Progress in Materials Science 64 (2014) 121–199

Contents lists available at ScienceDirect

Progress in Materials Science

journal homepage: www.elsevier.com/locate/pmatsci

Thermodynamic theory of growth of nanostructures

X.L. Li [a,b], C.X. Wang [b], G.W. Yang [b,*]

[a] MOE Key Laboratory of Laser Life Science & Institute of Laser Life Science, College of Biophotonics, South China Normal University, Guangzhou 510631, Guangdong, PR China

[b] State Key Laboratory of Optoelectronic Materials and Technologies, Institute of Optoelectronic and Functional Composite Materials, Nanotechnology Research Center, School of Physics & Engineering, Sun Yat-sen University, Guangzhou 510275, Guangdong, PR China

ARTICLE INFO

Article history:
Received 22 November 2013
Received in revised form 21 February 2014
Accepted 8 March 2014
Available online 15 March 2014

Keywords:
Nanostructures
Thermodynamics
Growth mechanism
Quantum dots and rings
Nanowires
Epitaxy

ABSTRACT

Self-assembled nanostructures, such as quantum dots (QDs), quantum rings (QRs) and nanowires (NWs), have been extensively studied because of their physical properties and promising device applications. To improve their physical properties and device applications, the fabrication of nanostructures with a uniform size, proper shape and regular position is desired in nanotechnology. Therefore, investigations of the growth process of nanostructures are highly important to control the self-assembly and synthesis processes of nanostructures flexibly. Thermodynamic theory as a universal approach to investigate material growth has been widely used to study the growth of nanostructures. This review covers the thermodynamic theoretical treatments of the growth of nanostructures, including QDs by epitaxy, QRs by droplet epitaxy, and NWs by the vapor–liquid–solid (VLS) mechanism. First, we introduce the thermodynamic models of the growth mechanisms of QDs by self-assembled epitaxy. The formation, stability, shape and position of QDs are discussed. Second, we introduce the nucleation thermodynamics and the growth kinetics of QRs by droplet epitaxy, and we present a simulation method employing the shape evolution of QRs based on a kinetic model. Third, several theoretical tools are introduced to address the nucleation and growth of NW by the VLS process. Finally, we introduce a thermodynamic treatment including the thermal fluctuations within the context of a statistical mechanical and

* Corresponding author.
E-mail address: stsygw@mail.sysu.edu.cn (G.W. Yang).

http://dx.doi.org/10.1016/j.pmatsci.2014.03.002

quantum mechanical model for the temperature-dependent growth of nanostructures.

Contents

1. Introduction

As promising candidate materials for future devices in optoelectronic and microelectronic applications, semiconductor nanostructures, such as quantum dots (QDs), quantum rings (QRs) and nanowires (NWs), have become the focus of intensive research [1–8]. These nanostructures not only provide a good system to study the electrical and thermal transport in low-dimensional confinement, but they also play an important role as interconnecting and functional units in fabricating electronic, optoelectronic, and magnetic storage devices. Therefore, to attain various nanometer-sized building blocks, numerous self-assembly and synthesis processes have been developed in recent years [9–14]. Importantly, these assembly and synthesis processes have revealed many unusual thermodynamic and kinetic aspects of microphase growth, which play an important role in the development of thermodynamics at the nanometer scale.

The self-assembly of nanostructures is a process in which a disordered system of pre-existing atoms or clusters form an organized structure or nanoscale domain pattern [15–18]. The interactions of atoms or clusters of atoms are the thermodynamic and kinetic driving forces of the self-assembly process. Therefore, to control the growth of nanostructures, it is essential to investigate the thermodynamic and kinetic process of self-assembly and develop new theoretical tools to address the nanoscale fabrication. For this purpose, several thermodynamic and kinetic tools have been developed in recent years to pursue the nucleation, growth and transformation of nanostructures upon vapor deposition.

Thermodynamics describes the average behavior of very large numbers of microscopic constituents, and its laws can be derived from statistical mechanics. A general rule of thermodynamics is that every system seeks to achieve a minimum value of free energy. Therefore, some theoretical treatments of the growth of nanostructures have been established according to thermodynamics-based theories [19–32]. In simple energetic models, nanostructures tend to move from an unstable state to a stable state, and the energy attains a minimum value and the decrease in the energy drives nanostructure evolution. These energy theories are successful in addressing many aspects of nanostructure growth, such as the formation of QDs by epitaxy, the evolution of NWs, and so on.

On the other hand, these energy models always focus on thermal equilibrium and neglect thermal fluctuations. Thus, they cannot address the effect of temperature on the growth of nanostructures. In fact, the entropic gains of the interface would be high enough to destroy the thermal equilibrium stability during the actual growth. Therefore, it is essential to develop a new theoretical treatment that includes the thermal effects to understand the temperature-dependent growth characteristics. Recently, several thermodynamic treatments that include a thermal effect have been developed [33–37]. Thermal fluctuations lead to oscillations of the nanostructure surface. Based on statistical mechanics and quantum mechanics, we can explore the probability of various surface topographies and deduce the most stable nanostructures. This thermodynamic treatment has successfully described a number of aspects of the temperature-dependent growth of nanostructures.

This review focuses on the thermodynamic, theoretical treatments of the growth of nanostructures, including the growth of QDs by epitaxy, QRs by droplet epitaxy, and NWs by vapor–liquid–solid (VLS) growth. It is organized as follows. In Section 2, the growth mechanism of QDs by epitaxy is introduced in connection with their formation, stability, shape, and position. First, we introduce the thermodynamic theory of the formation and stability of QDs on a flat semiconductor surface. Then, the shape transitions of QDs during the growth process and the capping process are discussed based on the thermodynamic models. Finally, we introduce a growth mechanism related to the position of the QDs on the patterned substrates and in vertically stacked structures. Section 3 is devoted to the growth of QRs by droplet epitaxy. In this section, taking GaAs QRs as an example, the nucleation thermodynamics

and growth kinetics are discussed. In Section 4, several theoretical tools to address the nucleation and growth of NW are introduced. Additionally, the size-dependent shape evolution of NWs is demonstrated according to the thermodynamic and kinetic factors. At the end of this section, a thermodynamic treatment of core–shell NW heterostructure growth is performed. Section 5 shows a thermodynamic model to study the temperature-dependent growth of nanostructures, in which thermal fluctuations lead to oscillations of the nanostructure surface. Using a thermodynamic treatment, the stability of the nanostructures and their temperature-dependent growth are discussed. Finally, concluding remarks are presented in Section 6.

2. Growth of QDs by epitaxy

Quantum dots (QDs), also called nanocrystals, are small enough to cause quantum confinement and create discrete electronic states [38–40]. QDs may result from lithography techniques such as focused ion beam, photolithography or selective chemical etching. Although lithography techniques yield lateral resolution down to several tens of nanometers, the disadvantages are the complicated technological processes and the high cost of the equipment [2]. Of the range of techniques for the fabrication of QDs, self-assembled epitaxial growth of QDs on semiconductor surfaces has become one of the most successful approaches [41], and it allows one to obtain a large number of homogeneous dots without slow and costly lithography steps [2,3]. The formation of QDs (also called strained islands) in these systems is driven by the strain in the epitaxial film due to the dissmilar lattice constants of the film and the substrate; this growth mechanism is also known as the Stranski–Krastanow growth mode [42]. This method has been successfully applied to fabricate arrays of semiconductor QDs that are composed of materials from the II–VI, III–V, or IV–IV groups on the periodic table, such as CdSe [43–46], InAs [47–57], InP [58–61], and Ge QDs [14,62–75]. The self-assembled QDs fabricated by this technique are typically between 10 and 50 nm in size.

Semiconductor QDs have wide potential applications in micro-, opto- and nanoelectronic devices [5]. By controlling the composition of a material and changing the size of the QDs, the optoelectronic properties can be tuned. The electronic spectrum of the bulk is continuous, but that of QDs is not continuous. Therefore, a QD can be called a "superatom", although it contains many atoms (approximately 10^5 – 10^6 atoms) [9]. Because of the atomic-like electronic spectrum of QDs, QDs have been used as an active medium of semiconductor lasers to improve the laser performance [76,77]. QDs can also be used to construct new types of devices, e.g. cellular automata [78,79] and single-electron transistors [80,81]. In the fields of computer science, there is a strong interest in QDs. Because the position of a single electron in a QD might attain several states, a QD could represent a byte of data. Alternatively, a QD might be used in more than one computational instruction at a time [82,83]. Other applications of QDs also include nanomachines [84], neural networks [85], and high-density memories or storage media [86,87].

2.1. Formation and stability of QDs

2.1.1. Three growth modes by epitaxy

Epitaxy is a method of depositing a crystalline overlayer on a crystalline substrate, in which the overlayer is called an epitaxial film or an epitaxial layer. The epitaxial film has an identical lattice structure and the same orientation as those of the substrate because of the effect of the crystal substrate. Generally, if the epitaxial film has the same composition as that of substrate, we name the process homoepitaxy; otherwise, it is called heteroepitaxy.

In homoepitaxial growth, the different conglomerations of deposited atoms lead to various configurations [88,89]. However, when the deposited temperature is so high that deposited atoms can diffuse easily on the substrate surface, these various configurations tend to form a layer-by-layer structure. This is because the two-dimensional (2D) layer-by-layer growth mode has the maximum number of bonds between the deposited atoms and the substrate [90]. However, the growth mode for heteroepitaxy becomes more complex. Traditionally, there are three growth modes for epitaxial films [91]. They are layer-by-layer growth (the Franck–van der Merwe mode, FV) [92], layer-by-layer

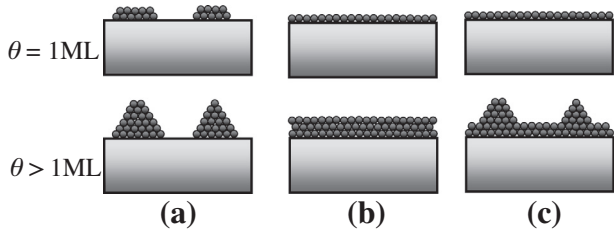

Fig. 1. Schematic illustration of three growth modes in heteroepitaxial growth. (a) 3D island growth (Volmer–Weber growth), (b) layer-by-layer growth (Franck–van der Merwe growth), and (c) layer-by-layer growth followed by island formation (Stranski–Krastanow growth). The deposition amount θ in the top row and bottom row are equal to 1ML and larger than 1ML (ML represents monolayer).

growth followed by island formation (the Stranski–Krastanow mode, SK) [42] and three-dimensional (3D) island growth (the Volmer–Weber mode, VW) [93], as shown in Fig. 1.

The basics behind the various growth modes is often understood within a simplified thermodynamic picture, through the well-known Young's equation [94]. When an epitaxial film is deposited onto a substrate, the stability of the surface is associated with the interplay of various thermodynamic properties, such as the surface energy densities of the film and of the substrate, and the interface energy density between the film and the substrate [6]. We symbolize these as γ, γ', and γ'', respectively. According to Young's equation, the equilibrium condition of a film should satisfy the equation:

$$\cos\alpha = (\gamma' - \gamma'')/\gamma \tag{2.1}$$

where α is the contact angle between the local film and the substrate. We find that the value of $\cos\alpha$ is larger than 1 when $\gamma' \geqslant \gamma + \gamma''$, which means the contact angle is zero, i.e., for a complete wetting process. Therefore, the layer-by-layer growth mode will occur. However, $\cos\alpha$ is less than 1 when $\gamma' < \gamma + \gamma''$, which means the film has a definite contact angle with the substrate. Further, the deposited atoms should grow on the substrate surface in the island growth mode in the case of $\gamma' < \gamma + \gamma''$.

SK growth is an intermediate mode consisting of 3D islands with a wetting layer (WL). The appearance of an initially complete WL means that $\gamma' \geqslant \gamma + \gamma''$. Because the formation of the WL occurs mimics the crystal surface, there is often an associated stain due to the lattice mismatch. As the WL thickens, the associated strain energy increases rapidly. To relieve the strain, island formation occurs in a coherent fashion [95,96]. Therefore, it is necessary to take the effect of strain into account in the investigation of the SK growth mode.

2.1.2. Formation of QDs in the Stranski–Krastanow growth mode

During heteroepitaxial growth, the epitaxial film suffers from a compressive or tensile strain induced by the lattice mismatch with the substrate. If the mismatch is sufficiently small, defect-free growth can proceed in the initial deposition process. As the epitaxial film grows, the strain stored in the film must be released. Except for the formation of defects, if the deposited temperature is high enough and the growth rate is slow enough, the formation of QDs is another pathway available for the release of strain [97–103], and is typical of the SK growth mode.

In the SK growth mode, an epitaxial WL first appears on the substrate surface. When the WL exceeds a critical thickness, QDs can form on its surface to release the strain; the reduction of the strain energy is called the elastic relaxation energy. However, the formation of QDs can also lead to an increase in the surface energy. If the relaxation energy is larger than the increment of the surface energy, it is favorable to form QDs. The gain in the elastic relaxation energy is proportional to the QD volume V, and the increment of the surface energy is proportional to $V^{2/3}$. Therefore, the change in the total energy caused by the formation of QD is [67,104,105]

$$\Delta E = A\gamma V^{2/3} - \kappa\varepsilon^2 A' V \tag{2.2}$$

where A and A' are coefficients that are determined by the shape of the QD, γ is the surface energy per unit area, κ is an elastic constant, and ε is the lattice mismatch. In this case, as the QD volume

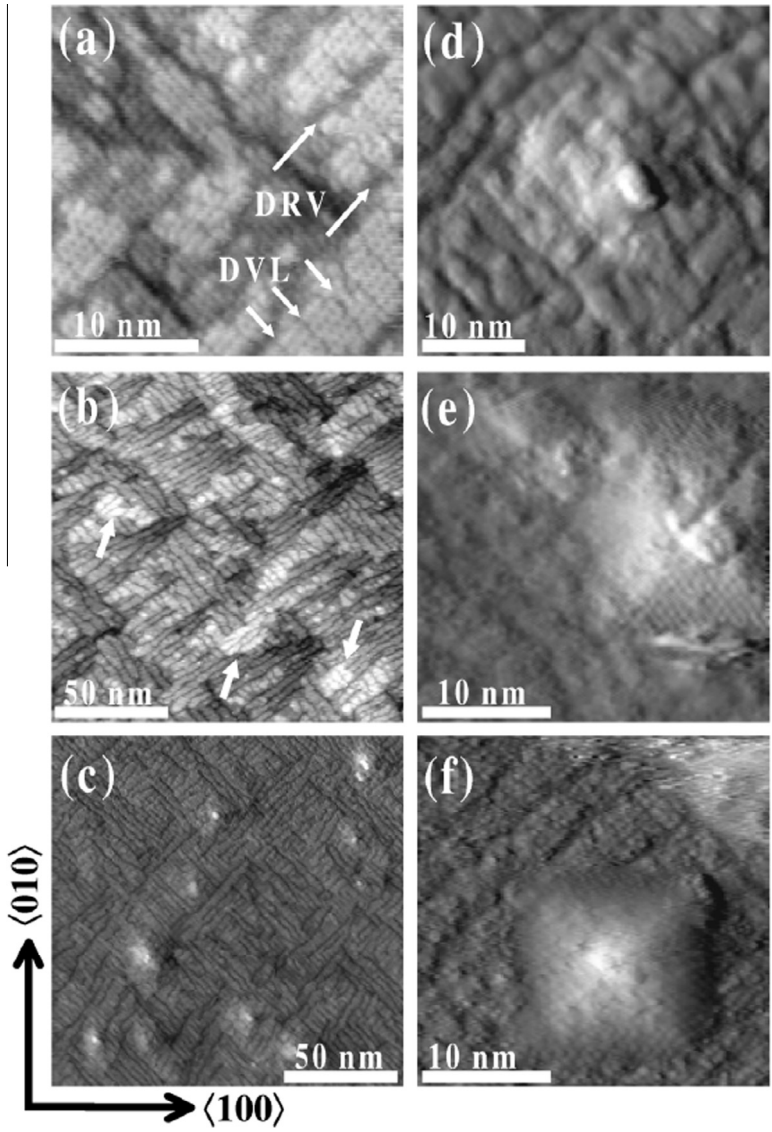

Fig. 2. STM images of the surface evolution during growth of a Ge film on Si(001). During growth in (a) and (b) at θ_{Ge} = 2.8 and 2.9 ML, 2D WL form on the Si substrate. When θ_{Ge} increases to 3.55 ML, initial prepyramid QDs appear on the WL in (c) and (d). Then these prepyramid QDs translate {105} facetted pyramids at θ_{Ge} = 3.85 and 4.0 ML in (e) and (f) [71].

increases, the total energy first increases and then decreases. When the volume of the QD exceeds a critical value, the change in the total energy becomes less than zero, which means that the formation of QDs is more favorable thermodynamically.

Taking the typical example of Ge QDs on Si(001), the QDs evolve due to the Asaro–Tiller–Grinfeld instability [106,107], and the slope of their sidewalls increases gradually until an angle of approximately 11.3° is reached, which corresponds to a pyramidal shape with four {105} facets. During further growth, the facet angle remains unchanged and {105}-facetted pyramids develop [95,96,108]. Based on the considerations for the energy change, the formation of a Ge QD with a pyramidal shape requires an energy of [104]

$$\Delta E = 4\Gamma V^{2/3}\tan^{1/3}\alpha - 6AV\tan\alpha \tag{2.3}$$

where α is the contact angle of the facets with respect to the substrate surface; $\Gamma = \gamma_s/\sin\alpha - \gamma_w\cot\alpha$, and γ_s and γ_w are the surface energy densities of the QD side and WL; $A = (M\varepsilon)^2(1-\upsilon)/(2\pi G)$, where M and ε are, respectively, Young's modulus and the misfit strain of the Ge film, and υ and G are, respectively, the Poisson ratio and shear modulus of the Si substrate. Lu and Liu [100] estimated the critical size for the formation of Ge QDs using first-principles calculations of energies and the strain dependence of the Ge/Si(001) surface. They found that the critical height and lateral size for pure Ge QDs on Si(001) are 1.1–1.6 nm and 11–16 nm. The modeling results agreed well with the minimum Ge QD size observed by several different experimental groups [71,72,108–110].

The analysis above shows that strain relaxation is the driving force for the formation of QDs. However, the simple consideration of the energy change cannot explain why QDs appear only when the WL exceeds a critical thickness. Experimental observations have shown that the transition from a 2D WL to 3D pyramid QDs only occurs when the coverage is larger than a critical value, as shown in Fig. 2 [71]. To explain why QDs only form when the WL exceeds a critical thickness, we must consider changes in the WL.

For an existing WL, there are two possibilities for further growth. The first is continuing 2D growth, and the second is forming 3D QDs on the WL, as shown in Fig. 3 [20,111]. Therefore, we can compare the changes in the energy caused by the two growth modes to identify which growth mode is favored. Maintaining layer-by-layer growth results in an increase in the thickness of the WL. The surface energy density of the WL depends on its thickness and can be intuitively written as $\gamma(\theta)$, where θ represents the thickness of the film [21]. According to the Müller and Thomas theory [112], if a few layers are deposited onto a substrate, the surface energy density of the layer obeys an exponential change [113–115]. Thus, the surface energy density of a film (material A) that contains θ layers on the substrate (material B) can be written as [21]:

$$\gamma(\theta) = \gamma_B^{\infty} + (\gamma_A^{\infty} - \gamma_B^{\infty})(1 - e^{-\theta/\eta}) \tag{2.4}$$

where $\Delta\gamma$ is the surface energy density change of a clean substrate to a monolayer film, γ_B^{∞} is the surface energy density of substrate, and γ_A^{∞} is the surface energy density of an infinite-thickness film that is assumed to have a crystal structure that matches that of the substrate in the vertical growth direction. For the Ge/Si(001) system, the theoretical results [21] are consistent with the calculated results from the first-principles calculations [100,116]. In this case, we can obtain the change in the energy caused by the two growth situations, layer-by-layer growth (situation A) and QD formation (situation B) (Fig. 3). For situation A, the change in the energy, ΔE_A is:

$$\Delta E_A = S[\gamma(\theta_0) - \gamma(\theta_{WL})] + \omega_1\varepsilon_0^2 Sh_0(\theta_0 - \theta_{WL}) \tag{2.5}$$

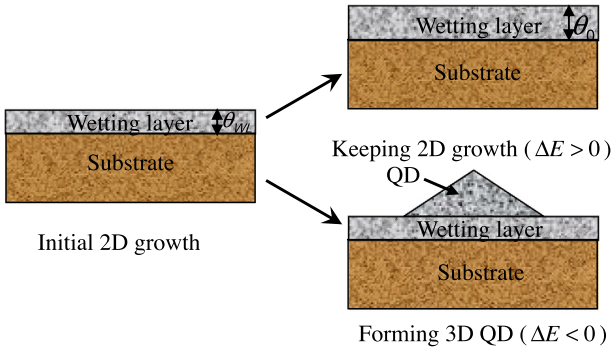

Fig. 3. Schematic illustration of two possibilities of further growth on a WL: keeping 2D growth and forming 3D quantum dots on the WL [111].

where S is the area of WL, h_0 is the thickness of the monolayer, and ω_1 is an elastic constant. The first term is the change in the surface energy, and the second term represents the strain energy caused by the mismatch with the substrate.

For QD formation, the change in the energy, ΔE_B can be calculated by:

$$\Delta E_B = [\gamma_s A_1 V^{2/3} - \gamma(\theta_{WL}) A_2 V^{2/3}] + (\omega_1 \varepsilon_0^2 V - \omega_2 A_3 \varepsilon_0^2 V) \tag{2.6}$$

where γ_s is the surface energy density of the QD side facet, V is the volume of the QD, ω_2 is another elastic constant [117], and A_1, A_2, and A_3, are the shape factors [111,118]. The first term is the change in the surface energy caused by QD formation, and the second term represents the strain energy of the QD. Therefore, the difference in the energy changes between the two growth modes, $\Delta E = \Delta E_B - \Delta E_A$, can be written as [111]:

$$\Delta E = [\gamma_s A_1 V^{2/3} - \gamma(\theta_{WL}) A_2 V^{2/3}] - \omega_2 A_3 \varepsilon^2 V - \frac{1}{k}[\gamma(\theta_{WL} + kV/h_0) - \gamma(\theta_{WL})] \tag{2.7}$$

Fig. 4 shows the value of ΔE as a function of the volume of the Ge QDs on a Si(001) substrate. When the thickness of the WL is too small (θ_{WL} = 3 ML), the value of ΔE is always larger than zero, which means that it is impossible to form QDs; in other words, the layer-by-layer growth mode is favored in the early growth stage. As the thickness of the WL increases, the value of ΔE becomes less than zero when the volume of the QD exceeds a critical volume, which means that the QDs can only form on the WL when the WL reaches a certain thickness. All of the analytic results show that the growth process is the typical SK growth mode, in which the QDs form only at a critical coverage.

According to the relationship $\Delta E = 0$, we can obtain the critical condition of the transition from the 2D to the 3D growth modes. The relationship between the critical thickness of WL (θ^*_{WL}) for QDs forming and the critical volume of QD (V^*) can be written as [111]:

$$\theta^*_{WL} = \eta \ln \frac{\left[\frac{1}{k}(1 - e^{-kV^*/\eta h_0}) - A_2 V^{*2/3}\right](\gamma_{substrate} - \gamma^{\infty}_{WL})}{\omega A_3 \varepsilon^2 V^* - \left(\gamma_s A_1 V^{*2/3} - \gamma^{\infty}_{WL} A_2 V^{*2/3}\right)} \tag{2.8}$$

Fig. 5 show the modeling results for the Ge/Si(001) and the InAs/GaAs(001) systems. We find that the critical thickness of the WL for the Ge QD formation is larger than 3.5 ML, and the critical thickness of the WL for the InAs QD formation is larger than 1.5 ML. These theoretical results are in good agreement with the experimental observations, e.g., the Ge QDs initially form after the formation of a WL with a thickness exceeding 3.5 ML [71,119,120], and the critical thickness of the WL for InAs QDs on GaAs(001) is reported to vary from 1.2 to 2.0 ML [120–125]. The physical original of the observation that QDs only form on a WL with a thickness larger than a critical value is the balance between the thickness-dependent surface energy of the WL and the relaxation energy caused by

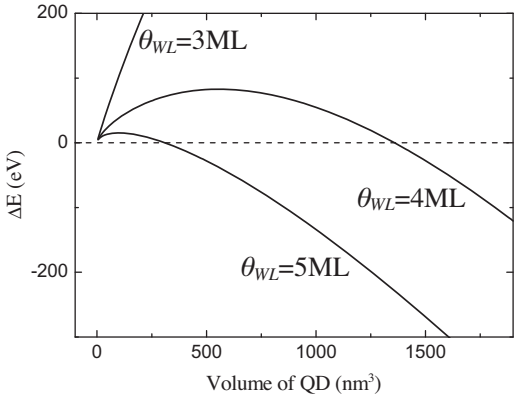

Fig. 4. The change of total energy as a function of Ge QD volume under different thicknesses of WL, θ_{WL} = 3 ML, 4 ML and 5 ML.

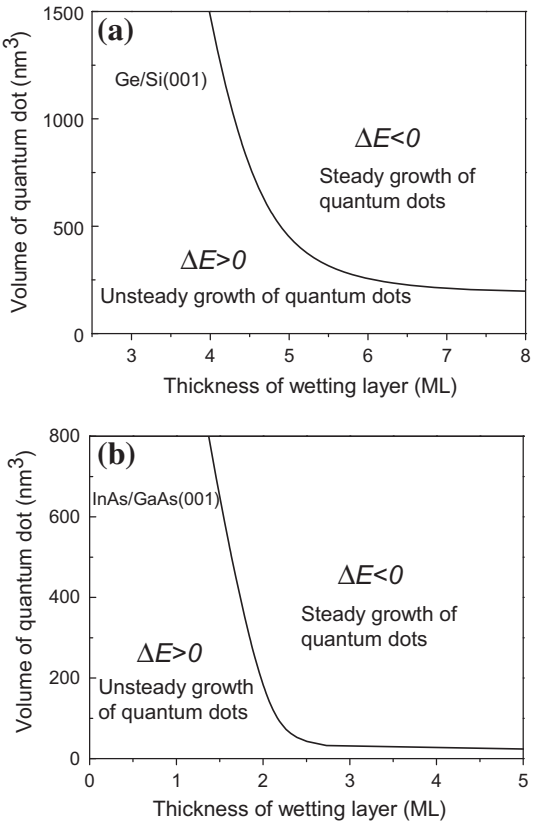

Fig. 5. The critical condition of the transition from the two-dimensional to three-dimensional growth modes for the two systems. (a) Ge/Si (001) and (b) InAs/GaAs (001) [111].

the QD formation. In the initial growth stage, lthe ayer-by-layer growth mode is favored over the QD growth mode due to the rapid decrease in the surface energy of the WL. When the WL exceeds a critical thickness, the rate of the decrease in the surface energy of the WL becomes very small. In this case, the relaxation energy of the QDs plays a key role in the further growth process. ΔE becomes less than zero when the QDs exceed a certain volume.

2.1.3. The steady state of QDs

After the QDs exceed the critical volume for their formation, QDs can grow steadily during a further deposition process. For a fixed deposited amount, the thickness of the WL decreases with the growth of the QDs at the expense of the WL. Because the effects of the thickness-dependent surface energy of the WL restrict the QD growth, the QDs cannot grow without limit and reach a final, steady state. We can also address the thermodynamic stability by analyzing the total energy per QD on the WL using Eq. (2.7). The only difference is that the total amount of the deposition is a constant here. Under a fixed amount of deposition θ_0, the total energy per QD on the WL can be written as [126]:

$$\Delta E = \gamma(\theta_{WL})\left(\frac{1}{k} - A_2 V^{2/3}\right) + \gamma_s A_1 V^{2/3} - \omega A_3 \varepsilon_0^2 V - \frac{1}{k}\gamma(\theta_0) \tag{2.9}$$

There exists the relation $\theta_{WL} = \theta_0 - kV/h_0$. The first term represents the surface energy of the WL with a single QD on it, the second term is the surface energy of the QD side facet, the third term is

the relaxation energy caused by the QD formation, and the last term represents the surface energy of the WL in the case without QD formation.

Eq. (2.9) shows the stability mechanism of the competition between the surface energy and the relaxation energy of the QD during the growth process. The relaxation energy of the QD drives its growth. However, the surface energy prevents the QD from growing. The growth of large QDs becomes more and more difficult with decreasing thickness of the WL until the entire system finally achieves thermodynamic equilibrium. Fig. 6(a) shows the calculated value of the total energy as a function of the QD volume under various densities of QDs and a fixed amount of deposition $\theta_0 = 6ML$. There is a minimum value of the total energy, and the steadiest size decreases with increasing density of QDs. This is because, when the amount of deposition is fixed, the growth of the QDs requires more deposited atoms in the case of a high density of QDs than in the case of a low density. Deposition is a process in which the amount of deposit increases continuously and the QD density can be considered as a constant [21]. Therefore, we calculate the total energy as a function of the QD volume under various amounts of deposition and a fixed density, as shown in Fig. 6(b). We find that the energy is always larger than zero and does not have a minimum value when the amount of deposit is less than 4 ML, which means that it is unfavorable to form QDs under a low deposition amount. The results are in good agreement with the experimental observations in which there is no QD formation on the WL when the total amount of deposit is less than 4 ML [127,128]. When the deposition amount is larger than 4 ML, there is a minimum value of the total energy. Further, the steady size increases with an

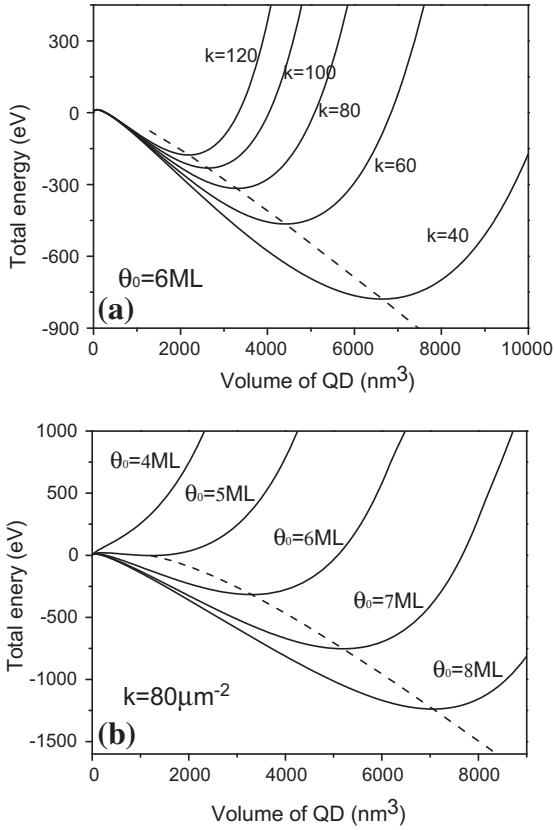

Fig. 6. (a) Total energy per QD as a function of QD volume in the Ge/Si(001) system under a fixed amount of deposited $\theta_0 = 6$ ML and different densities of QDs, $k = 40\ \mu m^{-2}$, $k = 60\ \mu m^{-2}$, $k = 80\ \mu m^{-2}$, $k = 100\ \mu m^{-2}$, and $k = 120\ \mu m^{-2}$. (b) Total energy per QD under a fixed density of QDs and different amounts of deposited $\theta_0 = 4$ ML, $\theta_0 = 5$ ML, $\theta_0 = 6$ ML, $\theta_0 = 7$ ML, and $\theta_0 = 8$ ML [126].

increasing amount of deposit. This is because the QDs can adsorb more deposited atoms for growth due to the increased deposition amount.

To reveal the evolution of the WL during the deposition process, Fig. 7 gives three-dimensional graphs of the steady thickness of the WL as functions of the density of the QDs and the amount deposited. We find that the steady WL does not become thicker but thins as the deposition amount increases. The results suggest that the WL not only fails to capture newly deposited atoms that instead contribute to growth, but it also releases atoms and thins to achieve a thermodynamic equilibrium during the deposition process. These interesting results are in good agreement with experimental observations [72,129,130]. In experiments, Ge atoms move from the WL into the QDs during annealing, and the thickness of the WL at a fixed deposition amount decreases with rising substrate temperature. According to the theoretical model, there are two reasons resulting in so puzzling a phenomenon. The first is that the driving force of growth for large QDs is larger than that for small QDs, thus large QDs can gain more atoms from deposition and the WL than small QDs. In addition, the surface coverage of the large QDs is higher than that of the small QDs when the density of the QDs is a constant. In this case, the resistance of the QD growth from the thickness-dependent surface energy of the WL becomes less effective for large QDs.

2.2. Shape transition of QDs

In typical semiconductor systems, such as the Ge/Si system and the InAs/GaAs system, QDs suffer from shape transitions as the volume of the QDs increases. During the growth of QDs, QDs undergo two obvious shape transitions, from a pre-pyramid to a pyramid [66,71,119] and from a pyramid with a low contact angle to a steeper dome [66,67,71,72,131–133]. However, during the capping process named as overgrowth, the reversible shape transition from a dome to a pyramid occurs with the increase of the capping deposition [134–136]. In this section, we introduce thermodynamic models to investigate the shape transitions of QDs.

2.2.1. Shape transition during the growth process

The Ge/Si(001) and the $Si_{1-x}Ge_x$/Si(001) systems, as ideal model systems for understanding the processes of QD formation and morphological evolution, have been intensively studied in the past decade. In these systems, 3D QDs first appear as shallow mounds (pre-pyramids) on a thin WL, and then they gradually transform into {105}-faceted pyramids. As they ripen, they undergo a shape transition into domes bounded by steeper facets. Beyond a certain critical size, the finally plastically relaxed

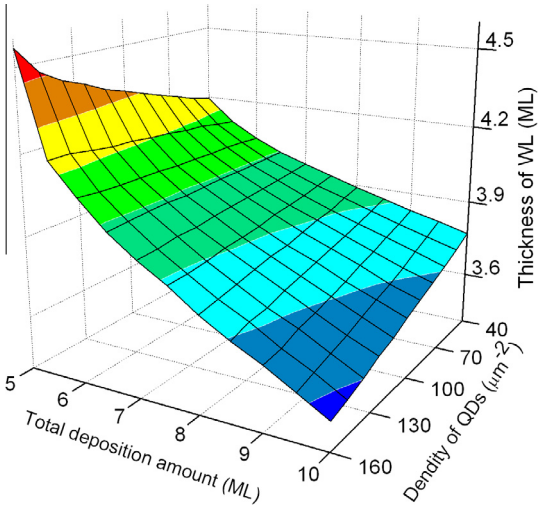

Fig. 7. Three-dimensional graphs of steady thickness of WL as functions of density of QDs and total deposition amount [126].

superdomes are formed with misfit dislocations at their bases [3,132]. Fig. 8 shows the size distribution of QDs as well as their shape evolution during Ge deposition onto Si(001) [71]. The thermodynamics of the shape transition was studied by different groups [19,21,133,137–140]. These studies have shown that the physical origin of the shape transition is actually the balance between the surface energy and the misfit strain of the QDs. In this section, we will introduce the thermodynamic models of the two typical shape transitions of QDs, from pre-pyramid to pyramid and from pyramid to dome.

For a nominal coverage θ_0 for which QDs with an identical pyramidal shape and volume appear after the formation of a WL whose thickness is θ, the total energy difference of a single QD between SK growth and the imaginary layer-by-layer modes can be written as:

$$\Delta E = \frac{1}{k}[\gamma(\theta) - \gamma(\theta_0)] + E_s - 4s^2\gamma(\theta) + E_r \tag{2.10}$$

where E_s is the surface energy of the QD facets, s is the half-base length, and E_r is the elastic relaxation energy of the QD ($E_r < 0$). For a single pyramidal QD, the volume of the QD should follow the relation $V = \frac{4}{3}s^3 \tan\alpha = \frac{1}{k}(\theta_0 - \theta)h_0$, where h_0 is the thickness of a monolayer. The first three terms in the equation represent the surface energy difference caused by the QD formation.

It is difficult to estimate the surface energy of the QD facets because the surface energy density of the QD facets varies with contact angle. To quantitatively compute the surface energy, we can regard the QD facet as a step facet [140]. Thus, the surface energy of the QD facets E_s can be divided into two parts: the surface energy of the terraces E_{st} and the step edge creation energy E_{sc}, i.e., $E_s = E_{st} + E_{sc}$. Therefore, the total energy difference of a single QD between the SK mode and the imaginary layer-by-layer mode becomes [21]

$$\begin{aligned}\Delta E = {} & \frac{1}{k}[\gamma(\theta) - \gamma(\theta_0)] + \sum_{n=1}^{n_T}[\gamma(\theta_n)A_n] + \gamma(\theta_{n_T+1})A_{n_T+1} + 8\sum_{n=1}^{n_T}[s - nh_0\cot\alpha] \\ & \times \left[\lambda_0 + \lambda_d\left(\frac{a\tan\alpha}{h_0}\right)^2\right] - 4s^2\gamma(\theta) - 1.3229Y\varepsilon_0^2\frac{1+\upsilon}{1-\upsilon}s^3\tan^2\alpha\end{aligned} \tag{2.11}$$

where the second term is E_{st}, the third term represents E_{sc} [140,141], and the last term is E_r [12–13].

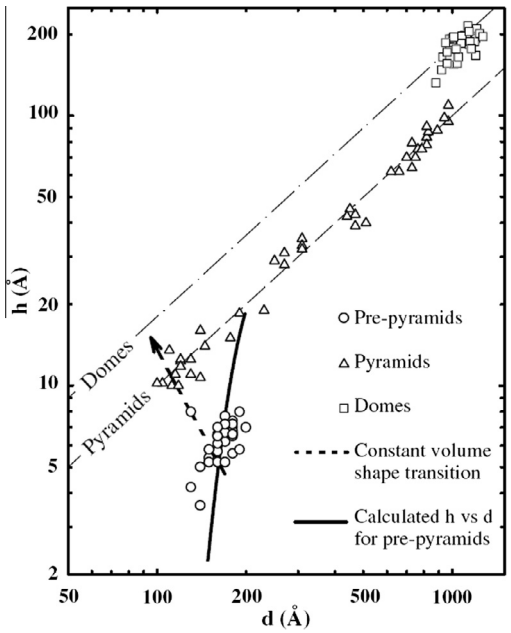

Fig. 8. The size distribution of three typical QD shapes during Ge deposition on Si(001). The symbols d and h represents the width and height of QD [71].

Fig. 9 shows the total energy change per unit volume as a function of the volume of the QDs for various contact angles. We find that QDs with a low contact angle are preferred over QDs with a high contact angle when the volume of the QDs is small. As the volume of the QDs increases, QDs with a high contact angle become favored over those with a low contact angle. The results explain well the shape transition of the QDs from a pre-pyramidal shape with a low contact angle to a pyramidal shape with a high contact angle.

The elastic relaxation energy at the top of the QDs drives the QD formation. However, the transition from a low contact angle to a high contact angle is determined not only by the elastic relaxation energy but also by the size-dependent surface energy. In the case of QDs with a small volume, the size-dependent surface energy dominates the total energy difference. Thus, the QD shape tends to minimize the surface energy, namely, to have a low contact angle. In the later stage of growth, the elastic relaxation becomes more significant and drives the QDs to have a high contact angle.

As the volume of QDs increases further, the shape of the QDs can transition from a pyramid to a dome, as shown in Fig. 10. We can adopt similar methods as above by comparing the total energies of the QDs with these two shapes [19,67]. Because both pyramidal QDs and dome-shaped QDs form on the existing WL, we can only compare the free energy of the formation of the QDs from a planar WL, ΔE. When the QD is a pyramid, the total energy change of a pyramidal QD is:

$$\Delta E_P = \left(\gamma_e \frac{1}{\cos\alpha} - \gamma_s\right)\left(\frac{6V_P}{\tan\alpha}\right)^{\frac{2}{3}} - \frac{9}{2}cV_p\tan\alpha \tag{2.12}$$

where γ_e and γ_s are the surface energy densities of the facets of the QD and the substrate, E_r is the elastic relaxation energy and $E_r = -(9/2)cV_p\tan\alpha$ [97], where α in the contact angle of the QD facet with the substrate. When the QD is a dome, we have [19]

$$\Delta E_D = \pi\left(\gamma_0 \frac{1}{\cos\alpha} - \gamma_s\right)\left(\frac{3V_D}{\pi\tan\alpha}\right)^{\frac{2}{3}} + \frac{2\pi\lambda}{\cos\alpha}\left(\frac{3V_D}{\pi\tan\alpha}\right)^{\frac{1}{3}} - \frac{9}{\sqrt{\pi}}cV_D\tan\alpha \tag{2.13}$$

where $E_s = \gamma_0 A_e + \lambda\int(1/r)dA_e$ according to the liquid-drop model [142], and $E_r = -(9/\sqrt{\pi})cV_D\tan\alpha$ [19].

Fig. 11 shows the theoretical results for pure Ge and $Ge_{0.4}Si_{0.6}$ QDs on a Si(001) substrate. Clearly, when the volume of a QD is less than a critical value, the energy change of a pyramidal QD is lower than that of a dome-shaped QD, which means that a QD with a pyramidal shape is more stable than that with a dome shape. However, when the volume of a QD is larger than the critical value, the energy change of a dome-shaped QD becomes lower than that of a pyramidal QD, which means that a QD with a dome shape is more stable. The results agree well with the experimental observations [66,67,72,132]. Due to the low relaxation energy caused by the small mismatch, the critical volume

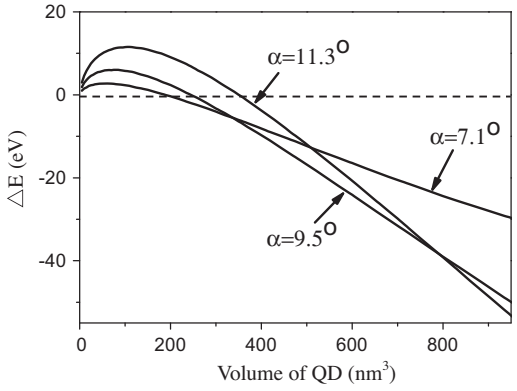

Fig. 9. The total energy change as a function of volume of QDs for different contact angles [21].

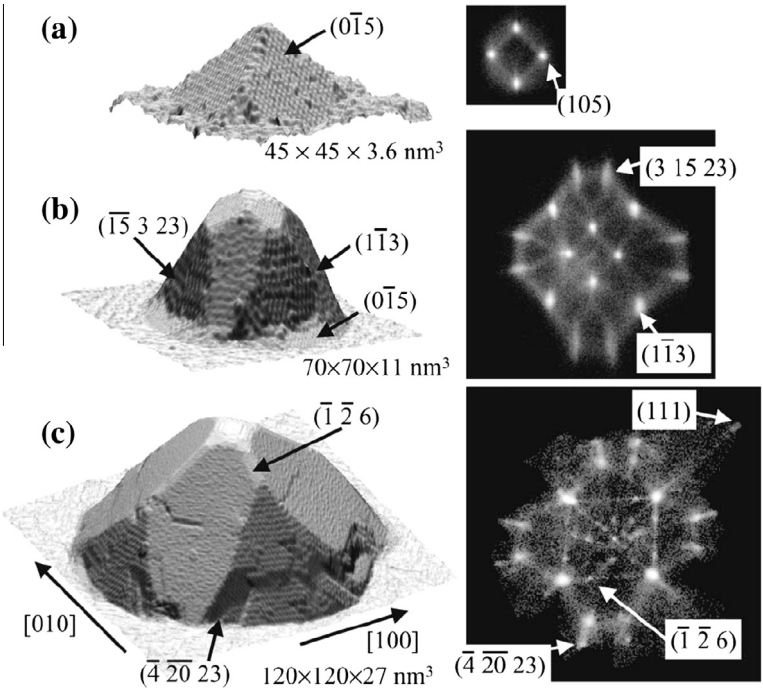

Fig. 10. STM images of a Ge pyramid (a), dome (b) and superdome (c). The corresponding facet plots are shown on the right. The scale of the images and the Miller indices of a few facets is indicated [132].

of a $Ge_{0.4}Si_{0.6}$ QD for the shape transition from a pyramid to a dome is larger than that for a pure Ge QD, as shown in Fig. 11(b). The results are in agreement with experimental observations [71,131].

The physical origin of the shape transition of a strained QD from a pyramid to a dome is actually the balance between the surface energy and the relaxation energy of the QD. In the early growth stage, the elastic relaxation is not efficient for the shape of a QD. The surface energy of a dome is larger than that of a pyramid. Thus, the equilibrium shape tends to be a pyramid. In the later growth stage, the elastic relaxation becomes more significant. The relaxation energy of a dome is larger than that of a pyramid with the same volume due to a dome having a high gradient. Hence, the energy change is lowered by the shape transition to gain the additional elastic relaxation.

2.2.2. Reversible shape transition induced by overgrowth

To incorporate self-assembled QDs into applications in optoelectronic and microelectronic devices, it is sometimes necessary to bury the QDs in a semiconductor matrix [143]. Therefore, the capping technique, i.e., overgrowth, is often used for the fabrication of the embedded structures above [134–136,144–149]. As the QDs are capped, the shape, size, strain and composition of the QDs will change, and these characteristic parameters for the QDs determine their physical properties [146]. For example, during the Si capping of Ge QDs, the Ge QDs have two obvious shape changes. The first change is a reversible shape transition, i.e., from a dome to a pyramid with increased Si deposition due to the decrease of the Ge concentration [134–136,145,146], as shown in Fig. 12. The second obvious change regards the QD volume. Rastelli et al. [134] reported that the volume of Ge QDs has a continuous increase. However, Lang et al. [136] showed that Ge QDs expand first and then shrink. These observations seem inconsistent. In the following, we introduce a quantitative thermodynamic theory to address the shape evolution and the volume change of the QDs induced by overgrowth [150].

During the Si capping process, the deposited Si atoms can be adsorbed directly by the QDs and the WL and then stick onto their surfaces [144]. The shrinkage of the Ge QDs is only induced by the

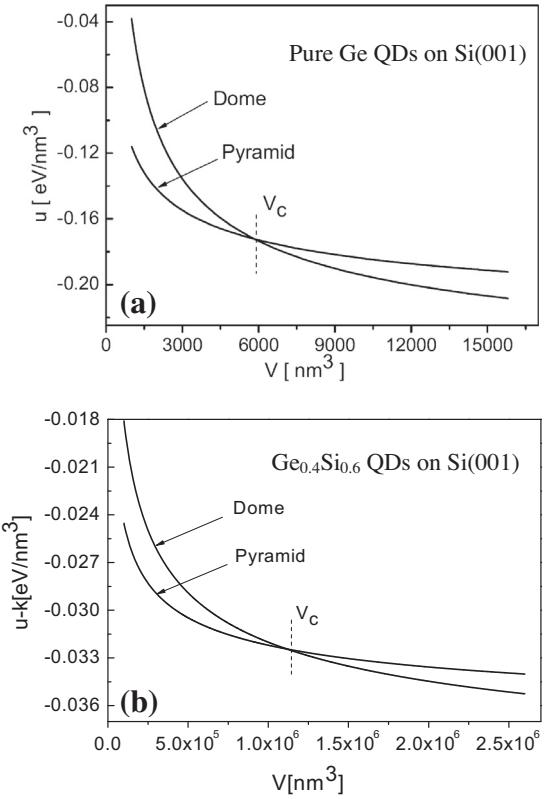

Fig. 11. Energy per unit volume of (a) pure Ge QDs and (b) $Ge_{0.4}Si_{0.6}$ QDs on Si(001) with two types shapes, pyramid and dome. $u = \Delta E/V$. The shape transition occurs at the critical volume V_c. The critical volume V_c of $Ge_{0.4}Si_{0.6}$ QDs is much larger than that of pure Ge QDs [19].

diffusion of Ge atoms from the QDs to the WL [136]. When Ge atoms diffuse from the QDs to the WL, the volume shrinkage of the QDs leads to an increase in the elastic relaxation energy. Meanwhile, the reduced surface area results in a decrease in the surface energy. The elastic relaxation energy of a single QD can be simply written as $E_r = -M\varepsilon^2 V_{QD} \tan\alpha$ [117]. Therefore, the increment of the relaxation energy of a single QD caused by the diffusion per unit volume of Ge from the QDs to the WL is equal to the increment of the total energy, i.e.:

$$\mu_{QD} = M\varepsilon^2 \tan\alpha \tag{2.14}$$

Diffusion of Ge atoms from the QDs to the WL would also result in an increase in the WL thickness, which can effectively reduce the surface energy of the WL. Considering a WL with a thickness of θ ML adsorbs Ge with a unit volume, the decrease in the surface energy of the WL is:

$$\mu_{WL} = \left[\gamma(\theta) - \gamma_{Ge}^{\infty}\right]\left(1 - \frac{1}{e}\right)\frac{1}{h_{0Ge}} \tag{2.15}$$

where h_{0Ge} is the thickness of the Ge monolayer, and $1/h_{0Ge}$ represents the surface area of the WL with a thickness of $(\theta + 1)$ ML. If $\mu_{WL} > \mu_{QD}$, the diffusion of Ge atoms from the QDs to the WL will be favored. Thus, there is a critical thickness of the WL when $\mu_{WL} = \mu_{QD}$. Meanwhile, considering the incorporation of Si into the WL and the surface segregation of Ge [151–153], we find that the critical WL has a nominal thickness θ_c' of [150]

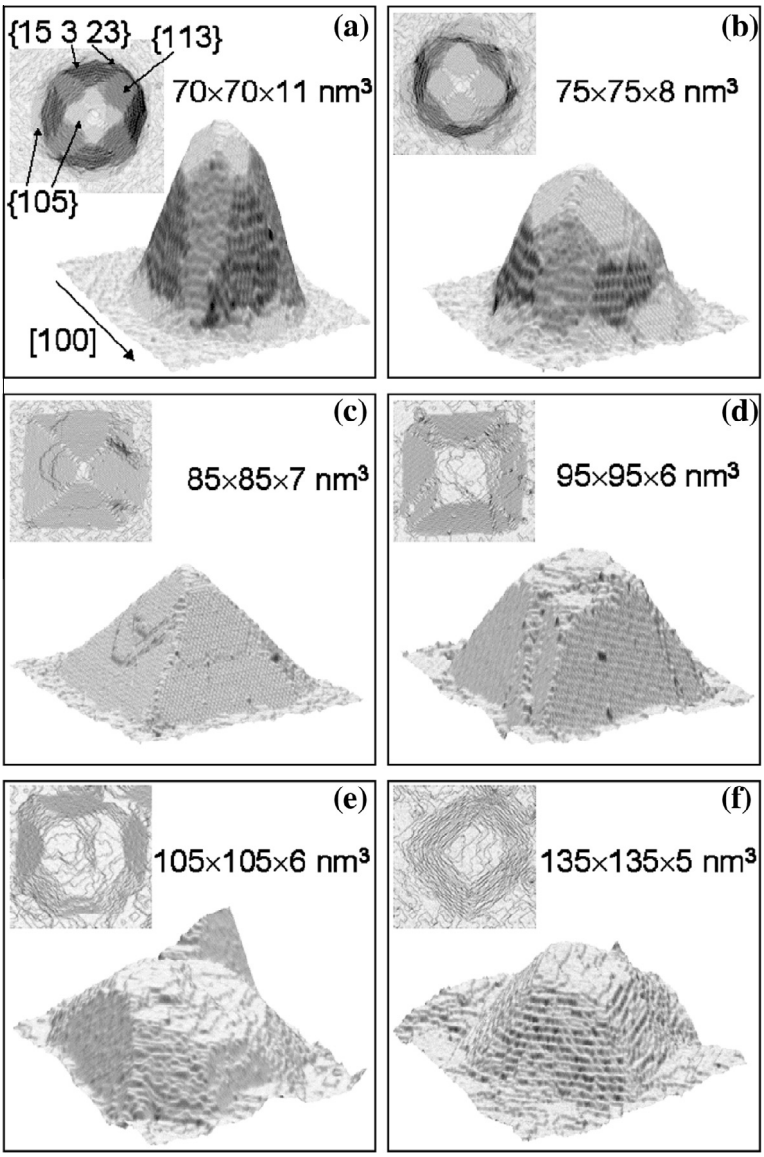

Fig. 12. STM topographs of representative Ge QDs during Si capping. (a) and (b), domes; (c) pyramids; (d)–(f) pre-pyramids. Si coverage θ_{Si} = 0, 1, 2, 4, 8, and 16 ML for (a)–(f) [134].

$$\theta_c' = \ln\left(\frac{\gamma_{Si}^{\infty} - \gamma_{Ge}^{\infty}}{\gamma(\theta_c) - \gamma_{Ge}^{\infty}}\right)\exp(K_1\theta_{Si}) \tag{2.16}$$

where K_1 represents the incorporation coefficient. This equation presents the balance between the QDs and the WL. When the critical thickness exceeds the initial thickness of the WL, Ge diffusion from the QDs to the WL will occur. In this case, the amount of Ge, ΔV_{Ge}, diffusing in one time step, Δt, exhibits the following behavior:

$$V_{QD}(t+\Delta t) = V_{QD}(t) + \frac{1}{D} C_{ov} k h_{0Si} - \Delta V_{Ge}$$
$$\Delta V_{Ge} = \frac{1}{D}(\theta_c(t+\Delta t) - \theta_c(t)) h_{0Ge}(1 - C_{ov}) \quad (2.17)$$

where D is the density of QDs, and C_{ov} is the surface coverage of QDs.

When the initial conditions, $V_{QD}(0)$ and $\theta_c(0)$, are known, we can deduce the evolution of the QDs during the Si-capping process. According to the initial conditions in the experiment by Lang et al. [136], modeling results are shown in Fig. 13(a). We find that there are three remarkable evolution stages of the QD volume, i.e., an expansion stage, a shrinkage stage, and a steady stage. In the first stage, the QDs expand because of Si absorption, and the Ge diffusion from the QDs to the WL barely happens. However, in the shrinkage stage, the critical thickness of the WL begins to exceed the actual thickness due to further Si absorption, which drives Ge atoms to diffuse from the QDs to the WL. Thus, the QDs start to shrink. However, due to Ge diffusion and further Si absorption, the increased rate of the critical thickness becomes quicker and quicker with an increase in the Ge concentration and the contact angle, which requires more Ge atoms to diffuse to wetting. In this case, the Ge diffusion from the QDs to the WL stops, and the Si absorption by the QDs becomes unfavorable when the QDs cannot provide enough Ge atoms to satisfy the demand of the WL. In this stage, the volume of the QDs scarcely changes. Additionally, the model is applied to the experiment by Rastelli et al. [134], and the calculated results are shown in Fig. 13(b). In this case, the QDs have a continuous increase in volume because of the high surface coverage of the QDs.

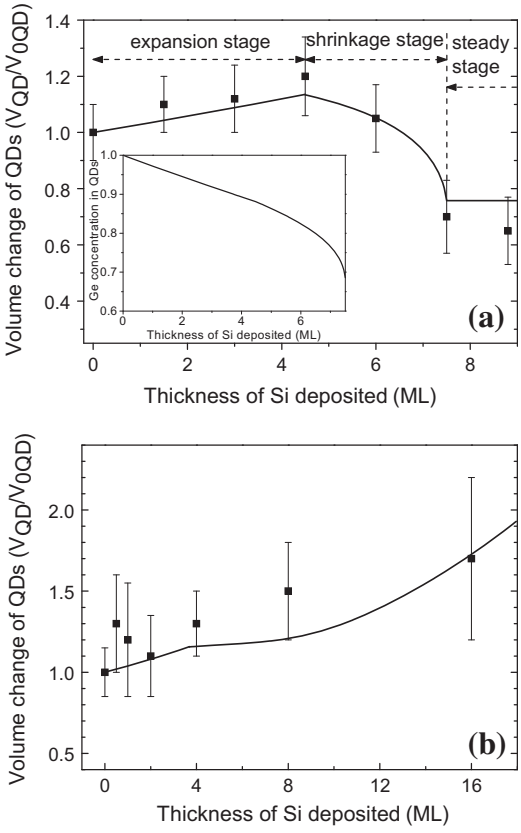

Fig. 13. (a) The calculated evolution of Ge QDs during the Si capping process and the comparison with the experimental data in Ref. [136]. The inset shows the predicted change of Ge concentration in QDs as the function of thickness of Si deposited. (b) The calculated volume evolution of Ge QDs and the comparison with experimental data (Ref. [134]) [150].

Based on the thermodynamic analysis, we find that the decrease in the Ge concentration of the QDs induced by Si absorption breaks the original balance of the composition between the QDs and the WL. To create a new balance, the WL is required to increase its thickness by Ge diffusion from the QD to the WL, which leads to the shape evolution of the QDs. The Ge diffusion can suppress the expansion of the QDs and promote their shrinkage.

2.3. Growth of QDs on patterned substrates

In general, QDs have a random spatial distribution due to their spontaneous nature. To improve device applications, it is important to fabricate QDs with a highly ordered arrangement. Growth onto patterned substrates is one of the most widely used approaches for controlling the spatial distribution of QDs. This approach has been successfully applied in the Ge/Si [154–166] and the InAs/GaAs [167–176] systems. In general, substrates with rectangular patterns can be obtained by lithography, such as optical lithography [158,159], holographic lithography [177], focused ion beam lithography [155], electron-beam lithography [165,178], and so on.

On patterned substrates, the surface curvature affects the formation sites of QDs. According to the thermodynamic perspective [15], it is usually believed that QDs should form preferentially in places with a negative curvature, i.e., in trenches or pits. For example, the formation of QDs always occurs at the intersection of the side facets within the pits, which results in long-range-ordered QD structures, as shown in Fig. 14 [166]. However, Yang et al. found a regular alignment of Ge dots on the stripes and mesas that are the most convex regions of the surface, as shown in Fig. 15 [158]. To understand the physical mechanism, several theoretical models have been established based on thermodynamic models or kinetic simulations [19,24,25,158,179–184]. In the following, we introduce the thermodynamic issues concerning the preferential sites of QD growth on a geometrically patterned substrate.

2.3.1. Surface chemical potential along patterned surface

It is well known that the most favorable nucleation sites are generally determined by the surface chemical potential [185]. The chemical potential along the surface of an uneven substrate is written as

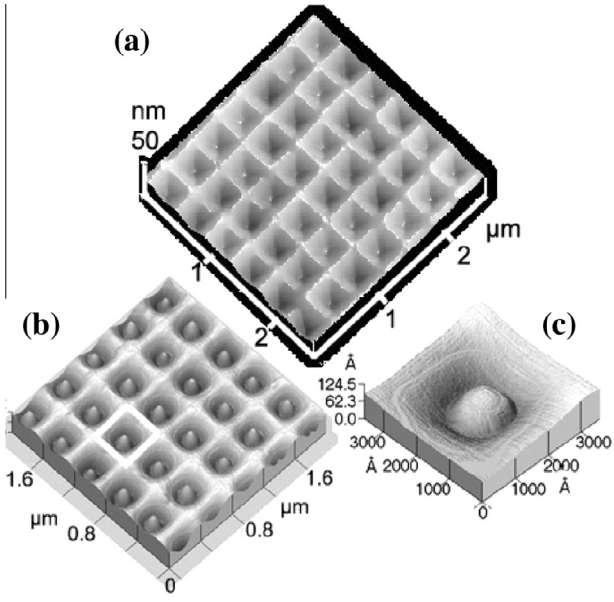

Fig. 14. AFM images of the surface of a Ge layer grown on lithographically prepatterned Sis(001) substrates [166].

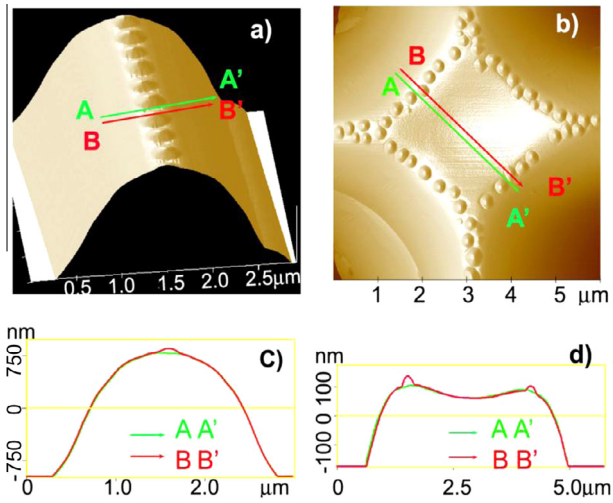

Fig. 15. AFM images of Ge QD ordering on patterned Si(001) structures: (a) a stripe ridge; (b) a diamond-shaped stripe cross. (c) and (d) are the cross sections through (a) and (b), respectively [158].

[185] $\mu = \mu_0 + \Omega\gamma k$, where μ_0 is the chemical potential of the planar surface, Ω is the atomic volume, γ is the surface free energy per unit area, and k is the local surface curvature. Convex regions have a higher chemical potential than that of concave regions. Thus, nucleation occurs favorably in concave regions [186]. However, if strain mismatch between the epitaxial film and the substrate is present, the strain relaxation in convex regions is more favorable than that in concave regions, which opposes the contribution from the surface curvature [5]. We need to add the strain contribution to the local chemical potential. Therefore, the surface chemical potential of the film should become [158]:

$$\mu = \mu_0 + \Omega\gamma k + \Omega E_s \tag{2.18}$$

where E_s is strain energy. When a QD C grows on a buffer layer B that is on a columned substrate A, the surface chemical potential is attained as [19]

$$\mu = \mu_0 + \Omega_B\gamma k + \frac{1}{4}\Omega_B C_B\left[\varepsilon_B^2 - \varepsilon_{BA}^2\right] + \frac{1}{4}\Omega_C C_C\left[\varepsilon_C^2 - \varepsilon_{CA}^2\right] \tag{2.19}$$

In the case that the buffer layer is the same material as the QDs, such as the deposition of Ge onto Si substrates, the Ge WL is the buffer layer. Eq. (2.19) can be written as:

$$\mu = \mu_0 + \Omega_B\gamma k + \frac{1}{2}C_B\Omega_B\left[\varepsilon_B^2 - \varepsilon_{BA}^2\right] \tag{2.20}$$

The equation has a similar meanings to that of the study by Yang [158].

In the case of InAs QDs on GaAs patterned substrates [167–169], an $In_{0.2}Ga_{0.8}As$ or a GaAs buffer layer is usually deposited first. Fig. 16 shows the chemical potentials of $In_{0.2}Ga_{0.8}As$ buffer layers with various thicknesses. The total chemical potential of the most convex regions is clearly larger than that of the other regions when the thickness of buffer layer is very small. Because a thinner buffer layer has a smaller strain-relaxation contribution, it is not strong enough to counteract the contribution of the surface energy in the convex regions. However, with the thickness of the buffer layer increasing, the strain relaxation contribution becomes more significant, and the most convex regions have the minima of the chemical potential. These results are consistent with experimental observations [167]. When the buffer layer is GaAs, Fig. 17(a and b) clearly shows that the regions with the minima of chemical potential are not the ridges of the stripes but the ridge feet (as shown in Fig. 17(a)) or the ridge sidewalls (as shown in Fig. 17(b)). The main reason is that the increment that caused the strain-relaxation contribution is less than the increment of the common chemical potential. These

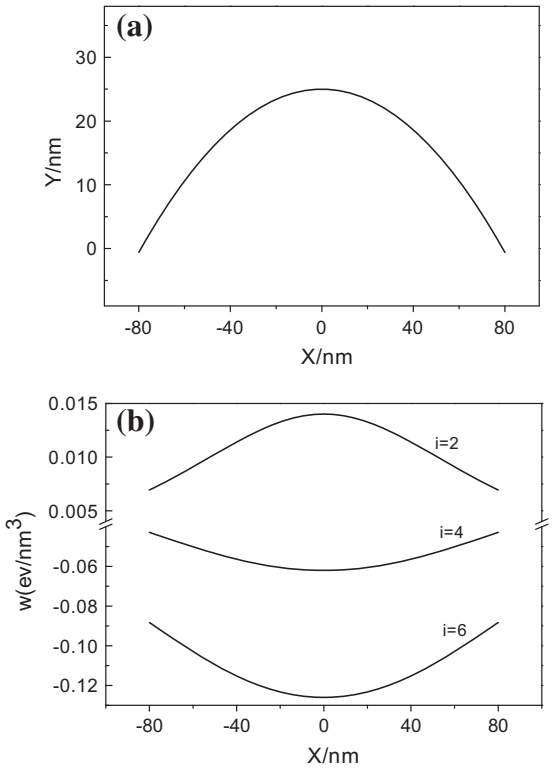

Fig. 16. The calculated chemical potentials with different thickness of $In_{0.2}Ga_{0.8}As$ buffer layer. (a) The surface profile of GaAs substrate. (b) The calculated chemical potentials with different thickness of buffer layer of $In_{0.2}Ga_{0.8}As$: $i = 2, 4, 6$, in which $w = (\mu - \mu_0)/\Omega$ [19].

theoretical results agree well with experiments [168,169], in which InAs QDs form at the ridge foot or the ridge sidewalls when a GaAs buffer layer is deposited.

2.3.2. Thermodynamic model of QDs on hole-patterned substrates

Recently, QDs with good spatial order have been grown onto substrates with a pattern of holes, such as the Ge/Si [155,182,187,188] and the InAs/GaAs [189–194] systems. Most of the experimental observations have shown that QDs form preferentially on the inside of a hole due to the negative surface curvature. However, Karmous [155] and Pascale [182] et al. reported that QD formation on the inside of a hole only occurs at a relatively low temperature (approximately 550 °C), but the QDs form on the terrace between the holes at temperatures higher than 700 °C, as shown in Fig. 18. Additionally, Martín-Sánchez et al. reported that the site of the InAs QD formation can be controlled by changing the distance between the holes [190]. They observed that most of the InAs QDs formed on the inside of the holes when the distance between the holes was 165 nm (Fig. 19(a)), but InAs QDs formed on the mesas between the holes when the distance was reduced to 30 nm (Fig. 19(b)). These interesting and puzzling experimental observations appear intuitively inconsistent with established theories. In the following, we introduce a thermodynamic model to address the self-assembly of QDs onto hole-patterned substrates.

Fig. 20 shows the schematic illustration of QD formation on hole-patterned substrates. During the deposition process, a thin WL first forms on the substrate surface due to the lower surface energy density of the WL than that of substrate. The total free energy of the WL on the hole-patterned substrate in the area per hole can be written as [24]:

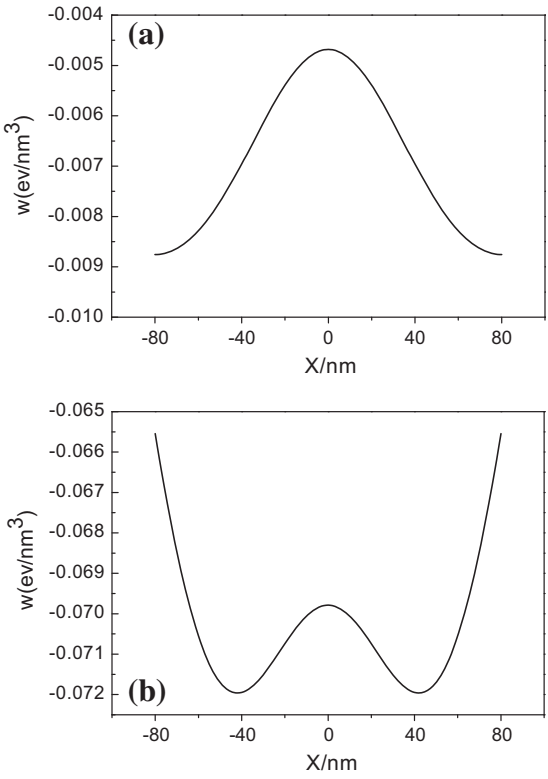

Fig. 17. The calculated chemical potential when 4 ML and 8 ML buffer layers GaAs are deposited on patterned substrates [19].

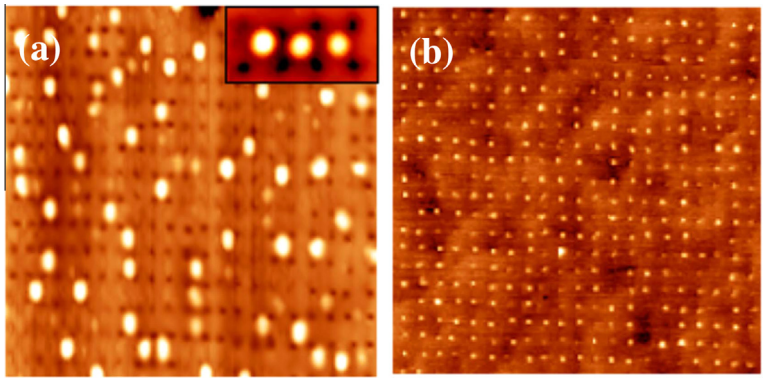

Fig. 18. AFM images (scan size is 2.5 μm) of focused ion beam patterned Si substrate after 8 ML Ge deposition at different temperatures *T*: (a) *T* = 750 °C. In this situation, the size of QD (100 nm) is in the range of the hole-hole distance (150 nm). The inset shows a higher magnification image of three Ge QDs situated on terraces between the pits. (b) *T* = 550 °C. In this situation, Ge QDs are located only in the holes [182].

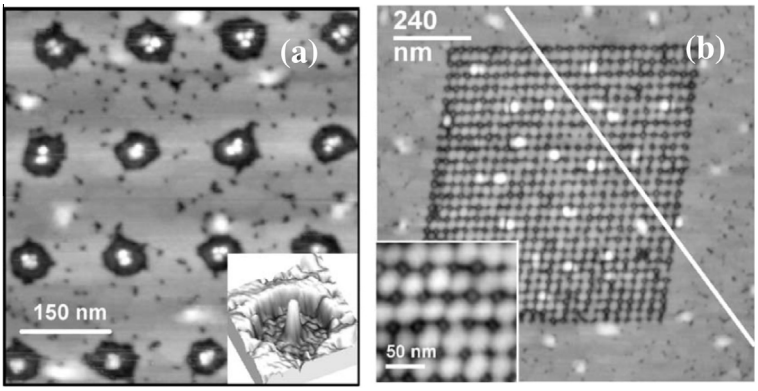

Fig. 19. AFM images of InAs QDs obtained by deposition of 0.5ML of InAs on GaAs hole-patterned substrate with the distance between the holes of (a) 165 nm and (b) 30 nm [190].

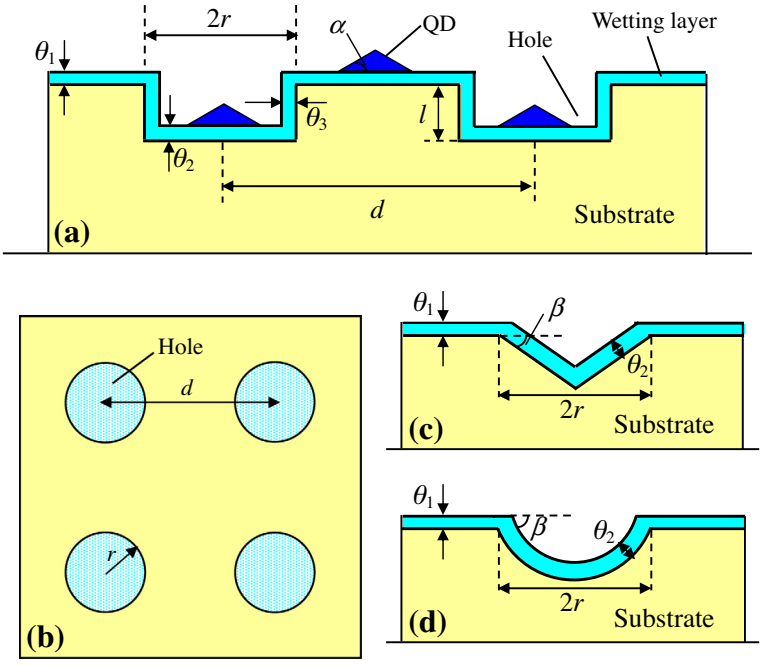

Fig. 20. Schematic illustrations of QDs formation on hole-patterned substrates. (a) Hole with column shape; (b) the top view of QDs array (c) hole with taper shape; (d) hole with part of sphere shape [24].

$$E_{2D}(\theta_0) = (d^2 - \pi r^2)\gamma(\theta_1, \phi_1) + \pi r^2 \gamma(\theta_2, \phi_2) + 2\pi(r - \theta_3 h_0)(l - \theta_2 h_0 + \theta_1 h_0)\gamma(\theta_3, \phi_3) + \omega_1 \varepsilon_0^2 V_{WL} + E_{corner} \tag{2.21}$$

where $\gamma(\theta_1, \phi_1)$, $\gamma(\theta_2, \phi_2)$ and $\gamma(\theta_3, \phi_3)$ represent the surface energy densities of the WL and the surface orientation (surface slope angle ϕ_1, ϕ_2 and ϕ_3) [21,195], and E_{corner} is the energy of the corners. The thermodynamic steady state can be found by minimizing the free energy function of Eq. (2.21). Taking the Ge/Si system as an example, the calculated results show that the thickness of the WL inside of a

hole is larger than that on the terrace at the thermodynamic steady state for which $\theta_1 \approx 3.8$ ML, $\theta_2 \approx 5.4$ ML, and $\theta_3 \approx 4.1$ ML [24]. The increased thickness on the inside of the hole can effectively reduce the surface area of the hole, which leads to a decrease in the surface energy of the hole.

Upon further deposition, the lattice mismatch-induced strain stored in the WL requires release, and the formation of QDs is an effective way to release the strain. For the formation of QDs (SK mode), the change in the energy is given by:

$$\Delta E_{SK} = \gamma_s A_1 V^{2/3} - \gamma(\theta_{WL}) A_2 V^{2/3} + \omega_1 \varepsilon_0^2 V - \omega_2 A_3 \varepsilon_0^2 V \tag{2.22}$$

If the growth mode is layer-by-layer growth (2D mode), the change in the energy is mainly caused by a decrease of the surface energy of the WL with an increase of its thickness. Therefore, the change of the energy caused by 2D growth is:

$$\Delta E_{2D} = A[\gamma(\theta_{WL} + kV/h_0) - \gamma(\theta_{WL})] + \omega_1 \varepsilon_0^2 V \tag{2.23}$$

To compare equally between ΔE_{SK} and ΔE_{2D}, the area of the WL used in Eq. (2.23) should be equal to the capture area by a single QD. However, when the substrate is patterned with holes, the expression of the change of the energy caused by 2D growth is influenced not only by the capture area but also by the size of the holes and the distance between the holes. In the following, we discuss the change of the energy by 2D growth and the formation sites of QDs on hole-patterned substrates in two typical cases.

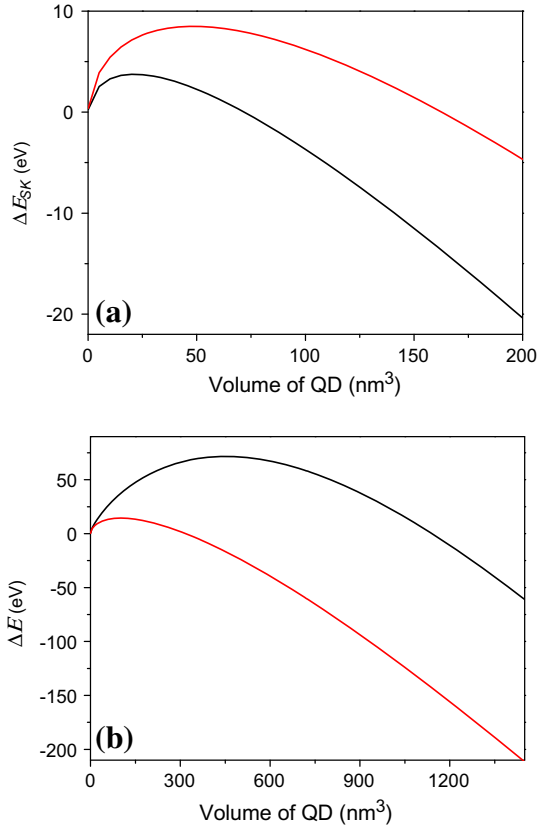

Fig. 21. (a) The comparisons of ΔE_{SK} between on the terrace (black line) and inside the hole (red line) as a function of volume under $\theta_0 = 4$ML. (b) The comparisons of the total energy difference ΔE between on the terrace (black line) and inside the hole (red line) as a function of QD volume [24].

The first typical case is that in which the capture length is larger than the distance between the holes. The total energy difference of the two growth modes, $\Delta E = \Delta E_{SK} - \Delta E_{2D}$, can be written as:

$$\Delta E = [E_{2D}(\theta_0) - E_{2D}(\theta_0 + kV/h_0)] + \gamma_s A_1 V^{2/3} - \gamma(\theta_{WL}) A_2 V^{2/3} - \omega_2 A_3 \varepsilon_0^2 V \tag{2.24}$$

This equation represents the case of QD formation on a terrace between the holes when $\theta_{WL} = \theta_1$, and it represents the case of QD formation on the inside of a hole when $\theta_{WL} = \theta_2$. Fig. 21(a) shows the comparisons of ΔE_{SK} between the two different formation sites when the total deposited amount is equal to 4 ML. It is obvious that the formation energy of a QD on a terrace is lower than that on the inside of a hole, which suggests that it is more favorable for a QD to form on a terrace.

However, when the capture area by the QD is smaller than both the size of a hole and the area of a terrace between the holes, i.e., $A < \pi r^2$ and $A < \pi(d - 2r)^2$, the terrace and the inside of a hole can be considered as separate regions to calculate the change of the energy. Therefore, the total energy difference becomes:

$$\Delta E = A[\gamma(\theta_i) - \gamma(\theta_i + kV/h_0)] + \gamma_s A_1 V^{2/3} - \gamma(\theta_i) A_2 V^{2/3} - \omega_2 A_3 \varepsilon_0^2 V \tag{2.25}$$

where $i = 1$ and $i = 2$ represent the QD formation on a terrace and the inside of a hole, respectively. Fig. 21(b) shows the calculated results. The total energy difference on the inside of a hole is lower than that for a terrace, which is contrary to the case of a large capture area, which suggests that the formation of a QD on the inside of a hole is favored over that on a terrace in the case of a small capture area.

The capture area of the QD and the thickness of the WL determine the two contrary formation sites. When the capture area is larger than that of the lattice of the hole array, the changes of the energy caused by layer-by-layer growth for two formation sites are equal to each other. Therefore, the total energy is mainly determined by the change of the energy caused by the QD formation. Because the thickness of the WL on a terrace is smaller than that on the inside of a hole, the surface energy density of the WL on the terrace is larger than that on the inside of the hole. So, the decrease in the surface energy of the WL caused by the coverage of the QD on the terrace is larger than that on the inside of the hole, which results in the formation energy of the QD on the terrace always being lower than that on the inside of the hole. However, when the surface diffusion length is smaller than half the size of the hole and the terrace, the terrace and the inside of the hole are considered as separate regions to calculate the total energy. In this case, the change of the energy caused by 2D growth plays a key role for the total energy difference, and the WL on the inside of the hole achieves the critical thickness for QD formation first due to its larger thickness than that on the terrace. Therefore, the formation of a QD on the inside of a hole is more favorable in the case of a small capture area for the QD.

The theoretical results explain several interesting and puzzling experiments mentioned at the beginning of this section. One key result of the model is that QDs can form in various sites for various capture areas. From a thermodynamics perspective, a high (low) temperature leads to a low (high) density of QDs, i.e., a large (small) capture area for the QD [66]. Therefore, the theoretical results are consistent with experiments [155,182], in which Ge QDs are organized on the terraces between holes at high temperature (higher than 700 °C) or on the inside of holes at a lower temperature (approximately 550 °C). The modeling results can also explain the various sites caused by the distance between the pattern holes [190]. When the distance between the holes is larger than the surface diffusion length, InAs QDs grow on the inside of the holes. However, when the distance between the holes is reduced, the capture area becomes larger than that of the lattice of the hole array, and therefore, InAs QDs can grow on the mesas between the holes. This model can also explain why the critical thickness of the WL for QD formation on a hole-patterned substrate is smaller than that on a planar substrate [188].

It should be noted that the temperature can influence the surface diffusivity of the deposited atoms, especially at the boundary between two different crystal facets [182]. A low temperature impedes the diffusion from a crystal facet to anther crystal facet, which means that it is difficult to achieve the equilibrium state. In this case, the increased thickness on the inside of a hole would be affected. Beyond that, the temperature also influences the intermixing and the alloying between an epitaxial film and the substrate, which can change the strain relaxation and the surface energy. In the model above, these influences are ignored for simplification.

2.4. Growth of QDs in multilayered systems

The self-assembly of QDs driven by the elastic strain field induced by buried QDs in multilayered systems is another effective approach for improving the uniformity of QDs [196–205]. With an increasing number of spacer layers, the QDs become uniform in size, shape, and spacing. Due to their simple manipulation and low cost, a number of groups have investigated them intensively experimentally. In the initial study, it was found that the interaction between the stacked QDs through the strain fields on the surface of the spacer layer induced by buried QDs leads to one-to-one vertical ordering of QDs. In other words, each QD in the upper layers grows on the top of a QD in the lower layer. The vertical pairing probability of QDs in multilayer structures is better with thinner spacer layers, as shown in Fig. 22. However, the following experiments showed remarkably different results when the thickness of the spacer layer is less than a critical value, demonstrating that the one-to-one vertical alignment of stacked QDs is broken and more than one QD forms on the spacer layer surface instead, i.e., one-to-several ordering of QDs (Fig. 23) [203,204]. The other interesting behavior is the change in the WL thickness. Experimental observations have shown that the critical thickness of the SK growth in the second layer is reduced compared to that of the first one [198–201,205].

To explain the experimental observations, several theories have been established based on analysis of the strain fields on the spacer layer surface. The early studies [196,206] simply consider a buried QD as a force dipole of zero dimension using the continuum theory of elasticity and demonstrate one-to-one vertical ordering of QDs by analyzing the preferential nucleation site at a local maximum of tensile strain fields on the spacer layer surface, i.e., above the buried QD with a local minimum of mismatch. Zhang et al. [207,208] proposed a model to calculate the surface strain using the Green's function method in the framework of the continuum theory of elasticity. They found that the local maxima of the tensile strain field on the spacer layer surface are not at the sites above the buried QDs in the case of very thin spacer layers, which explains the one-to-several ordering of the QDs.

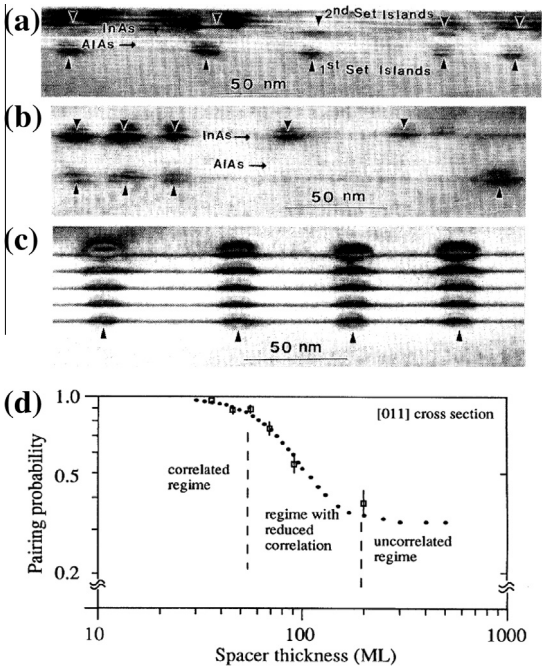

Fig. 22. TEM pictures taken along [0 1 1] azimuth for the InAs QDs separated by GaAs spacer layers with thickness of (a) 46 ML, (b) 92 ML, and (c) 36 ML. (d) is the experimentally observed pairing probabilities (open squares) as a function of the spacer thickness [196].

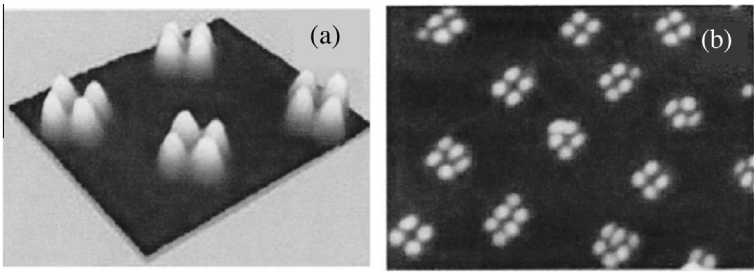

Fig. 23. AFM images of Ge QDs grown at 600 °C in stacked multilayers using Si spacer layer with thicknesses of 35 nm [203].

In addition, some theories adopt simulations, for example, atomistic simulations [209,210] and molecular-dynamics simulations [211], to calculate the strain fields induced by a buried QD. Additionally, Monte Carlo simulations and molecular dynamics simulations have also been performed for the growth of QDs in a multilayer [212–216]. In this section, we first introduce a calculation for the surface chemical potential and the elastic strain on the spacer layer surface in multilayered systems, which can explain the physical mechanisms of the vertical alignment of stacked QDs [217]. Then, we introduce a thermodynamic model of the QDs on a strained substrate, which reveals the driving force of QD formation on strained substrates and explains why the thickness of the WL in multilayered systems is much smaller than that on common substrates [23,218].

2.4.1. Surface chemical potential in multilayered systems

The surface chemical potential determines the most favorable nucleation sites [185]. In multilayered SK systems, the foreign inclusion B is buried in substrate A, and three-dimensional strained QDs C form after the formation of a two-dimensional WL. The strain-dependent surface chemical potential is expressed as [158,196]:

$$\mu(x,y,0) = \mu_0 + \Omega E_s(x,y,0) + \Omega\gamma\kappa \tag{2.26}$$

We first calculate the strain on the surface of the substrate [219] and then obtain the strain energy of the WL surface. The strain on the surface of the WL $(x, y, 0)$ induced by the inclusion can be calculated using the integration of Green's function over the volume of the inclusion V, i.e. [217]:

$$\begin{aligned}
\varepsilon^A_{xx}(x,y,0) &= \frac{\varepsilon_{AB}V(1+\upsilon)}{\pi R^3}\left(1-\frac{3x^2}{R^2}\right)\\
\varepsilon^A_{yy}(x,y,0) &= \frac{\varepsilon_{AB}V(1+\upsilon)}{\pi R^3}\left(1-\frac{3y^2}{R^2}\right)\\
\varepsilon^A_{zz}(x,y,0) &= \frac{\varepsilon_{AB}V(1+\upsilon)}{\pi R^3(1-\upsilon)}\left(\upsilon+\frac{3z_0^2(1-2\upsilon)}{2R^2}\right)\\
\varepsilon^A_{xy}(x,y,0) &= -\frac{6\varepsilon_{AB}V(1+\upsilon)}{\pi R^5}xy\\
\varepsilon^A_{xz}(x,y,0) &= \varepsilon^A_{yz}(x,y,0) = 0
\end{aligned} \tag{2.27}$$

where the inclusion is considered to be located approximately at $(0, 0, z_0)$, V is the volume of the inclusion, and $R = (x^2 + y^2 + z_0^2)^{1/2}$. Thus, the strain energy of the WL becomes:

$$E_s(x,y,0) = \frac{C_{11}}{2}\left[\left(\varepsilon^C_{xx}(x,y,0)\right)^2 + \left(\varepsilon^C_{yy}(x,y,0)\right)^2\right] + C_{12}\varepsilon^C_{xx}(x,y,0)\varepsilon^C_{yy}(x,y,0) + \frac{C_{44}}{2}\left(\varepsilon^C_{xy}(x,y,0)\right)^2 \tag{2.28}$$

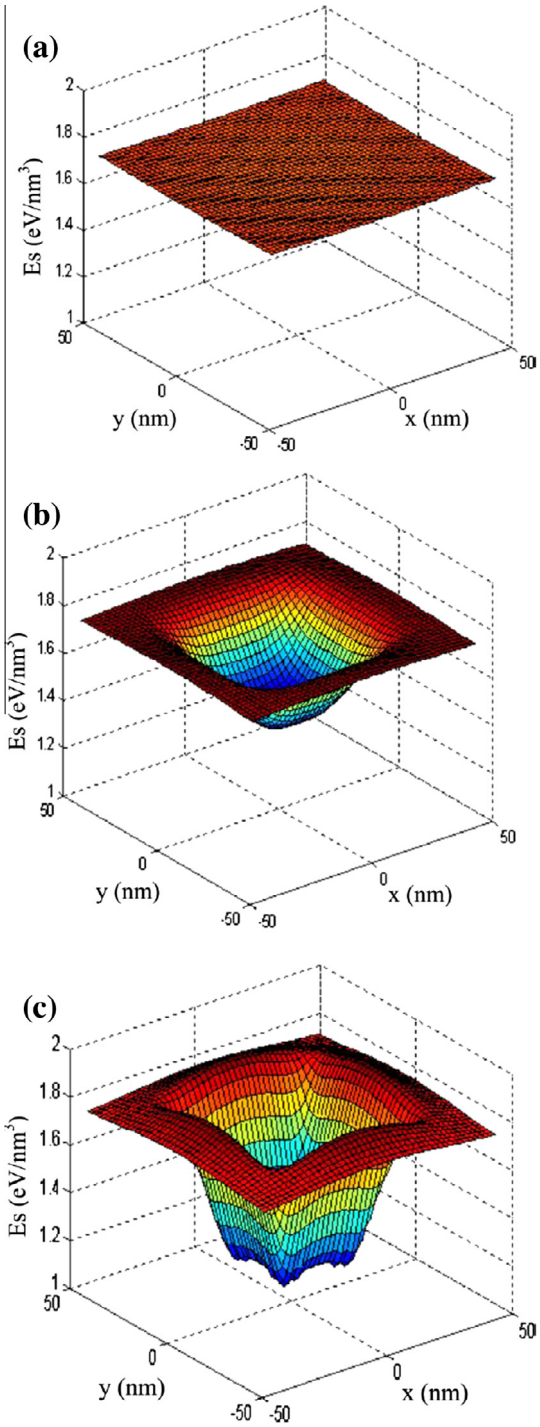

Fig. 24. The calculated strain energy of the WL for different depths of buried Ge QD in the Ge/Si system, (a) 60 nm, (b) 15 nm, and (c) 7.5 nm [217].

Fig. 24 shows the calculated surface chemical potential for a Ge QD buried in a Si substrate. There is a smoothly varying surface chemical potential in the case of the depth z_0 = 60 nm, as shown in Fig. 24 (a). However, when a Ge QD is buried at a depth z_0 = 15 nm, the surface chemical potential obviously has a minimum at the point above the buried QD (Fig. 24(b)), which means the deposited atoms can be driven to reach the region above the buried QD by gradation of the surface chemical potential and to nucleate easily in the region. Furthermore, the minimum value of the surface chemical potential is smaller with a deeper buried QD. The results are in good agreement with the experimental observations [196–198,202]. However, when the depth of the buried QD is z_0 = 7.5 nm, we find that the minimum surface chemical potential occurs at the edge of the region above the buried QD, which results in an annular distribution of the surface chemical potential (Fig. 24(c)). The annular distribution drives the deposited atoms to nucleate in the annular valley of the potential field and can form one-to-several ordering of QDs. The modeling results are in good agreement with the results of experiments, in which one-to-one vertical alignment of stacked QDs is broken and more than one QD forms on the spacer layer surface when the depth of the buried QD is less than a critical value [203,204].

According to the model, we propose several anticipated applications by selecting properly buried inclusions. For example, we expect that QRs can be fabricated by obtaining the annular distribution of the minimum of surface chemical potential in the case of $a_B > a_C > a_A$, such as Sn inclusions buried in a Ge/Si system [220]. Additionally, we can perhaps realize control of the nucleation of QDs from the microscale to the nanoscale. In detail, we can lithograph or chemical etch a heterogeneous material with a certain shape at the microscale on the surface of a substrate and then deposit a spacer layer with a proper thickness. QDs form easily in the region with the lowest surface chemical potential on the planar surface of the spacer layer. The region with the lowest surface chemical potential can be controlled by the inclusions [217].

2.4.2. Thermodynamics model of QDs on a strained substrate

In the multilayer structures of QDs, apart from the vertical distribution of stacked QDs, the thickness of the WL decreases and the size of QD increases relative to that on unstrained substrates when the total deposition is identical. These differences are also caused by the local strain fields induced by buried QDs.

Based on the model in Section 2.1.2 for an existing WL with a certain thickness, we can compare the changes of the energy caused by the two growth modes, layer-by-layer growth and QD formation, to identify which growth mode is favored, as shown in Fig. 3. Because of the influence of the foreign objects, the surface strain of the substrates has an uneven distribution, and the nucleation of QDs usually occurs in the region with the lowest strain mismatch. The strain energies of the QDs and the WL can be calculated by the average strain mismatch, $\bar{\varepsilon}_{QD}$ and $\bar{\varepsilon}_{WL}$. Therefore, the change of the energy in the case of the layer-by-layer growth mode on a strained substrate becomes:

$$\Delta E_A = \frac{1}{k}[\gamma(\theta_{WL} + kV/h_0) - \gamma(\theta_{WL})] + \omega_1 \bar{\varepsilon}_{WL}^2 V \tag{2.29}$$

The change in the strain energy of a QD is divided into the strain energy excluding the elastic relaxation energy and including the elastic relaxation energy, which can be expressed as ($\omega_1 \bar{\varepsilon}_{QD}^2 V - \omega_2 A_3 \bar{\varepsilon}_{QD}^2 V$). Therefore, the change in the total energy caused by the formation of a single QD is:

$$\Delta E_B = \left[\gamma_s A_1 V^{2/3} - \gamma(\theta_{WL}) A_2 V^{2/3}\right] + (\omega_1 \bar{\varepsilon}_{QD}^2 V - \omega_2 A_3 \bar{\varepsilon}_{QD}^2 V) \tag{2.30}$$

Therefore, the total energy difference between the formation of a QD and the layer-by-layer growth on the strained substrate is:

$$\begin{aligned}\Delta E = {} & \frac{1}{k}[\gamma(\theta_{WL}) - \gamma(\theta_{WL} + kV/h_0)] + \left[\gamma_s A_1 V^{2/3} - \gamma(\theta_{WL}) A_2 V^{2/3}\right] \\ & - \left[\omega_1(\bar{\varepsilon}_{WL}^2 - \bar{\varepsilon}_{QD}^2)V + \omega_2 A_3 \bar{\varepsilon}_{QD}^2 V\right]\end{aligned} \tag{2.31}$$

We can obtain the energy barrier (maximum of Eq. (2.31), ΔE_c) and the critical QD volume (V_c) according to the equation. Using the approximate relation of the surface energy density of the WL with its thickness [21], we obtain the energy barrier and the critical volume as [23]:

$$\Delta E_c = \frac{4N^3}{27M^2}; \quad V_c = \frac{8N^3}{27M^3} \tag{2.32}$$

where $M = [\omega_1(\bar{\varepsilon}_{WL}^2 - \bar{\varepsilon}_{QD}^2) + \omega_2 A_3 \bar{\varepsilon}_{QD}^2] - e^{-\theta_{WL}/\eta}(\gamma_{substrate}^{\infty} - \gamma_{WL}^{\infty})/\eta h_0$ and $N = \gamma_s A_1 - \gamma(\theta_{WL})A_2$.

Fig. 25 shows the calculated results for the dependence of the barrier energy (ΔE_c) and the critical size (critical width at the base, s_c) on the strain and the thickness of the WL for the Ge/Si system. We find that both ΔE_c and s_c decrease with decreasing $\bar{\varepsilon}_{QD}$ and increasing θ_{WL}. For a given θ_{WL}, the driving force of QD formation, $-\left[\omega_1(\bar{\varepsilon}_{WL}^2 - \bar{\varepsilon}_{QD}^2)V + \omega_2 A_3 \bar{\varepsilon}_{QD}^2 V\right]$, becomes stronger with decreasing $\bar{\varepsilon}_{QD}$, so that the QD can form much more easily with a strong driving force. On the other hand, for a given $\bar{\varepsilon}_{QD}$, both ΔE_c and s_c decrease with increasing θ_{WL}, which means that it is favored for QDs to form on the thicker WL. It is interesting and important to note that QDs scarcely form on the WL with a thickness less than 4 ML if the value of $\bar{\varepsilon}_{QD}$ is close to that of $\bar{\varepsilon}_{WL}$. However, for a small $\bar{\varepsilon}_{QD}$, QDs can still form on the WL with a smaller thickness, and the energy barrier and the critical size are also obviously lower than that of a large $\bar{\varepsilon}_{QD}$, which means that the QD formation on strained substrates usually begins much earlier

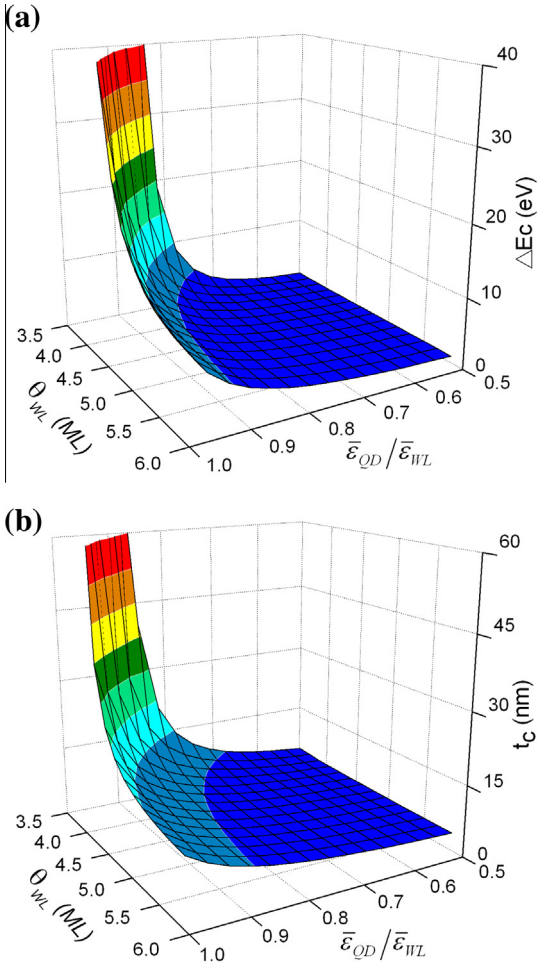

Fig. 25. The calculated barrier energy (a) and critical size (b) as a function of the strain ($\bar{\varepsilon}_{QD}/\bar{\varepsilon}_{WL}$) and the thickness of WL (θ_{WL}) for Ge/Si system [23].

than that on common substrates without extra strain. The calculated results are in good agreement with the experimental observations by various groups [198,199].

We can also investigate the stability and the evolution mechanism of QDs on strained substrates by Eq. (2.31) [218]. Fig. 26 gives the three-dimensional graphs of the stable thickness of the WL as functions of $\bar{\varepsilon}_{QD}/\bar{\varepsilon}_{WL}$ and the deposited amount. Clearly, we find that although the deposited amounts increase, the stable WL does not become thicker but thins when the value of $\bar{\varepsilon}_{QD}/\bar{\varepsilon}_{WL}$ is a constant. These interesting results are in good agreement with experimental observations by various groups [72,129,130], in which it is observed that Ge atoms move from the WL into QDs and the WL becomes thinner during growth and annealing. From the results, we deduce that the QDs become large and the WL becomes thin as the value of $\bar{\varepsilon}_{QD}/\bar{\varepsilon}_{WL}$ decreases under identical deposition amounts. The theoretical results have also been supported and demonstrated experimentally, in which the top QD in multilayered Ge/Si systems is usually larger than the buried QD, and the thickness of the WL on the top layer is usually smaller than that of the WL at the lower layer under identical deposition conditions [198–200]. Similar theoretical results can also be obtained by analyzing the balance between the energies of the QD and the WL [221].

Based on the quantitative thermodynamic theory, we find that the driving force for QD formation on strained substrates is different from that on common substrates. The decrease in the strain energy of the QDs drives QD formation to begin much earlier than that on common substrates, and the energy barrier and the critical size of the QDs on the strained substrates are smaller than those on common substrates. Additionally, the increase in the driving force of the QD growth leads to QDs with larger sizes and a thinner WL than in multilayered systems.

2.5. Compositional mapping of QDs

The inhomogeneous distribution of the composition in the QDs in most of the models above has not been considered. In fact, intermixing and alloying can allow for a partial strain relaxation in the growing film [222–226]. Because the unique properties of the QDs, such as the photoluminescence emission wavelength [11], depend on the detailed compositional mapping of QDs, the investigations of the composition of QDs are highly important for potential applications. In the past decade, much work has been devoted to the elucidation of the compositional mapping of QDs due to intermixing and alloying [226]. In experiments, intermixing of elements in QDs has been investigated by various techniques, including transmission electron microscopy [222,227], X-ray diffraction [228–233], photoelectron microscopy [234], ion-atom probes [235], scanning probe microscopy [236], and so on. Meanwhile, much theoretical work has been devoted to the elucidation of the compositional

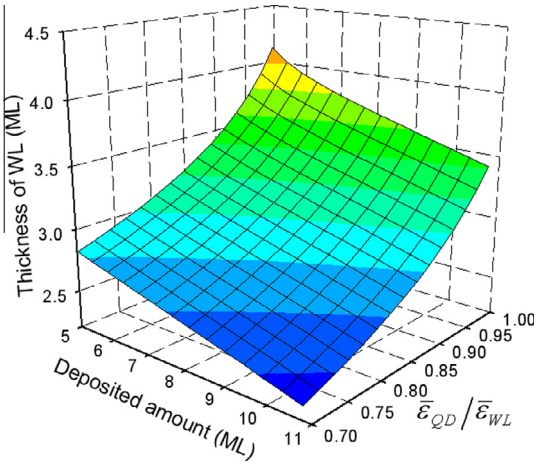

Fig. 26. Three-dimensional graphs of steady thickness of WL as functions of values of $\bar{\varepsilon}_{QD}/\bar{\varepsilon}_{WL}$ and deposited amount [218].

profile in the QDs due to intermixing and alloying, such as, finite-element methods [237,238], numerical simulations [239,240], continuum models [241], and Monte-Carlo simulations [151,242,243]. In this section, we review mainly the theoretical aspects of alloying in quantum dots under strain using finite element methods [237], and numerical simulations [239].

2.5.1. Finite element method

At equilibrium, the compositional profile of a QD with a given size, shape, and average composition is obtained by minimizing the total free energy that consists of the elastic energy and the entropic and chemical-mixing energies [237]. For an *AB* alloy QD grown epitaxially onto a substrate of species *A*, the total free energy E can be written as $E = E_{ch} + E_{el} + E_s$ [237], in which E_{ch} is the chemical free energy of the alloy components in the QD, E_{el} is the elastic-strain energy due to the lattice mismatch between the QD and the substrate, and E_s is the surface-energy cost involved in the formation of the QD. The elastic energy of the QD-substrate system and the chemical free energy of the alloy components can be written as [237]:

$$E_{ch} + E_{el} = M\varepsilon_m^2 V_d \widehat{W}(\bar{c}, \theta, F_0) \tag{2.33}$$

where M is the biaxial modulus, ε_m is the equibiaxial mismatch strain arising due to the difference in the lattice constants between species *A* and *B*, $\widehat{W}$ is a dimensionless function, and V_d is the volume of the QD. If the surface energy γ of QD is assumed to be independent of the facet angle θ, the total energy of an alloy dot can then be expressed as [237]:

$$E = M\varepsilon_m^2 V_d \widehat{W}(\bar{c}, \theta, F_0) + \gamma V_d^{2/3} \widehat{\Gamma}(\theta) \tag{2.34}$$

where $\widehat{\Gamma}(\theta) = \pi^{1/3} 3^{2/3} (\tan\theta)^{-2/3} (\sqrt{1 + \tan^2\theta} - 1)$.

Fig. 27 shows the computed equilibrium compositional maps in dome-shaped and truncated-pyramidal QDs. We find that the compositional profiles of the QDs with thermodynamically favorable mixing depend strongly on the slopes of the QDs and the curvature of their surfaces. The distinguishing feature of these QDs is the complex pattern of isocompositional profiles that can be attributed to the presence of "corners" formed by the intersection of various facets. Because such corners allow for the relaxation of mismatch strain, the free energy can be lowered by segregation of the larger alloy component in these regions.

2.5.2. Numerical simulations

Consider a three-dimensional alloy QD made of two elements A and B, as schematically represented in Fig. 28(a), which is immersed in a mixed vapor phase of A and B. When the growth of the QD is modeled in the surface-attachment-limited kinetics (SALK) regime, the surface evolution is governed by the difference in the chemical potential between the solid and the vapor phase. The chemical potentials for A and B at the QD surfaces are [239,244]:

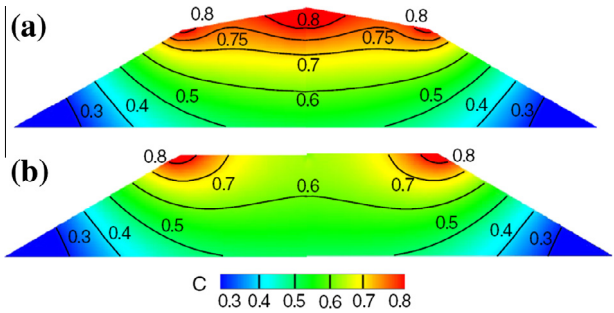

Fig. 27. Equilibrium composition profiles in axisymmetric QDs with (a) dome shape, the angles of the sidewalls being 30° and 15°, and (b) a truncated-cone shape with a sidewall angle of 30° [237].

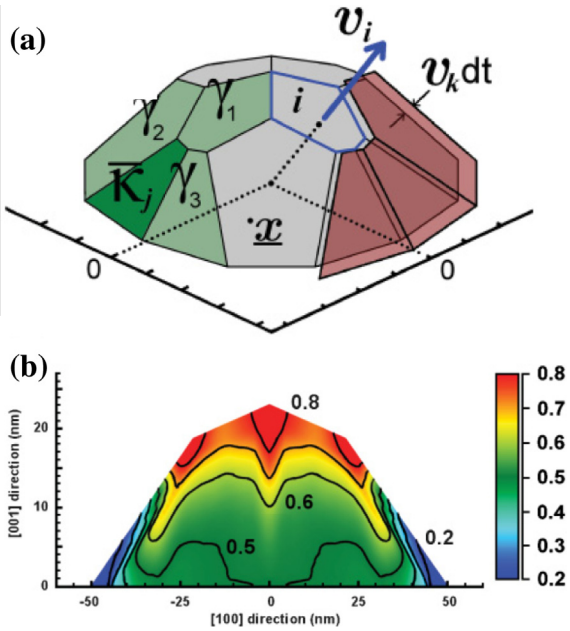

Fig. 28. (a) Illustration of a typical dot shape (dome QD in Ge/Si heteroepitaxy) showing how the change of one facet surface energy, κj, relates to the surface energies of that facet and its surrounding ones. (b) Cross-sectional composition profile of a SiGe dome QD on Si substrate using the numerical simulation [239].

$$\mu_{Ai}(x,t) = \alpha_i(x,t) - \zeta(x,t)\beta_i(x,t)$$

$$\mu_{Bi}(x,t) = \alpha_i(x,t) + [1-\zeta(x,t)]\beta_i(x,t) \tag{2.35}$$

where $\alpha_i(x,t)$ and $\beta_i(x,t)$ represent the contributions from the intrinsic element and the element change.

When atoms are deposited onto the surface, the facets move with a given velocity and evolution consistent with the decrease in the Gibbs free energy. The normal velocities of the individual atoms of the component facet give the following relations [239,244]:

$$v_{Ai}(x,t) = M_A(\mu_A^0 - \bar{\mu}_{Ai}) + \frac{1}{4}(M_A + M_B)[\beta_i(x,t) - \bar{\beta}_i]$$

$$v_{Bi}(x,t) = M_B(\mu_B^0 - \bar{\mu}_{Bi}) - \frac{1}{4}(M_A + M_B)[\beta_i(x,t) - \bar{\beta}_i] \tag{2.36}$$

where $\bar{\mu}_{Ai}$ and $\bar{\mu}_{Bi}$ are the averages of μ_{Ai} and μ_{Bi} over facet i, respectively. The parameters M_A and M_B are the attachment rates of species A and B, respectively. In the model, the attachment rates are assumed to be independent of the crystalline orientation.

Considering the vapor phase surrounding the crystal in the SALK regime, material incorporates at a constant rate (volume per unit time) R_A and R_B for each species independently. So, the composition of the depositing material is $R_B/(R_A + R_B)$. For attachment rates independent of facet orientation, the chemical potentials for A and B are [239,244]

$$\mu_A^0 = \frac{1}{S_{TOT}}\left(\sum_{i=1}^{N} S_i\bar{\mu}_{Ai} + \frac{R_A}{M_A}\right) \quad \text{and} \quad \mu_B^0 = \frac{1}{S_{TOT}}\left(\sum_{i=1}^{N} S_i\bar{\mu}_{Bi} + \frac{R_B}{M_B}\right) \tag{2.37}$$

where S_{TOT} is the total surface area exposed by the crystal. If we assume that material intermixing only occurs within a thin surface layer and the surface is advancing, the composition evolves as [239]

$$\delta\frac{\partial\zeta}{\partial t} = v_{Bi}(x,t) - \zeta(x,t)\,v_i(t) \tag{2.38}$$

where, $v_i(t) = v_A(x,t) + v_B(x,t)$ is the total velocity of facet i. The set of equations above represents the governing equations that are used in the model. Using the numerical scheme developed by Vastola et al. that is able to solve this set of coupled equations, the crystal growth dynamics can be illustrated [239].

Fig. 28(b) shows the cross-sectional compositional profile of a SiGe dome QD on a Si substrate using the numerical simulation. The segregation of the species with the larger lattice parameter (Ge) occurs at the top of the QD and along the edges. At the same time, the species with the smaller lattice parameter (Si) locates at the lower corners and the base of the QD. This redistribution allows for a lowering of the elastic energy of the crystal, and is consistent with the results shown in other works [237,245,246] and experiments [236,247,248]. Experimental measurements showed that Ge atoms accumulate at the top of the QD and silicon atoms prefer to stay at the bottom. The composition at the central part of the island appears to be relatively uniform with a composition close to the average between the top and the bottom of the QDs [236,247,248].

2.6. Kinetic models for the self-assembly of QDs

The kinetic approach is a basic one in the theoretical description of crystal growth. The formation and subsequent evolution of QDs have been investigated using kinetic considerations [63,110,249–257]. The importance of strain effects in the kinetics of growth has been recognized for a number of growth-related phenomena. Kinetic approaches have been used to investigate the size [110,252,256,257], coarsening [249–251], composition [251,253,254], and instability of the QDs [250,251]. In addition, the growth kinetics are also used to study the position of QDs on patterned substrate [255]. In this section, we review mainly the kinetic models of the coarsening, composition and instability of QDs.

2.6.1. Coarsening of QDs

Coarsening is a competitive growth process wherein some QDs grow at the expense of others to minimize total surface energy. The result of coarsening is that the mean QD volume increases with time, and the number of QDs per unit area simultaneously decreases [249]. The chemical potential for ripening can be given by $\Delta\mu(V) = B[V^{-1/3} + p(\theta)]$, where B sets the energy scale, V is the volume of a QD, and $p(\theta)$ represents the contribution of the elastic interaction energy that can be calculated using the finite-element method [249]. Therefore, the growth rate of any class of QDs of size V is [67,249]:

$$\frac{dV}{dt} = cV^{1/3}\left[e^{\Delta\mu^*/kT} - e^{\Delta\mu(V)/kT}\right] \tag{2.39}$$

where c is a constant, kT is as usual, and $\Delta\mu^*$ is specified by the conservation of mass:

$$\int_0^\infty f(V,t)\dot{V}dV = \Phi \tag{2.40}$$

where $f(V,t)$ is the distribution of island volumes, and Φ is the deposition rate. Finally, the evolution of $f(V,t)$ is obtained from the flux continuity equation in size space [249]:

$$\frac{\partial f}{\partial t} = -\frac{\partial(f\dot{V})}{\partial V} \tag{2.41}$$

The equation can be solved numerically [68]. From $f(V,t)$, we directly obtain the mean areal volume $\langle V(t)\rangle$ and the number density $\langle N(t)\rangle$. Fig. 29(a) shows the results when we do not consider the contribution of the elastic interaction energy ($p(\theta) = 0$). For pure ripening ($\Phi = 0$), $\langle V(t)\rangle$ increases linearly, and $\langle N(t)\rangle$ decays with a positive second derivative. The results are consistent with post-growth coarsening during annealing in experiments [249]. However, for a large Φ, $\langle V(t)\rangle$ again increases linearly with time, whereas $\langle N(t)\rangle$ decreases very slowly with time, again as expected. For an intermediate

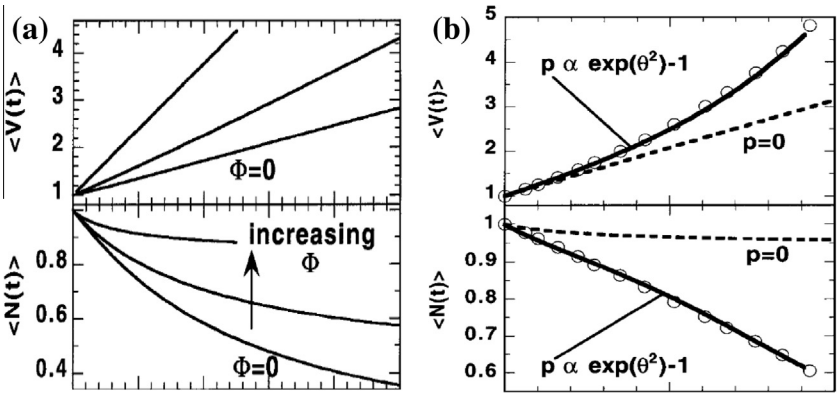

Fig. 29. (a) Mean field model results showing effect of deposition flux, Φ, where elastic interactions is not considered ($p(\theta) = 0$). (b) Mean field model results incorporating elastic interactions at large Φ (solid line). Also shown for reference is $p(\theta) = 0$, i.e., no elastic interactions, but the same Φ (dashed line). The open circles are the experimental data, scaled for comparison [249].

Φ, $\langle N(t)\rangle$ still decays with a positive curvature. Thus, pure capillarity-driven ripening ($p(\theta) = 0$), even in the presence of a deposition flux, cannot reproduce the essential experimental results. When we consider the contribution of the elastic interaction energy, i.e., $p(\theta) > 0$, we can obtain the expected results that elastic interactions promote both super-linearity in $\langle V(t)\rangle$ and the decay of $\langle N(t)\rangle$ with a negative curvature (Fig. 29(b)), which is consistent with experimental observations [249].

According to the results of the kinetic model, we know that Ostwald ripening is enhanced by the elastic repulsion energy between the islands, coupled with deposition that forces the islands closer together, thereby increasing the system energy. Elastic repulsion effects are important for a high volumetric density of precipitates [249].

2.6.2. Instability of QDs

The growth and the evolution of QDs are complex. Taking the Ge/Si system as an example, there is an instability that the most unstable wavelength is proportional to $1/x$ and not $1/x^2$ when the difference in the mobility between Si and Ge is accounted for in the limit of nearly immobile Si atoms [14,241]. Several kinetic models have been established to study the instability of QDs, including the strain/composition in epitaxial films [258,259], the compositional map of small pre-pyramid QD [260], the critical thickness for QD growth [250], and the mobility of QDs [251].

During the typical growth process of an epitaxial film, the system evolves by surface diffusion, and bulk diffusion is assumed to be negligible [250,251,261,262]. One can assume that atoms at a depth w_s (perhaps 2–4 monolayers) are in equilibrium with the surface because atoms within a few atomic layers of the surface are generally more mobile than in the bulk [241]. The free energy of this surface region g_s may be different than the bulk free energy function g_b, and any difference drives surface segregation [250,251], in which g_s is a function of the surface composition averaged over the depth w_s, i.e., ξ. In this case, the composition and the morphology evolve as coupled equations [250,251]:

$$\upsilon = \sum_{\upsilon}[F_\upsilon + \nabla\cdot(D_\upsilon \nabla\mu_\upsilon)] \tag{2.42}$$

$$w_s \frac{d\xi_\upsilon}{dt} = F_\upsilon + \nabla\cdot(D_\upsilon\nabla\mu_\upsilon) - \xi_\upsilon\upsilon \tag{2.43}$$

Here the subscript υ labels the two alloy components. F_υ is the incident flux of each component, D_υ is the diffusivity, and υ is the local growth velocity of the surface normal to itself.

Fig. 30 shows the simulation results of Ge growth on Si(001) at 600 °C. During the first deposition to form a thin Ge film, a degree of intermixing is visible, as well as the formation of a thin Ge-rich surface layer due to surface segregation, as shown in Fig. 30(a). With increasing time, ripples grow

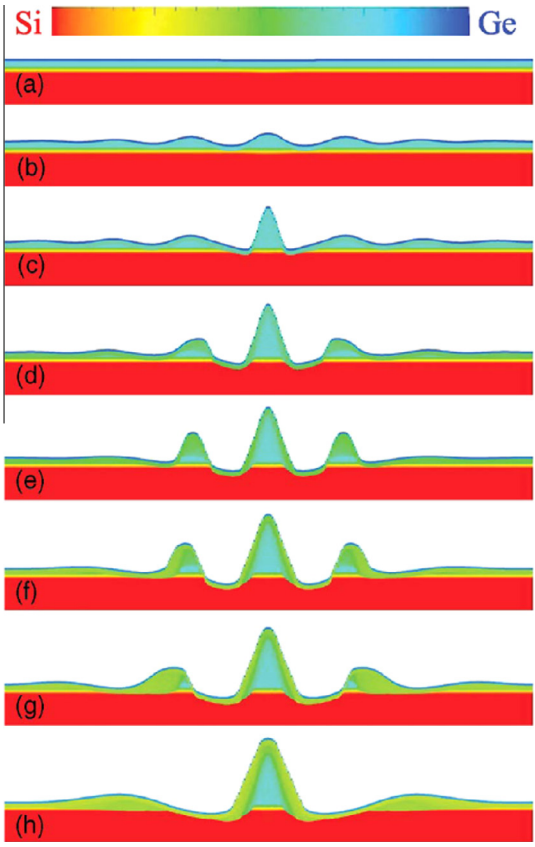

Fig. 30. Selected snapshots from the simulation. Taking the beginning of deposition as $t = 0$, images (a–h) correspond to times 3 (end of deposition), 12, 14, 19, 23, 29, 35, and 161, respectively, in arbitrary units. The width of the images is 410 nm, one unit cell of our periodic system [251].

and trenches start to form; see Fig. 30(b). Beginning with Fig. 30(c), trenches form around the largest QD, digging into the substrate (Fig. 30(d)). After the penetration of the trench into the substrate, the ejected Si mixes with the Ge of the growing dot in the outer layer of the QDs, which leads to the lateral motion of QDs, as shown in Fig. 30(e)–(h). The kinetic results show a complex response to the rather simple thermodynamic driving forces.

2.7. Conclusion

The growth of QDs seems to be simple, but it has led to a surprisingly rich complexity since its discovery more than thirty years ago. The detailed growth of QDs, such as their formation, stability, shape, and position, can be understood by thermodynamic theory. Thermodynamic theory can provide a fundamental understanding for the growth and self-organization of QDs by epitaxy. In this section, we have given a comprehensive overview of the thermodynamic models of the growth of QDs by epitaxy.

However, some questions remain open. Coherently strained, 3D QDs usually have an inhomogeneous composition. The inhomogeneous distribution of the composition can be caused not only by intermixing of QDs with the substrate but also by their own alloys (e.g., Ge_xSi_{1-x} and $In_xGa_{1-x}As$ QDs). Although some theoretical models have been created to compute the equilibrium compositional profiles in strained QDs [233,237,263] (experimental work on the compositional mapping of QDs has

been reviewed in Ref. [264]), the distribution of the QD composition is not well understood. Due to the effects of intermixing, the elastic strain energy will be partly released, which would result in the increase of the critical thickness for the 2D to 3D transition. Additionally, the surface chemical potential can be influenced by the intermixing and alloying between an epitaxial film and its substrate. For example, surface segregation results in a decrease in the surface energy, which drives the atoms of the element with lower surface energy to segregate at the surface. The extension of the existing theory to consideration of the distribution of QD compositions will allow us to describe experimental systems more accurately. In addition, the effect of patterned substrates on QD ordering is still not well understood. A patterned substrate has a multi-faceted surface, which results in a heterogeneous surface energy and a complicated interface between the QDs and the substrate. However, the multi-faceted surface also leads to a discontinuity of the surface diffusion coefficient. These multiple factors influence the final formation sites of the QDs. Several puzzling experimental observations are still under debate. Further investigations in both theories and experiments are therefore necessary to provide a clear interpretation of these results.

3. Growth of QRs by droplet epitaxy

In recent years, semiconductor quantum rings (QRs) have become the focus of intensive research because they provide ideal systems for potential applications in nanodevices. Because of their particular topology, ring nanostructures show unique electronic, optical, and magnetic properties. [265–267]. To attain perfect QRs, various methods have been employed to control the sizes and shapes of QRs in the past few years. For instance, the lithographic technique has been used to fabricate ring structures. However, this technique has a drawback for the fabrication of small rings. Self-organization technology with a cap layer is another fabrication [268–271]. However, this technique has a drawback for the fabrication of small rings. Self-organization technology with a cap layer is another fabrication. [148,272]. However, this technology is only suitable for the lattice-mismatched system, and the strain induced by the additional cap layer has effects on the physical properties of QRs. Recently, droplet epitaxy has been intensively investigated as an important self-assembly technique of semiconductor QRs in lattice-matched systems, such as GaAs/AlGaAs [13,273–281] and in lattice-mismatched systems, such as InGaAs/GaAs. [274,282,283].

The fabrication of QRs by droplet epitaxy is divided into two stages. The first stage is the deposition of III-column element atoms with a low melting point to form liquid droplets with a uniform size of less than 100 nm on the substrate surface, and the second stage is the supply of a V-column element molecular beam to crystallize with liquid droplets. In detail, using the GaAs system as an example, the liquid Ga droplets first form on the substrate surface by depositing Ga atoms in the absence of As flux at the first stage, and then the As flux is supplied to crystallize with Ga droplets. By controlling the intensity of the As flux and the crystallization temperature, four nanostructures, including a dot [273,277,283], a single ring [13,273,277], double rings [13,274,276,278], and a hole [275,276,279,280,282,284] can be obtained, as shown in Fig. 31. The present method of employing strain-free nanostructures is applicable to high-efficiency intermediate-band solar cells, long-wavelength infrared detectors, and light emission devices [8,285–289].

Some theoretical models of droplet epitaxy have been presented [22,36,290–296]. In this section, we introduce the thermodynamic and kinetic issues concerning the growth of QRs by droplet epitaxy.

3.1. Growth mechanisms of QRs

Based on experimental observations, QR formation by droplet epitaxy is determined by two factors, QR nucleation and the growth of QR nuclei at the expense of the droplet. Therefore, nucleation thermodynamics and growth kinetics can be used to investigate the two above-mentioned issues, respectively.

3.1.1. Thermodynamic approach

If the temperature is high enough to neglect the bulk diffusion of As atoms into droplets, then there are three confirmable nucleation sites: one on the surface of the Ga droplet (situation A); one on the

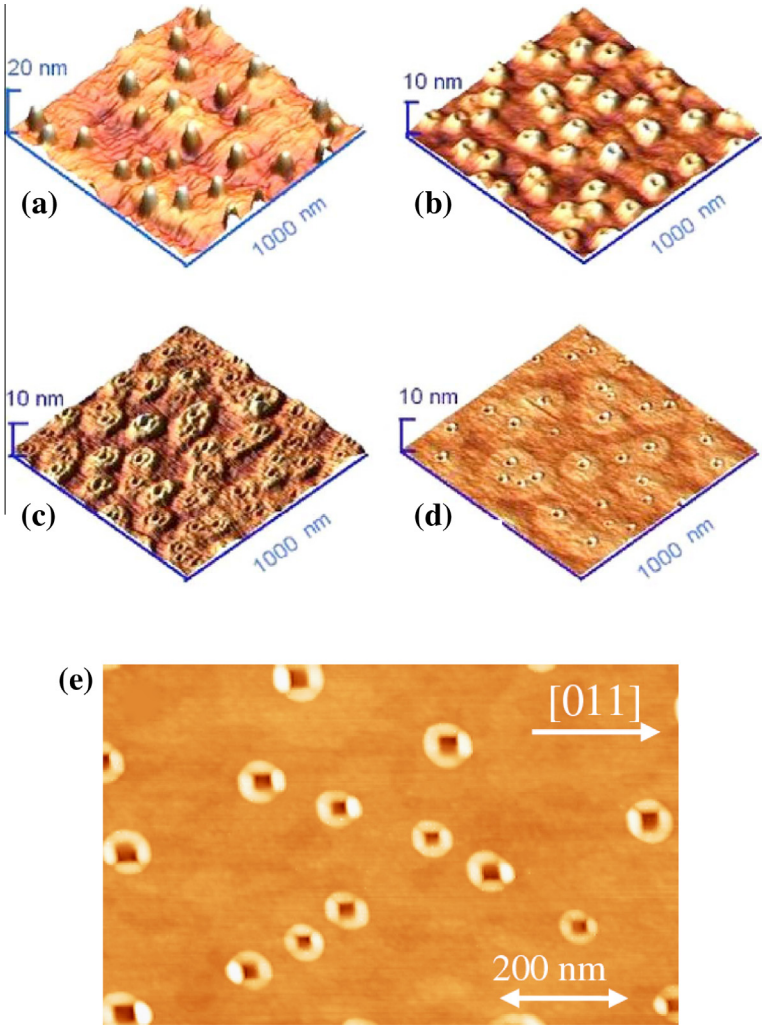

Fig. 31. AFM image of the (a) Ga droplets, and (b–e) the surfaces after crystallization with As flux. (b) single ring, (c) and (d) double rings, and (e) hole. (a–d) are cited from Ref. [274], and (e) is cited from Ref. [275].

skirt of the Ga droplet (situation B); and one on the substrate surface (situation C), as shown in Fig. 32. Thus, we compare the energies of the three sites to clarify which nucleation site is energetically preferable. Based on the nucleation thermodynamics [15,22,186,297], Fig. 32 shows a comparison of the Gibbs free energy difference of the three nucleation sites. Clearly, situation B has the lowest Gibbs free energy difference among the three situations, which definitely indicates that the nucleation on the skirt of the Ga droplet is energetically preferable. The physical origin of the preferable nucleation on the skirt of the Ga droplet is because the high surface energy density of the droplet causes the nucleation around the droplet, which can depress the total surface energy of droplet. The preferable nucleation on the skirt of the Ga droplet results in the possibility of QR formation.

3.1.2. Kinetic growth

Although the thermodynamic nucleation on the skirt of the Ga droplet creates a possibility of QR formation by droplet epitaxy, kinetic growth determines the final shape of nanostructures. The

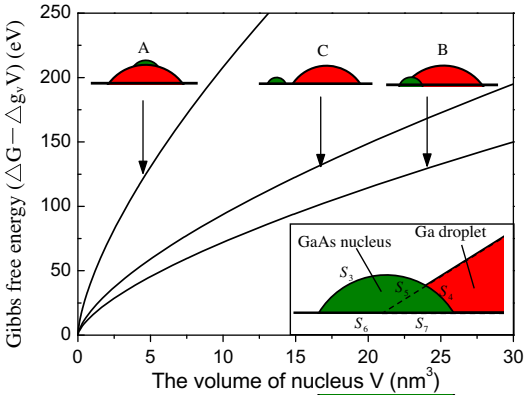

Fig. 32. Gibbs free energy difference ($\Delta G - \Delta g_v V$) as a function of the GaAs nucleus volume for three nucleation sites. The inset is the schematic diagram of the GaAs nucleation (green region) on the skirt of the Ga droplet (red region) [22].

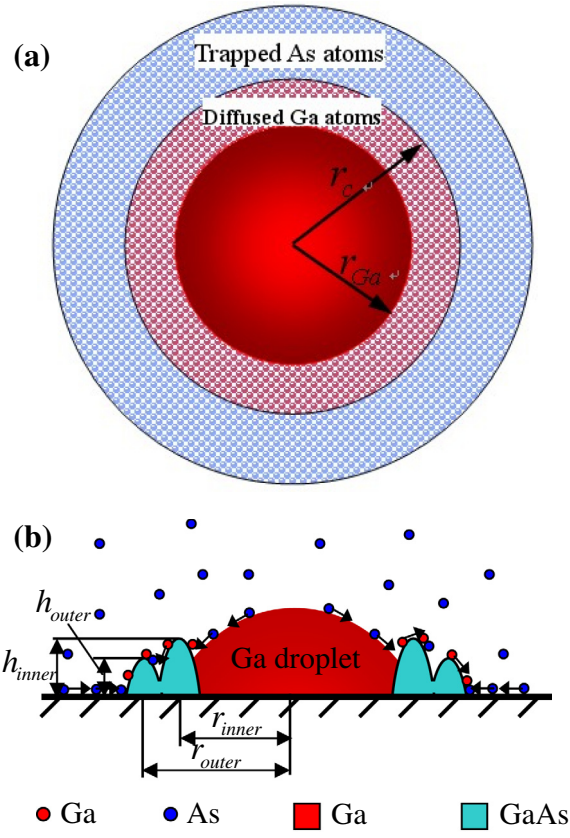

Fig. 33. (a) Schematic illustration of the kinetic diffusion of Ga and trapped As atoms. (b) Schematic illustration of the crystallization process of Ga droplet with As ambience [295].

diffusion of Ga atoms and the trapping of As atoms play key roles in the final morphology of GaAs nanostructures.

To analyze the diffusion of Ga atoms and the trapping of As atoms, we assume that there is a diffusion region around the droplet where all of the migratory Ga atoms from the droplet are limited in the region and crystallize with the trapped As atoms. In this case, the substrate surface is divided into three regions. The first region is the surface of the Ga droplet; the second region is the diffusion region of Ga atoms; and the last region is the trapped region of As atoms, as shown in Fig. 33(a). Atoms deposited on the droplet surface can arrive at the boundary of the droplet via surface diffusion and then crystallize with Ga atoms at the boundary of the droplet. In addition, diffused Ga atoms can crystallize with the trapped As atoms at the periphery of the diffusion region of Ga atoms, as shown in Fig. 33(b).

The final shapes of GaAs structures are strongly influenced by the size of the diffusion region of Ga atoms. The size of the diffusion region can be written as follows [22,293–295]:

$$r_c/r_{Ga} = lambertw\left\{\exp\left[\frac{h_0 D_{0Ga} C_0 \upsilon_0 \sqrt{2\pi mkT}\exp(\Delta E/kT)}{a_0 \upsilon_1 r_{Ga} P}\right]\right\} \tag{3.1}$$

where *lambertw*(x) represents the Lambert W function. Because *lambertw*(x) is a monotone increasing function, the values of r_c/r_{Ga} increase with an increasing growth temperature or with a decreasing intensity of the As flux. The value of r_c determines the outermost boundary of final GaAs quantum structures, and the size of the droplet determines the inner ring of GaAs quantum structures [23]. Therefore, we can control the size of final GaAs quantum structures through regulating the temperature and the intensity of the As flux.

Fig. 34 shows the values of r_c/r_{Ga} as a function of the growth temperature and of the As flux intensity. We find that the high temperature and the low pressure lead to the r_c/r_{Ga} increasing, and in contrast, the low temperature and the high pressure result in the r_c/r_{Ga} decreasing. Correspondingly, three types of GaAs quantum structures, a single ring, double rings and a holed structure, are fabricated as r_c/r_{Ga} increases. Three characteristic shape phase regions can be identified according to the numerical value of r_c/r_{Ga}. In the case of low growth temperature and high As flux, diffused Ga atoms away from the droplet are confined on the skirt of the Ga droplet, which results in the growth of GaAs on the skirt droplet and in the formation of a single ring. When the growth temperature increases and the As flux intensity becomes low, then the diffusivity of Ga atoms becomes strong, and the trapping ability of As atoms decreases, which results in the size of the diffusion region of Ga atoms (r_c) becoming much larger than the size of the droplet (r_{Ga}). The rapid growth at the boundary of the diffusion region of Ga atoms leads to the formation of the outer ring. In this case, concentric double rings can be fabricated. However, as the growth temperature further increases and as the As flux intensity decreases, the outer ring should disappear once r_c becomes large enough to exceed the distance

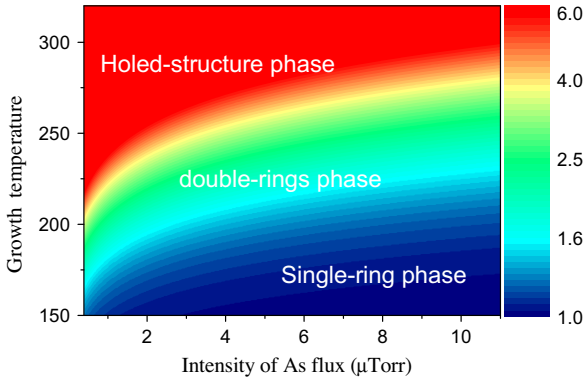

Fig. 34. A two-dimensional phase diagram on the (T–P) plane characterizes the interrelated effects of growth temperature and intensity of As flux on the final shapes of GaAs quantum structures. The color represents the calculated values of r_c/r_{Ga} [295].

between droplets, which leads to a hole. These theoretical investigations are qualitatively consistent with experimental observations [13,273,276]. In experiments, by decreasing the intensity of the As flux or by increasing the crystallization temperature, a single ring, double rings, and a hole can be fabricated in sequence. For example, the supply of the As flux with an intensity of 1×10^{-5} Torr or 8×10^{-6} Torr leads to the formation of single rings, and the concentric double rings are formed under 2×10^{-6} Torr at 200 °C [273]. Lee et al. [276] reported an interesting phenomenon, with double rings forming under 6.4×10^{-6} Torr and with holed nanostructures appearing when the intensity decreased to 9×10^{-7} Torr at 400 °C.

3.2. Kinetic simulation of QR growth

3.2.1. Kinetic simulation of single-ring, double-ring and hole

Using the GaAs system as an example, the diffusion of atoms includes the diffusion of Ga atoms away from liquid droplets and the trapping of As atoms by Ga crystallizing with As atoms. The evaporation of Ga from the surface is neglected because of the low vapor pressure of Ga [298]. Therefore, the loss of Ga atoms is only caused by crystallization with As atoms. The amounts of crystallization product in different regions, $N_{(i)GaAs}$, and the total amount, N_{GaAs}, per unit time can be written as follows [293]:

$$N_{(i)GaAs} = \begin{cases} \pi r_{Ga}^2 P/\sqrt{2\pi mkT} & (i = \text{A, at boundary of regions I and region II}) \\ \pi P(r_c^2 - r_{Ga}^2)/\sqrt{2\pi mkT} & (i = \text{B, in region II}) \\ 2\pi h_0 D_{Ga} C_0 \ln(r_{Ga}/r_c) & (i = \text{C, at boundary of regions II and region III}) \end{cases}$$

$$N_{GaAs} = N_{(A)GaAs} + N_{(B)GaAs} + N_{(C)GaAs} \tag{3.2}$$

where r_c is the size of the diffusion region of Ga atoms.

Therefore, we can calculate the amounts of GaAs in each region based on Eq. (3.2). The change in the volume of the Ga droplet in a short time, Δt, can be given by the following relation: $V_{droplet}(t + \Delta t) = V_{droplet}(t) - N_{GaAs} V_{mGa} \Delta t / N_A$. The change in the height of the GaAs structure at the point of r (the distance from the center of droplet) in a limit time, Δt, can be given by the following equation:

$$\Delta h(r,t) = \begin{cases} \frac{N_{(A)GaAs} V_{mGaAs} \Delta t}{N_A \pi (r_c^2(t) - r_c^2(t+\Delta t))} & (r_c(t+\Delta t) < r < r_c(t)) \\ \frac{N_{(B)GaAs} V_{mGaAs} \Delta t}{N_A \pi (r_c^2(t) - r_{Ga}^2(t))} & (r_{Ga}(t) < r < r_c(t+\Delta t)) \\ \frac{N_{(C)GaAs} V_{mGaAs} \Delta t}{N_A \pi (r_{Ga}^2(t) - r_{Ga}^2(t+\Delta t))} & (r_{Ga}(t) < r < r_{Ga}(t)) \end{cases} \tag{3.3}$$

The final height of the GaAs structure at the point of r, $h(r)$, can be obtained by the accumulative total of $\Delta h(r)$ in the total time of crystallization process, t_m, i.e.,

$$h(r) = \sum_{t=0}^{t_m} \Delta h(r,t) \tag{3.4}$$

Fig. 35 shows the simulation results, in which the crystallization temperature and the As flux intensity are at 200 °C and 8×10^{-6} Torr for single rings [13]; at 200 °C and 2×10^{-6} Torr for double rings [13]; and at 300 °C and 1×10^{-6} Torr for holed structures, respectively [276]. Fig. 35(a) shows the shape evolution of concentric double rings. However, when the As flux is enhanced to 8×10^{-6} Torr at the same temperature, then the size of the diffusion region of Ga atoms becomes small because of the high trapping ability of As atoms in the case of the high As flux. Thus, the two pinnacles can overlap with the decreasing size of the Ga droplet. This result finally leads to a single ring, as shown in Fig. 35(b). At the temperature 300 °C and at the As flux intensity 1×10^{-6} Torr, for an isolated droplet, the size of the diffusion region of Ga atoms is approximately thirty times the size of the initial Ga droplet due to the increasing diffusivity of Ga atoms at the high temperature. Lee et al. [276] reported that the distances between Ga droplets and the radius of Ga droplets are approximately 300 nm and 50 nm, respectively, which indicate that the size of region II for an isolated droplet is much larger than

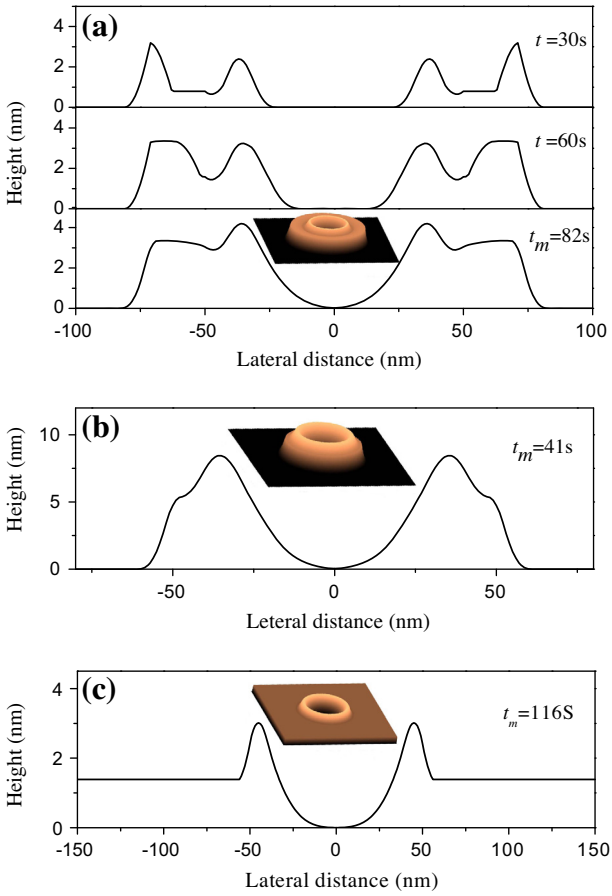

Fig. 35. Simulation results of three different shapes, (a) double rings, (b) single ring, and (c) hole. (a) The evolution process of concentric double rings under temperature 200 °C and As flux intensity 2×10^{-6} Torr. (b) The final shape of GaAs structure, single ring, under temperature 200 °C and As flux intensity 8×10^{-6} Torr. (c) The shape of final GaAs holed structure under temperature 300 °C and As flux intensity 1×10^{-6} Torr [293].

half of the actual distance of droplets. Therefore, crystallization only occurs in two places, the skirt of the Ga droplet and the space between droplets. The high growth rate on the skirt of the droplet results in the formation of a holed structure (Fig. 35(c)).

3.2.2. Kinetic simulation of multiple concentric QRs

The above-mentioned nanostructures with various shapes are fabricated only by a one-step crystallization procedure, i.e., both the intensity of the As flux and the growth temperature are immovable during the crystallization process. If the intensity of the As flux or the growth temperature are altered during the crystallization process, then the final nanostructures may have more complicated shapes. [281,299]. Recently, Somaschini et al. presented the fabrication of GaAs multiple (from three to five) concentric ring nanostructures by a multi-step growth process using droplet epitaxy [281]. The innovative growth method is based on a time-phased As supply to the Ga droplets at different substrate temperatures. In detail, the crystallization process is divided into multiple steps by the change in substrate temperatures.

The above-mentioned kinetic model is also performed to elucidate the formation mechanism of multiple concentric rings. Using concentric triple rings as an example, the crystallization process is

divided into two steps: the first step maintains the same intensity of the As flux and the growth temperature as that for fabricating double rings, and the second step corresponds to increasing the growth temperature to increase the values of r_c/r_{Ga}. During step 1, there are two rapid growth regions. The first region is the skirt of the Ga droplet. The rapid growth in this region results in the formation of an inner ring. The second rapid growth region is the periphery of the diffusion region, which results in the formation of an outer ring. However, when the growth temperature increases during step 2, then the size of the diffusion region becomes large, which induces the rapid growth region at the periphery of the diffusion region to be pushed outward. In this case, the periphery of the new large diffusion region becomes a new rapid growth region. The rapid growth at the periphery of the new diffusion region leads to the formation of the third ring beyond the first double rings formed in step 1. Therefore, after a 2-step crystallization process, we obtain concentric triple rings

Fig. 36 shows the results of simulations based on the kinetic growth model. A double ring surface configuration of the GaAs structure appears after the crystallization procedure of step 1 (4×10^{-6} Torr As supply at 180 °C for 10 s, Fig. 36(a)). When the growth temperature is increased to 210 °C under the same intensity of the As flux after step 1 until the full crystallization of the Ga droplet, then the initial double ring during step 1 becomes a triple ring after step 2 (Fig. 36(b)). If we maintain the growth temperature at 210 °C for only 10 s during step 2, increase the growth temperature to 225 °C for 10 s (step 3), and then maintain the growth temperature at 240 °C until the full crystallization of the Ga droplet (step 4), a fivefold ring structure can be obtained, as shown in Fig. 36(c). The main reasons for multiple ring formation are because the value of r_c/r_{Ga} increases with the increasing temperature, which induces the rapid growth region to be pushed outward.

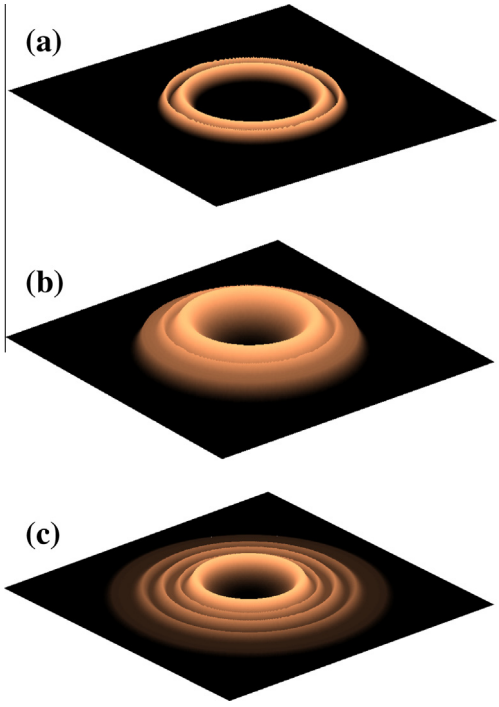

Fig. 36. Simulation results of surface of GaAs nanostructures during multi-step crystallization process. (a) after the procedure of step 1 (4×10^{-6} Torr As supply at 180 °C for 10 s), (b) after step 2 (growth temperature increased to 210 °C under a same intensity of As flux after step 1 until full crystallization of Ga droplet), and (c) after 4-step crystallization procedure (step 1: 180 °C for 10 s; step 2: 210 °C for 10 s; step 3: 225 °C for 10 s; step 4: 240 °C until full crystallization of Ga droplet. All the steps are under a same As supply of 4×10^{-6} Torr) [294].

4. Nucleation and growth thermodynamics of NWs

One-dimensional (1D) nanostructures, such as wires, rods, belts, and tubes, have become the focus of intensive research because of their unique applications. These structures not only provide a good system to study electrical and thermal transport in one-dimensional confinement but are also expected to play an important role in both interconnection and functional units in fabricating electronic, optoelectronic, and magnetic storage devices [300]. Therefore, to attain various nanometer building blocks, many self-assembly and synthesis processes have emerged in recent years [301]. Importantly, these assemblies and syntheses have revealed many unusual thermodynamic and kinetic behaviors of microphase growth [15,17,18,26,27,31,302–306]. A large challenge is how to flexibly control the self-assembly and synthesis processes of 1D nanostructures for the purposes of fundamental studies and for potential applications. To control the growth of nanostructures, it is important to clarify the thermodynamic and kinetic processes of the self-assembly and to develop theoretical tools to address nano fabrications [307,308]. For this issue, we have developed a series of thermodynamic and kinetic tools to pursue the nucleation and growth of 1D nanostructures using the vapor–liquid–solid (VLS) mechanism.

It is well known that VLS growth has been one of leading methods to synthesize semiconductor 1D nanostructures [301]. However, many crucial physical and chemical issues involved in the nucleation and growth of NW have not been addressed in the present securable literature. Some of these crucial issues include the nucleation position of NW on the surface of catalyst particles, the size limit of NW growth, the size-dependence of the NW growth rate and the size-dependent shape evolution during NW growth. Importantly, these basic physical and chemical processes play key roles in controlling the fabrication of 1D nanostructures. In this section, we introduce many new theoretical tools to address the nucleation and growth of NW by VLS.

4.1. Thermodynamic and kinetic theory of NW nucleation

Based on the experimental data, there are two general modes of NW growth by VLS. One mode has catalyst nanoparticles on the bottom of NWs, and the other mode has catalyst nanoparticles on the tip of NWs [300,309–315]. Why would catalyst nanoparticles be on the tip of NWs sometimes and on the bottom at other times? Few studies have reported the above-mentioned issue [31,297,300]. We proposed the two universal thermodynamic and kinetic theoretical criteria for the selection growth of NWs by VLS [17], which show that the thermodynamic theory is valid when used to address growth [17,26,302].

4.1.1. Thermodynamic criteria of selection nucleation

Generally, Gibbs free energy is an adaptable measure of the stability of a state in phase transition. Thermodynamically, the phase transformation is caused by the difference in the free energy [186,316]. Therefore, we propose a thermodynamic criterion for the selection growth of NWs by comparing the Gibbs free energy difference of the NW nucleation in two cases [186,317]. For the first case, i.e., the NW nucleation occurs on the surface of catalyst nanoparticles, as shown in Fig. 37(a). When an atom cluster condensed with a catalyst on the substrate, Gibbs free energy can be expressed as follows:

$$\Delta G_S = 2\sigma_{nv}\pi r_1^2(1-\cos\theta_1) - \pi r_1^2 \sin^2\theta_1 \sigma_{nv}\cos\theta_1 + \frac{4\pi r_1^3 \Delta g_v}{3}\frac{2-3\cos\theta_1+\cos\theta_1^3}{4} \tag{4.1}$$

Based on the condition of the critical nucleus formation, $\partial\Delta G_S/\partial r_1 = 0$, when the atomic cluster transforms into the critical nucleus, then the radius of the critical nucleus can be calculated as follows:

$$r_1^* = -\frac{8}{3}\frac{\sigma_{nv}}{\Delta g_v^0} \tag{4.2}$$

Accordingly, the formation energy $\Delta G_S^*(r_1^*)$ of the critical nucleus is calculated as follows:

$$\Delta G_s^* = \left(\frac{256\pi\sigma_{nv}^3}{9(\Delta g_v^0)^2} + \frac{2048\pi\sigma_{nv}^3}{81(\Delta g_v^0)^3}\right)\left(\frac{2-3\cos\theta_1+\cos^3\theta_1}{4}\right) \tag{4.3}$$

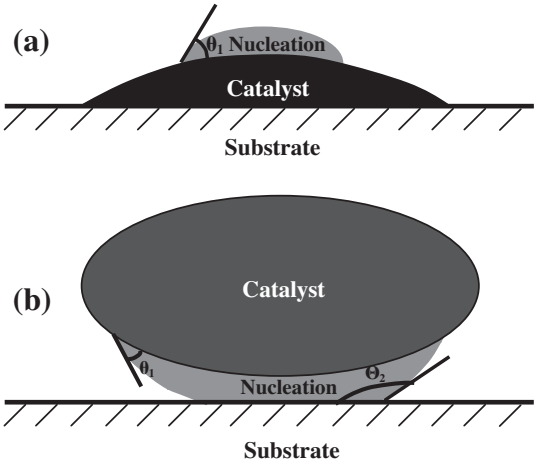

Fig. 37. The schematic illustration of the NW nucleation by two models upon CCVD: nucleation on the surface of catalyst nanoparticles (a) and at the interface between catalyst nanoparticles and substrate (b) [31].

For the second case, i.e., the NW nucleation occurs on the interface between the catalyst nanoparticle and the substrate (Fig. 37(b)), the entire Gibbs free energy difference can be obtained by the following equation [31]:

$$\Delta G_T = \frac{4\pi r_2^3 \Delta g_v}{3} f_2(\theta) - \pi r_2^2 \sigma_{nv} f_1(\theta) \tag{4.4}$$

where $f_1(\theta)$ and $f_2(\theta)$ are geometrical coefficients. Similarly, based on the condition of the critical nucleus formation, $\partial \Delta G_T / \partial r_2 = 0$, when the atomic cluster transforms into the critical nucleus, then the radius of the critical nucleus and the formation energy $\Delta G_T^*(r_2^*)$ can be calculated as follows:

$$r_2^* = \frac{\sigma_{nv}}{2\Delta g_v^0}\left(\frac{2f_1(\theta)}{f_2(\theta)} + \frac{8}{3}\right) \tag{4.5}$$

$$\Delta G_T^* = -\pi\sigma_{nv}\left[\frac{\sigma_{nv}}{2\Delta g_v^0}\left(\frac{2f_1(\theta)}{f_2(\theta)} + \frac{8}{3}\right)\right]^2 f_1(\theta) + \frac{4\pi}{3}\left[\frac{\sigma_{nv}}{2\Delta g_v^0}\left(\frac{2f_1(\theta)}{f_2(\theta)} + \frac{8}{3}\right)\right]^3 \times \left(\frac{1}{2}\Delta g_v^0 - \frac{2\Delta g_v^0}{\frac{2f_1(\theta)}{f_2(\theta)} + \frac{8}{3}}\right) f_2(\theta) \tag{4.6}$$

Thus, we can determine that the NW nucleation on the surface of catalyst nanoparticles (Fig. 37(a)) would be preferable when $\Delta G_S^* > \Delta G_T^*$. In contrast, the nucleation on the interface between catalyst nanoparticles and substrates (Fig. 37(b)) would be preferable when $\Delta G_S^* < \Delta G_T^*$. For the case of the Si NW nucleation on a Si substrate using Fe as catalyst, we can attain the relation curves between θ_2 and the critical radius of the two cases, as shown in Fig. 38(a). Obviously, one can determine that the critical radius r_2^* increases quickly with θ_2 decreasing when θ_2 is less than 80° and that the critical radius is close to r_1^* when θ_2 is larger than 150°. In addition, we can obtain the dependence of θ_2 and the critical energy, as shown in Fig. 38(b). However, comparing Fig. 38(a) with (b), we find that the dependencies of the critical radius and of the critical energy of nuclei on the value of θ_2 are inversely related. More importantly, most of the experimental cases of Si NWs growing on Si substrates using Fe as catalysts by VLS show that Fe nanoparticles are always on the tip of Si NWs. [10,311,318,319].

4.1.2. Kinetic criteria of selection nucleation

From Louchev's model [320], we introduce the diffusion kinetic mechanism of the nucleation and growth of NWs by VLS. Two types of diffusion processes, surface diffusion and body diffusion, of depositing atoms on the surface of nanoparticles are important for the selection nucleation stage,

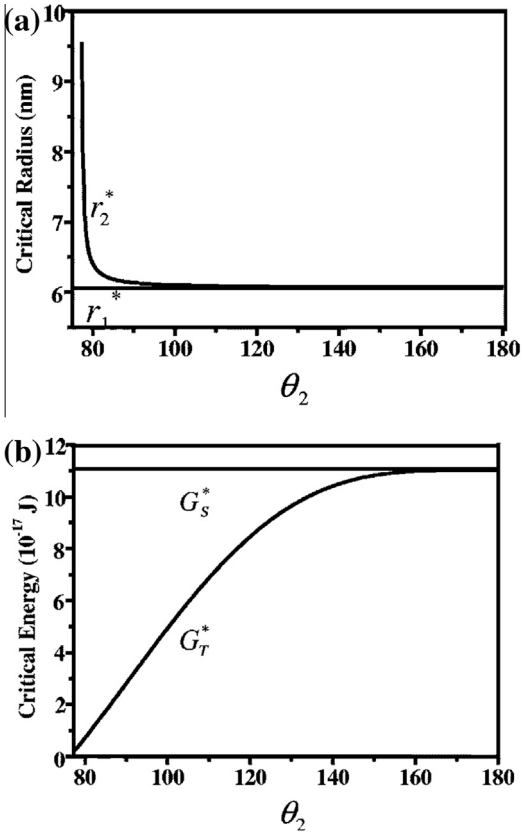

Fig. 38. (a) The dependence relationship between the contact angle θ_2 and the critical nucleus r_1^*, r_2^*. (b) The relationship curves between the contact angle θ_2 and the critical energy ΔG_S^*, ΔG_T^* [31].

defining whether the nanoparticle remains at the substrate or on the tip of the growing *X* NWs. For the nucleation of NWs by VLS, the surface diffusion of adatoms on the surface of nanoparticles is expressed by the surface saturation time of t_s, indicating the time it takes for the increasing adatom content to reach the saturation concentration. Thus, the surface diffusion time of order is expressed by the following equation [320]:

$$t_s = \frac{C^{*2} D_b(r,T)}{Q^2} \tag{4.7}$$

where C^* is a concentration threshold triggering the precipitation of the growing atoms directly onto the upper surface of the nanoparticle. $D_b(r, T)$ is the size-dependent body diffusion coefficient of atoms.

In contrast, the body diffusion is expressed by the body diffusion time of t_d, which can be calculated as follows:

$$t_d = \frac{1}{6D_b(r,T)} \sqrt[3]{\left[\frac{4\pi}{3}\left(\frac{d}{2}\right)^3\right]^2} \tag{4.8}$$

Clearly, when $t_d \gg t_s$, the nanoparticle surface saturates with atoms much faster than when one penetrates to its base, suggesting that the nucleation of adatoms would occur on the upper surface of catalyst nanoparticles and then provide a nanoscale template for the NW growth. In contrast, when $t_d \ll t_s$, then atoms would penetrate to the base from the upper surface of nanoparticles much faster

than adatoms reach the saturation threshold on the upper surface, implying that growing atoms will precipitate at the bottom of nanoparticles and then result in nucleation at the interface between the nanoparticle and the substrate.

To study the kinetics of Si NW growth, the diffusion time and saturation time are calculated at the given temperature and pressure in the Si–Fe system, as shown in Fig. 39. We find that the diffusion time increases with the size increase of Fe catalyst, whereas the saturation time hardly changes with the increasing diameter of the nanoparticles. Importantly, $t_d < t_s$ (more two orders of magnitude) when the size of the Fe catalyst is less than 25 μm. According to the above-mentioned kinetic criterion, this result indicates that Si penetrates to the base much faster than Si when the catalyst surface reaches the saturation threshold when the size of the nanoparticles is less than 25 μm. Thus, Si will precipitate at the bottom, lift catalysts, and later maintain catalyst droplets on NW tips when the size of the Fe catalyst is less than 25 μm.

Tan et al. noted that the size of the Si NWs is limited by the size of the metallic catalyst droplet and that the diameter of the Si NWs is usually much smaller than that of the catalyst droplet [321]. Accordingly, the size of Si NWs should be smaller than that of the catalyst droplet when catalyst droplets are on NW tips. Interestingly, currently, almost all experimental data at given temperatures and pressures in the Si–Fe system show that the diameter of Si NWs is less than 200 nm and that catalyst droplets are definitely located on the tip of the Si NWs [10,311,318,319], which correspond with the above-mentioned theory predictions. In contrast, from Fig. 39, one can see that a critical diameter of 30 μm exists for catalyst droplets and that the catalyst surface-saturation and Si penetration-base time are nearly the same order of magnitude when the size of the nanoparticle is larger than 30 μm. Therefore, when the radius of the droplet is larger than 30 μm, then no solid conclusions can be drawn from the above model predictions, and maybe, the selection growth of NWs would be determined by chance.

Thermodynamic and kinetic criteria of the selection growth of NWs forming by VLS seem to operate to determine catalyst nanoparticles on the tip or bottom of NWs. Notably, in some studies of Si NW synthesis by laser ablation [322,323], no catalyst nanoparticles were observed anywhere on the NW tip or on the substrate, even when metals were mixed in the target. Actually, this nucleation and growth of NWs are different from the VLS mechanism. Moreover, Wang et al. [323] noted that metal was not necessary for Si NW synthesis by laser ablation. Instead, oxides such as SiO_2 are effective catalysts that largely enhanced the Si NW growth in these cases [322,323].

4.2. Thermodynamic and kinetic models of NW growth

Thus far, most semiconductor NWs have been synthesized based on the VLS process [311,324–329]. The VLS mechanism reveals that (i) reactants are supplied in the vapor phase and that NWs

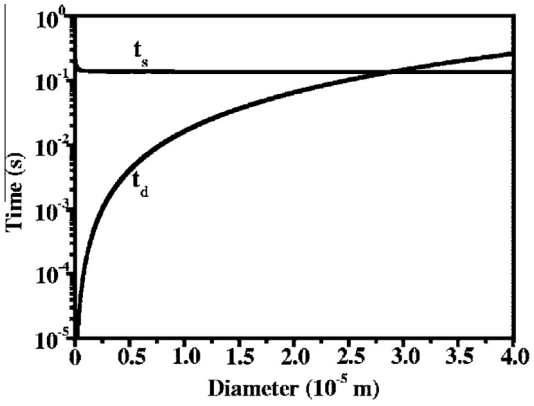

Fig. 39. The comparison between the surface saturation time of t_s and the body diffusion time of t_d [31].

are formed by the extraction of NWs materials from liquid droplets of metal alloy and that (ii) the NW growth results from the difference in the sticking coefficients of liquid droplets and NWs, i.e., sticking coefficients of NWs are orders of magnitude smaller than that of liquid droplets. As a result, the droplet and the solid NW can capture and reject nearly all of the constituents of the growing material from the vapor phase, respectively. Generally, the intrinsic properties of 1D nanostructures are primarily determined by their size, shape, composition, and crystalline structure. In principle, one can control any one of these characteristics to fine-tune the properties of this nanostructure. Therefore, it is essential to pursue the basic physics and chemistry involved in the formation of NWs. However, the size limit of the NW growth by VLS still remains much less understood in theory, although there have been many relevant experimental studies of NW growth [319,329,330]. For instance, in both theories and experiments, we have not yet determined how thin or thick NWs could be synthesized using VLS. Accordingly, we proposed the universal nucleation thermodynamics and growth kinetics for the NW growth by VLS, and then theoretically deduced the size limit of the NW growth. Importantly, using the Si NW (SiNW) growth as an example, we found that the theoretical predictions are in excellent agreement with experimental cases.

4.2.1. Thermodynamic size limit of NW growth

In general, the minimal size of the NWs depends on nucleation thermodynamics and on growth kinetics (energy stability theory). However, this minimal size also depends on the Rayleigh instability of NW itself (linearized stability theory) [331]. However, when the linearized system is symmetric, then the prediction of the stability based on the linearized stability theory and on the energy stability theory is consistent [332,333]. Linearized equations do not yield much information concerning the energy stability range. Thus, we could have an instability (usually called a subcritical instability)

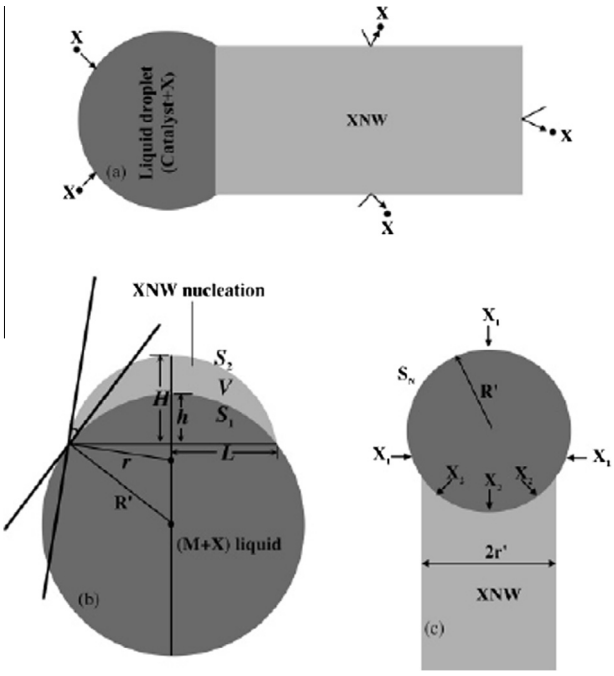

Fig. 40. The schematic diagram showing the VLS mechanism, and XNW thermodynamic nucleation and kinetic growth processes. (a) The droplet and the solid NW capturing and rejecting nearly all the constituents of the growing material from the vapor phase, respectively, due to the sticking coefficient immense difference between them. (b) The thermodynamic nucleation case. (c) The kinetic growth case [297].

below the critical values of Rayleigh numbers determined by the linearized theory, which could be in the energy stable region. Thermodynamically, the phase transformation is caused by the difference in Gibbs free energies. The schematic illustration of the X NW (XNW) nucleation by VLS is shown in Fig. 40. The Gibbs free energy difference of a cluster X can be expressed as follows [186,321]:

$$\begin{aligned}\Delta G = {} & \pi R(\sigma_{xv} - \sigma_{lv})\left(R - \sqrt{R^2 - r^2 + \frac{r^2(R\cos\theta - r)^2}{R^2 + r^2 - 2Rr\cos\theta}}\right) + 2\pi\sigma_{xv}r^2\left(1 - \frac{R\cos\theta - r}{\sqrt{R^2 + r^2 - 2Rr\cos\theta}}\right) \\ & + \frac{1}{6}\pi\left(\frac{RT}{V_m}\ln\left(\frac{C}{C^{eq}}\right)\right)\left(\left(R - \sqrt{R^2 - r^2 + \frac{r^2(R\cos\theta - r)^2}{R^2 + r^2 - 2Rr\cos\theta}}\right)^3\right. \\ & + 3r^2\left(R - \sqrt{R^2 - r^2 + \frac{r^2(R\cos\theta - r)^2}{R^2 + r^2 - 2Rr\cos\theta}}\right)\left(1 - \frac{(R\cos\theta - r)^2}{R^2 + r^2 - 2Rr\cos\theta}\right) \\ & \left. - r^3\left(1 - \frac{R\cos\theta - r}{\sqrt{R^2 + r^2 - 2Rr\cos\theta}}\right)^3 - 3r^3\left(1 - \frac{R\cos\theta - r}{\sqrt{R^2 + r^2 - 2Rr\cos\theta}}\right) \times \left(1 - \frac{(R\cos\theta - r)^2}{R^2 + r^2 - 2Rr\cos\theta}\right)\right)\end{aligned} \tag{4.9}$$

When $\frac{\partial \Delta G(r)}{\partial r} = 0$, the critical size of the nuclei of XNWs can be attained [17]. Clearly, the critical size of the XNW nuclei is the thermodynamic size limit of the NW growth.

Fig. 41 shows the dependence of the radius of a cluster of Si (r) and the Gibbs free energy (ΔG). We find that the Gibbs free energy of Si clusters (ΔG) hardly changes with an increase in the Au-catalyst radius. Therefore, the nucleation barrier of NWs does not actually depend on the size of the metal catalyst. The radius of Si clusters (r) corresponding to the peak value should be the critical radius (r') of the SiNW nucleation. Furthermore, the relation curves between the Au-catalyst radius (R') and the critical radius of the SiNW nucleation (r') are given by numerical calculation, as shown in Fig. 42. Clearly, the critical radius of the SiNW nucleation essentially remains unchanged with an increase in the Au-catalyst radius. These results suggest that the critical radius of the NW nucleation seems a relatively independent value for a given system, e.g., the Si-Au system. There is certainly a thermodynamic limit, i.e., a theoretical minimum value, for the NW growth size by VLS. For example, the thermodynamic limit is a 1.4 nm radius for the Si–Au system, as shown in Fig. 42. Interestingly, thus far, we have not yet found any experiments that reported SiNWs with less than a 1.4 nm radius that have been synthesized by VLS.

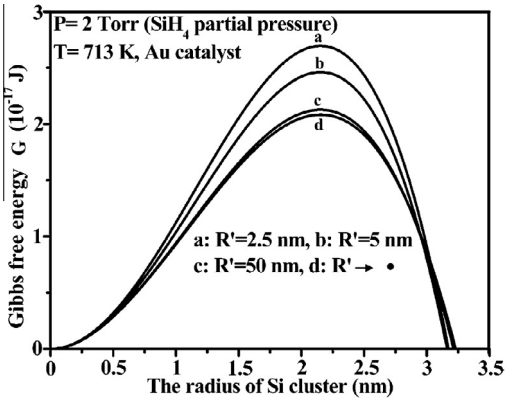

Fig. 41. Dependence of the radius of the SiNW nucleation and the Gibbis free energy on the Si cluster size under conditions of various Au-catalyst sizes, temperature (713 K), and pressure (SiH_4 partial pressure of 2 Torr) [297].

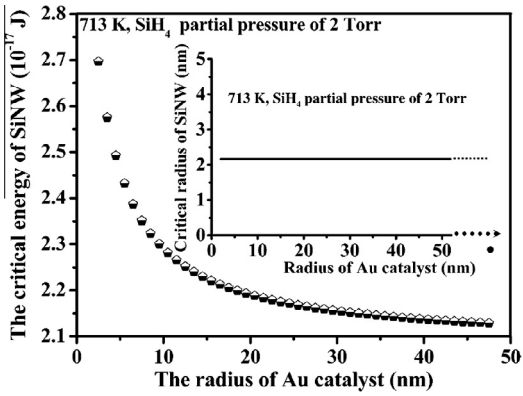

Fig. 42. Relationship curve between the Au-catalyst radius and the critical energy of SiNW nucleation; the inset shows the dependence of the Au-catalyst radius and the critical nucleation of SiNW nucleation [297].

4.2.2. Kinetic size limit of NW growth

From the growth kinetics, when X atoms reach saturation in the liquid droplet, then the number of X atoms of the droplet capturing (X_1) and extracting ($X_2 + X_2^N$) should be equal, as shown in Fig. 40(c). Thus, only X_2^N atoms contribute to the growth of XNWs in the extracting X atoms. The number of X_2^N atoms can be approximately equal to the net flux of impinging on the surface of the area whose value is equal to S_N. Reasonably, the number N of X_2^N atoms is expressed as follows:

$$N = 2\pi R'\left(R' - \sqrt{R'^2 - r'^2}\right)(\theta - \theta_r) = \frac{10^6 \pi r'^2 S \rho N_m}{M} \tag{4.10}$$

where R', r', ρ, N_m, and M are the radius of droplet; the radius of XNW; the density of single crystal X; the Avogadro constant; and the mole mass of single crystal X, respectively. θ is the number of X atoms from vapor impinging on a unit plane surface in an unit time. S is the growth velocity of XNW, and can be expressed as follows [334]:

$$S = h\nu \exp(-E_\alpha/RT)[1 - \exp(-|\Delta g_m|/RT)] \tag{4.11}$$

where h, ν, E_α, R, and T are the lattice constant of the XNW in the growth direction; the thermal vibration frequency; the mole adsorption energy of adatoms attached of X atom at surface sites; the gas constant; and the substrate temperature, respectively. The Gibbs free energy difference per mole, Δg_m, has the following relation: $\Delta g_m = -RT\ln(C/C^{eq})$.

According to Eqs. (4.10) and (4.11), we can obtain the relation between the size ($2R'$) of the catalyst and the diameter ($2r'$) of XNW as follows:

$$2r' = 4R'\left(\frac{M\left(P - \frac{PC^{eq}}{C}\exp\left(\frac{2\sigma_{lv}\Omega}{R'kT}\right)\right)}{10^6\sqrt{2\pi mkT}\rho N_m h\nu \exp\left(-\frac{E_\alpha}{RT}\right)\left(1 - \exp\left(-\frac{|-RT\ln\left(\frac{C}{C^{eq}}\right)|}{RT}\right)\right)} - \left(\frac{M\left(P - \frac{PC^{eq}}{C}\exp\left(\frac{2\sigma_{lv}\Omega}{R'kT}\right)\right)}{10^6\sqrt{2\pi mkT}\rho N_m h\nu \exp\left(-\frac{E_\alpha}{RT}\right)\left(1 - \exp\left(-\frac{|-RT\ln\left(\frac{C}{C^{eq}}\right)|}{RT}\right)\right)}\right)^2\right)^{1/2} \tag{4.12}$$

The dependence of the diameter of SiNWs on the Au-catalyst size can be attained from Eq. (4.12), as shown in Fig. 43. One can see that the diameter of SiNWs increases with an increase in the Au-catalyst diameter and that the SiNW diameter is always smaller than that of the Au-catalyst. These theoretical results are consistent with experimental cases [311,319,335,336]. Remarkably, the quantitative calculations are in excellent agreement with Lieber's experimental data [319,336], as shown in

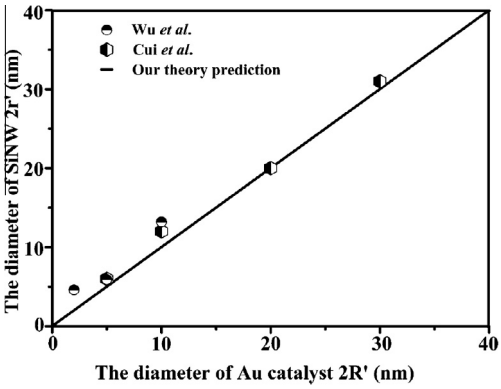

Fig. 43. Experimental data of relationship between the size of the Au catalyst and the diameter of SiNW compared to the calculated curve by using Eq. (10) and Au–Si phase diagram [297].

Fig. 43. Similarly, Yu et al. [337] simulated the relation curve between the diameter of catalyst and the size of GaAs NWs from their empirically linear expression and from experimental data. Interestingly, our theoretical predictions are consistent with Buhro's results. Noticeably, in Fig. 43, considering the oxidation effect after the SiNW growth, the data of Ref. [319] have been corrected from the authors' stated thickness of the oxidation layer. Accordingly, the size of the catalyst droplet can limit the possible growing size of the NW synthesized by VLS to a certain extent from the kinetic viewpoint.

4.3. Size-dependent shape evolution of NW

As is well known, self-assembly processes require the interactions of atoms or clusters of atoms as the thermodynamic driving force to organize those atoms or clusters to form nano domain morphologies [307]. For instance, Thürmer et al. recently reported the self-assembly of the regular arrays of two-dimensional (2D) vacancy islands via absorbate-driven dislocation reactions [338]. Therefore, it is essential to pursue the physical and chemical origins causing the nanostructure to control its growth. In contrast, the surface shape of 1D nanostructures plays a particular important role in their application. For instance, NWs as wraparound gate transistors or as core–shell heterostructures require good control of the surface shape to achieve a uniform cross section and to minimize carrier scattering at rough interfaces [339]. Accordingly, a quantitative understanding of the surface shape formation of 1D nanostructures is required for the application of interest.

For example, experiments have shown the size-dependent morphological evolution of the 1D SnO_2 nanostructure growth using metal catalyst-assisted thermal chemical vapor transport and condensation (the VLS process). In detail, the shape formations of NWs and nanobelts of SnO_2 are size dependent, i.e., the wire is favorable when the size is less than 90 nm, and the belt is favorable when the size is more than 90 nm (Fig. 44). For this issue, we proposed nucleation thermodynamics, growth kinetics, and shape transition thermodynamics to elucidate our findings [15,27,28,30,31,302]. Note that the size-dependent shape transformation from the initial stage of the NW nuclei to the nanobelt nuclei originates from the thermodynamic driving forces of the nucleation and growth of 1D nanostructures.

4.3.1. Nucleation thermodynamic considerations

Generally, Gibbs free energy is an adaptable measure of the energy of a state in phase transformation among competing phases [186]. Therefore, we perform the nucleation of SnO_2 based on thermodynamic nucleation at the nanometer scale [31,297]. Considering that the NW growth originates from the column-shape nuclei and that the formation of nuclei of the NW (Fig. 44(b)) is a process of the reaction precursors extracted from the saturated Au catalyst [334], the Gibbs free energy difference of a column-shape nucleus is expressed as follows:

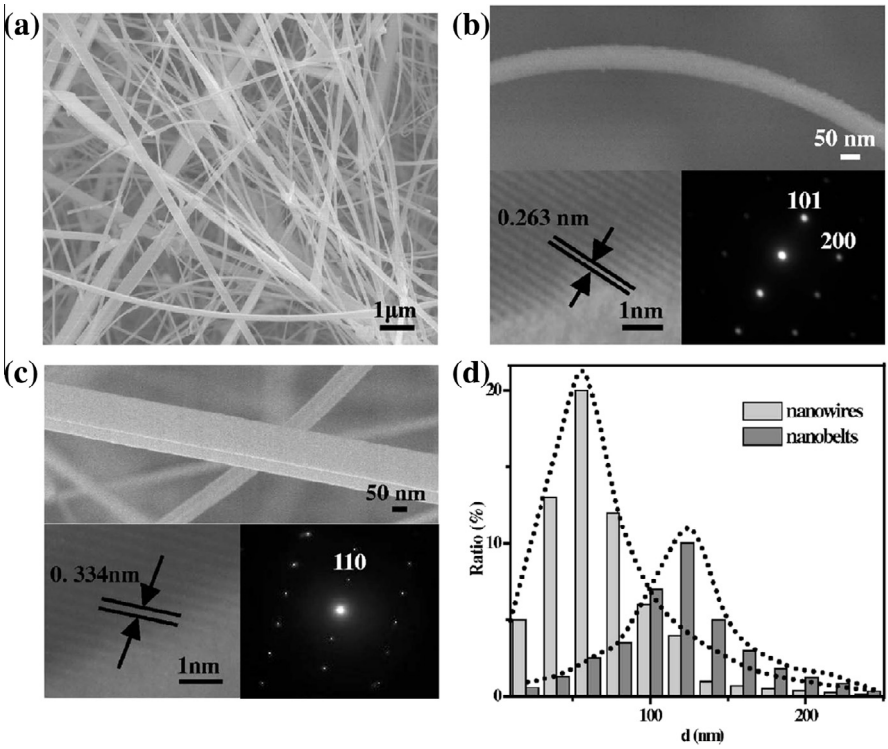

Fig. 44. (a) Low-magnifying field emission scanning electron microscopy (FESEM) image of SnO_2 NWs and nanobelts. (b) High-magnifying FESEM image of a NW, in which a corresponding high-resolution transmission electron microscopy (HRTEM) image and selected area electronic diffraction (SAD) are shown below left right, respectively. (c) High-magnifying FESEM image of a nanobelt, in which a corresponding HRTEM image and SAD are shown below left right, respectively. (d) The SEM statistics result of the radial size distribution of NWs and nanobelts in the total prepared 1D nanostructures [28].

$$\Delta G_1 = -\Delta g_v \pi r_1^2 L_1 + \pi r_1^2(\delta_1 + \delta_1'') + 2\pi r_1 L_1 \delta_1 \tag{4.13}$$

where δ_1 and δ_1'' are the nucleus-vapor and the nucleus-liquid interface energies, respectively, and r_1 and L_1 are the radius and the height of the nucleus, respectively. The $\Delta g_v = -RT/V_m \ln(P/P_e)$ is the Gibbs free energy difference per unit volume. From Eq. (4.13), we deduce that the critical radius of r_1^*, the critical height of L_1^* and the critical energy of ΔG_1^* of nuclei are $2\delta_1/\Delta g_v$, $2(\delta_1 + \delta_1'')/\Delta g_v$, and $4\pi\delta_1^2(\delta_1 + \delta_1'')/\Delta g_v^2$, respectively.

We use square nuclei instead of rectangle nuclei for simplifying the calculation in our case. Thus, the Gibbs free energy difference of a rectangle nucleus is expressed as follows:

$$\Delta G_2 = -\Delta g_v r_2^2 L_2 + r_2^2(\delta_2 + \delta_2'') + 4 r_2 L_2 \delta_2 \tag{4.14}$$

where δ_2 and δ_2'' are the nucleus-vapor and nucleus-liquid interface energies, respectively, and r_2 and L_2 are the side-length and the height of nucleus, respectively. Similarly, the critical radius of r_2^*, the critical height of L_2^* and the critical energy of ΔG_2^* of nuclei are $4\delta_2/\Delta g_v$, $2(\delta_2 + \delta_2'')/\Delta g_v$, and $16\pi\delta_2^2(\delta_2 + \delta_2'')/\Delta g_v^2$, respectively.

The size-dependence of the NW and of nanobelt nucleation is shown by Fig. 45. Clearly, the radial size of the critical nucleus of nanobelts is approximately two times larger than the diameter of the critical nucleus of NWs. Moreover, the nucleation energy of NW nuclei is lower than that of nanobelt nuclei, which indicates that the nucleation probabilities of NWs are higher than that of nanobelts. The

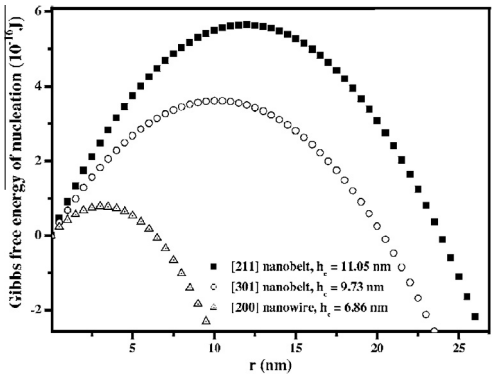

Fig. 45. The nucleation energies of a column-shape nucleus of NWs and a rectangle-shape nucleus of nanobelts growing along the (211) and the (301) directions, respectively [28].

results are consistent with our observations that the ratios of wires and belts in the total synthesized nanostructures are 63% and 37%, respectively.

4.3.2. Growth kinetic considerations

Once the nucleation occurs, the continuous supply of the reaction precursors extracted from the saturated Au catalyst results in increases in the sizes and heights of NWs and nanobelts [27,297]. Fig. 46(a) shows the growth mechanisms of the NW or the nanobelt. As is well known, the surface free energy of nuclei and the concentration of the reaction precursors play key roles in the growth of nuclei [29], in which the surface free energy consists of the surface energy [340,341] and the strain energy [342,343]. Meanwhile, the supply of the reaction precursors originates from the axial direction reaction precursors extracted from the saturated Au catalyst. The supply leads to the growth of the radius and height of 1D nanostructures, i.e., (i) the axial supply results in an augment in the height (P_{aa}), and (ii) the axial supply results in an augment in the radius (P_{ar}) as follows [343]:

$$P_{ij} = \frac{\exp\left(-\frac{\Delta E_{ij}}{KT}\right)}{\sum_{i,j}\exp\left(-\frac{\Delta E_{ij}}{KT}\right)}, \Delta E_{ij} = \Delta E_{Sij} + \Delta E_{Tij}, i,j = a,r \tag{4.15}$$

K is the Boltzmann constant, and T is the growth temperature. Considering the free energy ΔE_{ij} gained in each case, we assume that the radial size of NWs and nanobelts is large enough to make the surface energy ΔE_{Sij} much smaller than the strain energy ΔE_{Tij}. Thus, in each case, ΔE_{Tij} is written as follows [90]: $\Delta E_{Taa} = E_m(1-\sigma_m)\varepsilon_a^2, \Delta E_{Tar} = E_m\delta_m\varepsilon_a^2$, where E_m is the elastic modulus; δ_m is the Poisson's ratio of NWs or nanobelts; and ε_a is the strain in the axial. Therefore, δt, the volume additivities of NWs along the radial and axial are shown as follows [343]:

$$\begin{aligned}
&\frac{1}{4}L_1(t)d_1(t)\frac{\partial d_1(t)}{\partial t} = A\frac{1}{4}P_{ar}d_1(t)^2 \\
&\frac{1}{4}d_1(t)^2\frac{\partial L_1(t)}{\partial t} = 2A\frac{1}{4}P_{aa}d_1(t)^2
\end{aligned} \tag{4.16}$$

Similarly, in the case of nanobelts, we have the following relations:

$$\begin{aligned}
&\frac{1}{4}L_2(t)d_2(t)\frac{\partial d_2(t)}{\partial t} = A\frac{1}{4}P_{ar}d_2(t)^2 \\
&\frac{1}{4}d_2(t)^2\frac{\partial L_2(t)}{\partial t} = 2A\frac{1}{4}P_{aa}d_2(t)^2
\end{aligned} \tag{4.17}$$

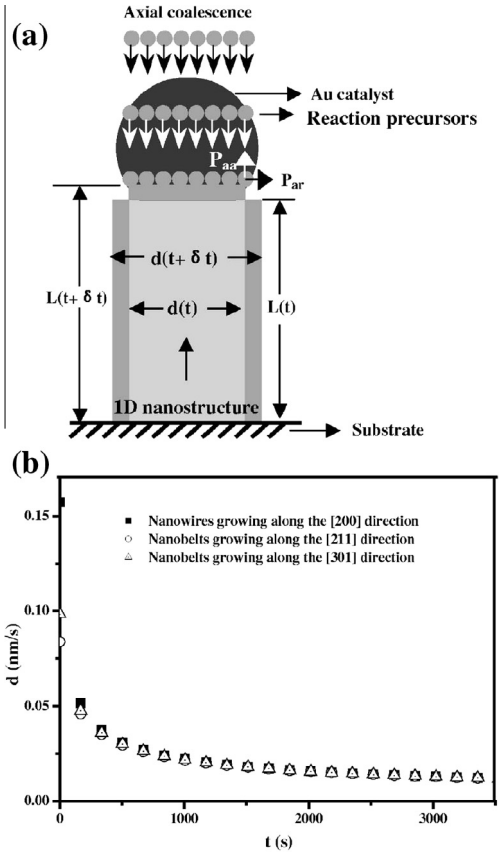

Fig. 46. (a) The growth mechanism sketch map of the 1D nanostructure (the radial cross section of the NW or nanobelt is shown). (b) The growth rates of NW and nanobelt [28].

where $d_1(t)$ and $d_2(t)$ are the diameter (which is the function of the time t) of NWs and the side-length (which is the function of the time t) of nanobelts, respectively; $L_1(t)$ and $L_2(t)$ are the height (which is the function of the time t) of the NWs and the nanobelts, respectively; and A is the constant that is relative with the growth. Neglecting the difference in strain energies in every type of growth, we attain approximate conclusions as follows:

$$d_1(t) \approx [2(t + 2r_1^{*2})]^{\frac{1}{2}}, \quad d_2(t) \approx \left[2\left(t + \frac{r_2^{*2}}{2}\right)\right]^{\frac{1}{2}} \tag{4.18}$$

where t is the growth time of nanostructures after nucleating, and r_1^* and r_2^* are critical sizes of NWs and nanobelts, respectively. According to Eq. (4.18), the growth rates of NWs and nanobelts are shown by Fig. 46(b). Clearly, both growth rates of NWs and nanobelts are identical during the growth of nanostructures. Therefore, the final size of nanobelts is approximately two times larger than that of NWs because r_2^* is double the value of r_1^*. This theoretical result is in good agreement with our findings shown in Fig. 44(d).

4.3.3. Shape transition thermodynamic consideration

During the initial stage of the growth of NW nuclei, there are two probabilities of the shape transitions. One is from the wire nuclei to belt nuclei, and another one is from the belt nuclei to wire

nuclei. In order to clarify which shape transition is preferable in thermodynamic, we need to compare the Gibbs free energies of wire and belt nuclei. The Gibbs free energy difference between wire nuclei and belt nuclei, is given as $\Delta G = V\Delta P + \delta\Delta S$ [344], where ΔP is a pressure difference between NW nuclei and nanobelt nuclei, which is small enough to ignore. $V = \pi d_1^2 L_1/4 = d_2^2 L_2$ is the volume of NW nuclei and nanobelt nuclei, in which d_1 and L_1 are the diameter and height of NW nuclei, and d_2 and L_2 are the side length and height of the nanobelt nuclei, and $L_2 = \pi d_1^2 L_1/4d_2^2$. δ is the surface energy difference of the (2 0 0) plane of NW nuclei and the (2 1 1) plane of nanobelt nuclei. ΔS is the surface area difference between NWs nuclei and nanobelt nuclei. Thus, ΔG can be expressed as

$$\Delta G = \delta_2(4d_2L_2 + d_2^2) + \delta_2'' d_2^2 - \delta_1(\pi d_1 L_1 + \pi d_1^2/4) - \pi d_1^2 \delta_1''/4 \tag{4.19}$$

According to the equation, when d_1 is equal to 150, 175 and 200 nm and L_1 = 12 nm, the relationships between ΔG and d_2 are shown in Fig. 47(a). Clearly, three curves intersect at the A point ($\Delta G = 0$ and d_2 = 43 nm), and $\Delta G < 0$ in these regions of AB, AC and AD. In detail, in these regions, $\Delta G < 0$ means the Gibbs free energy of NW nuclei is larger than that of nanobelt nuclei, suggesting that the shape transition from wire nuclei to belt nuclei is probable. In this instance, the NW nuclei with diameters of 150, 175 and 200 nm could transform into the nanobelt nuclei with radial sizes of 60, 70, and 80 nm, respectively. Note that, $\Delta G > 0$, when $d_1 < 120$ nm, implying that the shape transition from wire nuclei to belt nuclei of NW nuclei with the diameter less than 120 nm is not thermodynamically expected.

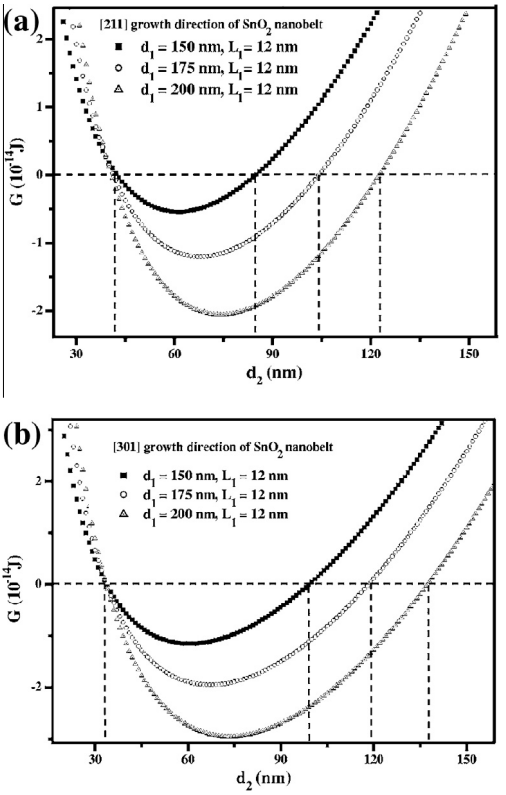

Fig. 47. Dependence of the Gibbs free energy of the shape transition during the initial stage of the nuclei growth. (a) The shape transition from the wire nuclei to the belt nuclei that grows along the (2 1 1) direction on the radial size of the NWs nuclei under conditions of d_1 = 150, 175, and 200 nm, respectively, and L_1 = 12 nm. (b) The shape transition from the wire nuclei to the belt nuclei that growing along the (3 0 1) direction on the radial size of a NWs nuclei under conditions of d_1 = 150, 175, and 200 nm, respectively, and L_1 = 12 nm [28].

When the nanobelts grow along the [301] direction, according to the Eq. (4.19), the relationships between ΔG and d_2 are shown in Fig. 47(b). Clearly, three curves intersect at the E point ($\Delta G = 0$ and $d_2 = 34$ nm), and $\Delta G < 0$ in these regions of EF, EG and EH. The NW nuclei with diameters of 150, 175 and 200 nm could transform into the nanobelt nuclei with radial sizes of 60, 70, and 80 nm, respectively. Note that, $\Delta G > 0$, when $d_1 < 90$ nm, implying that the shape transition from the wire nuclei to the belt nuclei of NW nuclei with the diameter less than 90 nm is not thermodynamically expected. To sum up, the difference between the calculation results is not so large that the conclusions are consistent and acceptable. Therefore, the larger NW nuclei sizes are, the easier the shape transition from wire nuclei to belt nuclei is. In fact, these theoretical predictions are not only consistent with experiments shown in Fig. 44(d), but also are physical origins of the experimental observations that both the wire formation with small size and the belt formation with large size are favorable during the growth of nanostructures.

4.4. Thermodynamic treatment of core–shell NW heterostructure growth

Semiconductor NW heterostructures have attracted considerable interest due to their great potential in microelectronic and optoelectronic devices [345–349]. As the promising and typical semiconductor heterostructure, the radial Ge/Si NW heterostructure, i.e., the Ge-core/Si-shell NW structure, has been widely investigated and used in various nanodevices, such as solar cells [350,351], lasers [352], and sensors [353]. More importantly, semiconducting core–shell NW structures show better performance than that of single-elements, such as Ge or Si NWs [354,355]. In contrast, surface roughening is usually undesirable for the epitaxial growth of high quality radial NW heterostructures. For example, the surface of the Ge-core/Si-shell NWs always exhibits a periodic modulation with island-like morphologies during epitaxial growth [349,355–358]. However, considering the surface roughness of a NW as QDs, the core–shell NW structure with roughening has actually transferred into another type of heterostructure, i.e., the QD-NW heterostructure, which can be considered a unique functional nanostructure for applications ranging from solar cells to biosensors [359]. Therefore, the physical understanding of the roughening behavior during epitaxial growth on the surface of NW is essential for theoretical design and for the experimental growth of high quality radials.

The shell formation on a NW can be considered layer-by-layer growth on a curved surface, which is attributed to the Frank–van der Merwe (FM) mode of growth during heteroepitaxial growth, as shown in Fig. 48(a). Meanwhile, the surface roughening in a core–shell NW heterostructure can be contributed to the QD formation on the epitaxial layer of NW, as illustrated in Fig. 48(b). Accordingly, we can address the surface roughening by determining the heteroepitaxial mode of the growth. Assuming

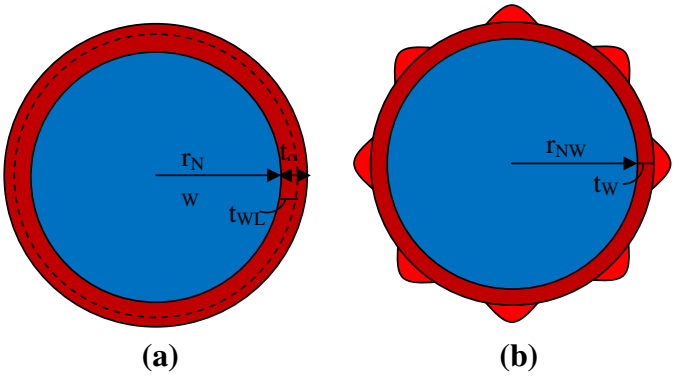

Fig. 48. Schematic illustration of the cross section of the heteroepitaxy on NW. (a) The FM mode, i.e., the core–shell structure. The total shell thickness t_o denoted in (a) is also the total thickness of the deposited layer both in the FM and SK modes. (b) The surface roughening on the core–shell structure by the SK mode. The radius of NW r_{NW} and the thickness of WL t_{WL} denoted in the FM and SK modes are both the same [32].

that the epitaxial layer with thickness t_o is deposited on the NW with length l_o, we first compare the change in energy caused by the two growth modes to identify which growth mode is more favorable. Because the NW surface is curved, the strain between the epitaxial layer and the NW becomes more complex than that of the situation on a planar substrate. The longitudinal strain component can be determined by the lattice mismatch between the epitaxial layer and the NW in the direction along the axis of NW and can be given by the following equation: $\varepsilon_z = \varepsilon_o$, where $\varepsilon_o = (a_{NW} - a_{shell})/a_{shell}$, here a_{NW} and a_{shell}, are the lattice constants of the NW and the shell material, respectively. Otherwise, there is no stress in the direction normal to the NW surface by omitting the effect of the two ends of the NW [360]. Additionally, the shear strain components are all equal to zero [118]. The contribution of curvature primarily acts on the strain ε_t in the tangential direction to the NW surface, which can be given by the following equation: $\varepsilon_t = \varepsilon_o - \frac{(r-r_{NW})(1-\varepsilon_o)}{r_{NW}}$, when $r < r_{NW}/(1-\varepsilon_o)$ [19]. If $r \geqslant r_{NW}/(1-\varepsilon_o)$, then the tangential strain component would be zero, where r is the distance of the given point to the center of NW, and r_{NW} is the radius of NW.

In the FM mode, the increase in the thickness of the epitaxial layer causes the change in the surface and strain energies, which can be written as follows:

$$E_{FM} = \frac{l_o}{n}[2\pi(r_{NW}+t_o)\gamma_{t_o} - 2\pi(r_{NW}+t_{WL})\gamma_{WL}] + \frac{2\pi l_o}{n} \times \int_{r_{NW}+t_{WL}}^{r_{NW}+t_o}\left[\frac{1}{2}c_{11}(\varepsilon_t^2+\varepsilon_z^2) + c_{12}\varepsilon_t\varepsilon_z\right]rdr \tag{4.20}$$

The first term describes the change in the surface energy, where t_{WL} is the thickness of the wetting layer (WL), and n is the density of QDs along the NW surface (the number of QDs along the NW surface). γ_{WL} and γ_{t_o} are the surface energies of the layer with thickness t_{WL} and t_o, respectively. We can obtain these values by the following equations: $\gamma_{WL} = \gamma_{substrate} + (\gamma_{film} - \gamma_{substrate})\left(1 - e^{\frac{t_{WL}}{h_o\eta}}\right)$ and $\gamma_{t_o} = \gamma_{substrate} + (\gamma_{film} - \gamma_{substrate})\left(1 - e^{\frac{t_o}{h_o\eta}}\right)$, where $\gamma_{substrate}$ and γ_{film} are the surface energy densities of the substrate and film with infinite thickness, respectively [361,362].

For the SK mode, QDs with base length l and contact angle α form on the NW, following with t_{WL} thickness of WL. The density of QDs in the longitudinal direction is n_o, i.e., the number of QDs along the axis of NW with length l_o. The change in the surface energy is expressed in the following equation: $E_s = n_o(\gamma_s S_1 - \gamma_{WL}S_2)$, in which γ_s is the surface energy density of QDs' side facet; S_1 is the area of side facet surface of a single QD; and S_2 is its base area. The strain energy change can be expressed as follows: $E_{el} = n_o V\left[\frac{1}{2}c_{11}(\varepsilon_{tWL}^2+\varepsilon_z^2) + c_{11}\varepsilon_{tWL}\varepsilon_z\right]$, where V is the volume of a single QD, and ε_{tWL} is the strain on the surface of WL in the tangential direction to the surface of NW. Considering that the strain in QDs is uniform, the average strain is expressed as follows: $\varepsilon_a = \frac{1}{2}(\varepsilon_{tWL} + \varepsilon_z)$. Thus, the variation in the relaxation energy of QDs is expressed as follows: $E_r = -n_o\kappa Y(1+\nu)/(1-\nu)\varepsilon_a^2 \tan\alpha V$, where κ is the shape factor. Furthermore, QDs along the direction of the NW axis are close to neighbors, i.e., the distance between two neighboring QDs is nearly zero based on the experimental roughening phenomena. Thus, the elastic interaction energy between any two QDs in the longitudinal direction can be expressed as follows: $E_{ini} = \frac{1+\nu}{1-\nu}\frac{1}{\pi}Y\varepsilon_a^2V^2\frac{1}{(il)^3}F\left(\frac{1}{2i}\right)$, where $F\left(\frac{1}{2i}\right)$ is the correction factor [361], and $i-1$ is the QD number between the two QDs. Hence, the total elastic interaction energy in the length of l_o, with n_o QDs, is expressed as follows: $E_{in} = \sum_{i=1}^{n_o-1}(n_o - i)E_{ini}$. Therefore, the energy change in the SK mode is expressed as follows:

$$E_{SK} = E_s + E_{el} + E_r + E_{in} \tag{4.21}$$

Based on the energy change in the FM and SK modes, we compare the two modes and obtain the energy difference using the following equation:

$$E = E_{FM} - E_{SK} \tag{4.22}$$

If the energy difference $E < 0$, then the FM mode is more favorable, i.e., the core–shell NW structure can be present. In contrast, if $E > 0$, then the SK mode is preferential. As a result, the roughening phenomena will appear. Thus, we can obtain the critical thickness of WL by $E = 0$. If the epitaxial layer

is less than the critical thickness of WL, then the core–shell NW structure can be obtained. If the layer continues to thicken and exceeds the critical thickness of WL, then QDs would form on the surface of NW, i.e., the surface of NW begins to roughen.

We can use the reciprocal of the longitudinal density or the base length of QDs to describe the periodicity of roughening, whereas the amplitude can be represented by the distance between the top of QDs to the planar surface. The height of QDs is only the amplitude until the QDs overlap with each other. After t_o thick layer deposited on NW, QDs with base length l and contact angle α have formed. Thus, we assume that there is an additional Δt layer deposited on QDs. Then, the increased volume of a single QD would be $\Delta V = \pi \tan\alpha\left(\frac{1}{4}l^2\Delta t + \frac{1}{2}l\Delta t^2 + \frac{1}{3}\Delta t^3\right)$. Because of the increase in the deposited layer, the total energy of QDs in the longitudinal direction with length l_o of NW would change. The surface energy would change due to the increase in the surface area and could be expressed as follows: $\Delta E_s = \frac{\pi l}{\cos\alpha}\Delta t\gamma_s n_o$. Furthermore, the change in the strain energy and in the relaxation energy can be given by the following equations: $\Delta E_{el} = \left[\frac{1}{2}c_{11}(\varepsilon_t^2 + \varepsilon_z^2) + c_{12}\varepsilon_t\varepsilon_z\right]\Delta V n_o$ and $\Delta E_r = -\kappa Y(1+\nu)/(1-\nu)\varepsilon_a^2\Delta V n_o$, respectively. Otherwise, we can obtain the change in the interaction energy by comparing the energies before and after Δt layer deposited. Hence, the change in the interaction energy can be expressed as follows: $\Delta E_{in} = \sum_{i=1}^{n_o-1}(n_o - i)\frac{1+\nu}{1-\nu}Y\overline{\varepsilon}^2\frac{\tan\alpha}{24}\frac{\Delta V}{i^3}F\left(\frac{1}{2i}\right)$. Based on all of the above-mentioned energy changes, we can obtain the total energy change as follows:

$$\Delta E = \Delta E_s + \Delta E_{el} + \Delta E_r + \Delta E_{in} \tag{4.23}$$

The total energy would always increase with the deposited layer increasing, i.e., ΔE is always bigger than zero. The change in the total energy can reflect the stability of QDs on NW to a certain extent by their value. Thus, QDs with different densities and volumes can have the same probability to form on the core–shell NW structure with different radii of NW, as long as their changes in energy are identical. The surface roughening on the core–shell NW structures with different radii would exhibit different periodicities and amplitudes, even with the same thickness of the deposited layer.

Using the Ge-core/Si-shell NW structure as an example in this study, we can obtain the energy difference E between the FM and SK modes with various thicknesses of WL and radii of NW based on Eq. (4.22), as shown in Fig. 49. The darkness degree in the figures represents the value of energy difference. With the same radius of NW, the energy difference increases from less than zero to larger than zero with the WL thickening. Thus, the epitaxial growth mode would converse from the FM to the SK modes with the increase in the WL thickness. Furthermore, the critical thickness of WL obtained by the energy balance between the two modes could be the dividing line between the two modes. Hence, the shell would first form on the surface of the NW, which accomplishes the core–shell NW structure, with a layer deposited on the NW. When the deposited layer exceeds the critical thickness of WL, then QDs begin to form, i.e., the surface roughening appears in the core–shell NW structure. Therefore, we can determine the two modes based on the critical thickness. Thus, we can avoid the surface roughening and achieve the perfect core–shell NW structure by moderating the thickness of the deposited layer according to the above analysis.

The important difference between the epitaxial growth on the planar substrate and the NW surface is the curved surface of the NW. The curved surface can alter the distribution and value of the strain that led to the change in the elastic energy. The radius of the NW determines the curviness of the NW surface and results in the variation in the energy difference caused by the two modes. From Fig. 49, we can see that the difference in energy would decrease from larger than zero to less than zero with the radii of the NW if the thickness of WL remains constant. Thus, the radii of the NW can cause the transition of the growth mode when the deposited layer maintains a certain amount. Otherwise, we can obtain the critical radius of the NW with a certain amount of the deposited layer. If the radius of the NW exceeds the critical value, then the core–shell NW structure is favorable for existence, whereas QDs would form when the radius is smaller than the critical radius.

According to the above analysis, both the thickness of the deposited layer and the radius of the NW play important roles in determining the epitaxial growth mode. In Fig. 49, the denoted zero presents the situations in which the energy difference is equal to zero. The line shows that the critical thickness of WL would increase with the radius of the NW, whereas the critical radii of the NW would increase

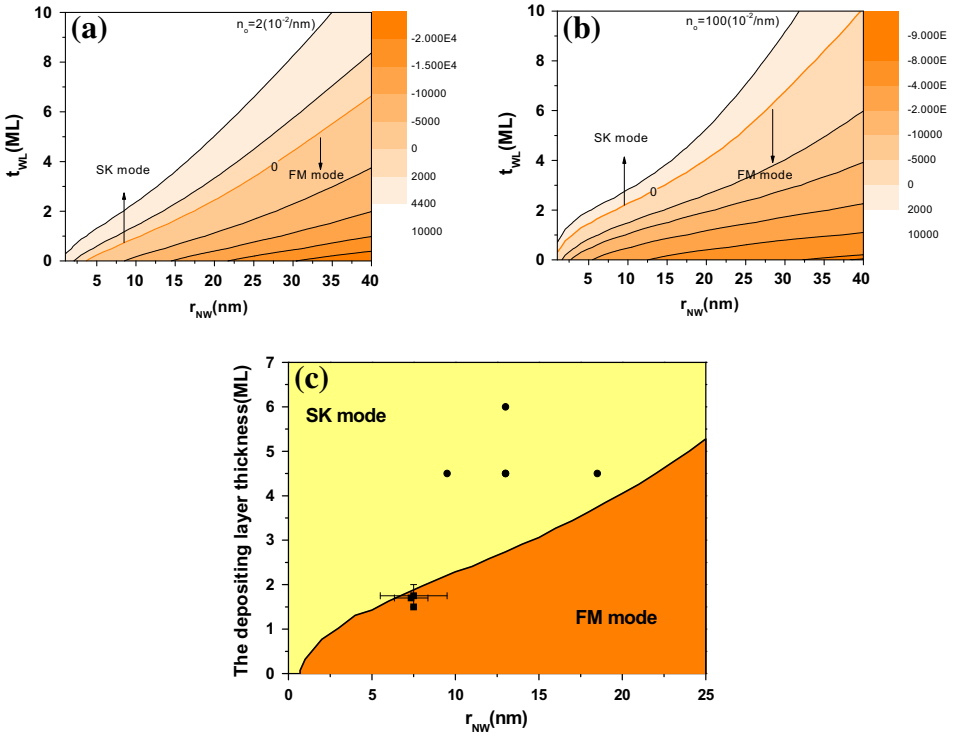

Fig. 49. The energy difference E caused by the two modes as functions of various radii of NW and thickness of WL with longitudinal density of QDs $n_o = 2$ (a) and 100 (b). The value of energy difference is presented by the degree of the orange and the units are *eV*. (c) Phase diagram of surface roughening on the core–shell NW with the radius of NW and the thickness of depositing layer, based on the critical thickness of WL [32].

with the deposited layer thickening. Obviously, the zero energy difference line could be the dividing line to separate the FM and SK mode regimes. The regime above the critical line enables the formation of QDs, whereas the FM mode becomes favorable in the regime below the critical line.

According to the quantitatively thermodynamic model [32], we find that the competition between the two epitaxial growth modes determines the final growth behavior and that the periodicity and amplitude of roughening can be controlled by modulating the radius of the NW and the thickness of the deposited shell layer.

5. Thermodynamic treatments within a statistical and quantum mechanics framework for the temperature-dependent growth of nanostructures

The previous theoretical treatments of the growth of semiconductor nanostructures have always been thermodynamics-based energy theories. In the simple energetic model, nanostructures would tend to locate in a stable state, whereas the energy would decrease to a minimum. Therefore, the energy theory has been successfully used to address many of the growth behaviors of nanostructures. However, the energy model always chooses thermal equilibrium and completely neglects thermal fluctuations. In fact, high entropic gains of the (thermodynamically extensive) interface would lead to various stable states. Thus, the thermodynamics-based energy theory cannot address the effect of thermal fluctuations on the growth of nanostructures, which is one of the most important growth conditions that affect the formation of nanostructures. In fact, the entropic gains of the interface would be high enough to destroy the thermal equilibrium stability during the growth compared with

the whole system. Therefore, it is essential and urgent to develop a new theoretical treatment that includes thermal effects to understand the temperature-dependent growth characteristics. Based on the fundamental energy theory, we introduce a thermodynamic treatment that includes thermal effects within the context of a statistical, mechanical, and quantum mechanical model [33–37], in which thermal fluctuations are added to nanostructures that leads to the oscillations of the nanostructure surface.

5.1. Thermal stability of the wetting layer in QD self-assembly

The wetting layer (WL) plays a crucial role in QD self-assembly [21,198,221]. The thickness of the WL is usually described by a constrained thermodynamic equilibrium between the QD and WL [99,150]. As an ideal system, Ge QDs could be generated on Si substrates following triple monolayer (ML) WL [363,364]. However, experimental results revealed that the thickness of the WL is between 1.7 and 8 ML [365,366]. This disagreement between theory and experiment could be attributed to the neglect of thermal effects in the present theoretical treatment [99,137,363,367]. The dependence of the thickness of WL as a function of the growth temperature has been reported in experimental studies [63,71,108,368–370], which have shown that thermal effects have a large influence on the formation of QDs and that the surface of QDs begins to oscillate and to become unstable due to thermal effects. Therefore, thermal fluctuations can alter the surface energy, which is important for determining the thickness of the WL. However, we always neglect thermal fluctuations in the present thermodynamic theory [99,137,363]. For this issue, we established a theoretical model to address the temperature-dependent thickness of the WL by introducing thermal effects based on statistical mechanics.

5.1.1. Temperature-dependent thickness of the wetting layer

Thermal effects can generate QD surface oscillation and instability, which alter the surface energy and breaks thermal equilibrium. Thus, the thickness of the WL in relation to the energy varies from the influence of thermal effects. To investigate the effect of temperature on the thickness of the WL, we first focus on the QD stability with base radius r, contact angle α, and WL thickness t_0 by considering the energy for a QD unit area. The relaxation energy of a single QD can be expressed as follows:

$$E_r = -M\varepsilon^2 \tan\alpha V \tag{5.1}$$

Treating the QD facet as a step facet, the surface energy includes the surface energy of terraces and the energy of step edge creation, which can be written as follows:

$$E_s = \gamma(t_{n_T+1})A_{n_T+1}\sum_{n=1}^{n_T}\gamma(t_n)A_n + 2\pi(r - nh_0\cot\alpha)\left[\lambda_0 + \lambda_d\left(\frac{a\tan\alpha}{h_0}\right)^2\right] \tag{5.2}$$

The first term represents the surface energy of terraces. The term $\gamma(t_n) = \gamma_{sub} + (\gamma_{film} - \gamma_{sub})(1 - e^{-t_n})$ is the film surface density [40] with a monolayer thickness of t_n. The second part represents the energy of the step edge creation. Considering the average surface cross-section $\overline{S} = \pi(\frac{1}{2}r)^2$, we obtain the energy per unit QD area based on Eqs. (5.1) and (5.2) as follows:

$$V = 4\frac{E_r + E_s}{\pi r^2} \tag{5.3}$$

To explore QD thermal stability, we simply consider the fluctuations in the QD cross-section boundaries. The QD base radius r fluctuates in the range $0 \leqslant \theta \leqslant 2\pi$. The boundaries are allowed to oscillate with an elastic energy of $(k/2)r^2$ and to interact via a local potential V. Based on the energy associated with fluctuations, the partition function can be written as follows:

$$Z(\beta) = \int\prod_r [dr]e^{-\beta\int_0^{2\pi} d\theta[(k/2)r^2 + R^{*2}V/2]} \tag{5.4}$$

Additionally, the integral in Eq. (5.4) is limited to the circular region $r(\theta) = R^*$, where R^* is the QD base radius at minimum energy. Using the density matrix and the standard transformation, Eq. (5.4) can be expressed as follows:

$$Z = \left(\frac{2\pi}{\beta k\lambda}\right)^{2\pi\lambda} Tr[\exp(-2\pi H_\beta)] \tag{5.5}$$

The temperature-dependent Hamiltonian can be written as follows:

$$H_\beta = -\frac{1}{2\beta k}\frac{d^2}{dr^2} + \frac{\beta}{2}R^{*2}V \tag{5.6}$$

The free oscillator contribution is contained in the trace coefficient. The linear density of the oscillators is $\lambda = K/k$, in which K is the microscopic spring constant. From the QD elastic energy, we deduce the elastic constant to be $k = \frac{4}{3}\frac{\gamma}{1-\nu}\varepsilon^2 h$. We assume k is independent of temperature because the elastic modulus variation is small as a function of temperature [371,372].

The Hamiltonian can be projected onto the lowest bound state, as given by $\widehat{H}_\beta\psi_\beta(r) = E_\beta\psi_\beta(r)$. Then, we obtain the probability of the QD base radius by the expression $p(r) = |\psi_\beta(r)|^2$. Thus, we can probabilistically deduce the thermal stability of a QD. If the probability is constant, then the QD cannot maintain stability because of the equipotential probability. However, if the probability is not constant, then the QD can remain stable. Moreover, based on previous research, the existence of a bound state in $\widehat{H}_\beta$ determines whether the probability $p(r)$ is constant [33,34]. Therefore, we can obtain QD stability by verifying the existence of a bound state in a suitable one-particle Hamiltonian operator.

5.1.2. Critical temperature for the stability of the wetting layer

The potential in Eq. (5.6) is a linear potential with a small potential barrier. The linear potential is limited to the largest value because the QD base radius cannot be smaller than zero. Thus, we cannot confirm that there is a bound state with the potential. Accordingly, the QD cannot always maintain stability. We try to resolve the problem of bound state disappearance by the quantization rules in the WKB approximation [373]. The classically allowed range in the quantization rules is from zero to infinity, in theory. However, the QD base radius cannot be infinitely large because this size may cause the QD to coalesce and to form a continuous film [374]. Thus, the integration limits in the quantization rules are from zero to the largest QD base radius upon consideration of the size limitation. From the WKB approximation, we can obtain the critical temperature corresponding to the disappearance of the lowest bound eigenstate as follows:

$$T_c = \frac{2R^*}{\pi}\int_0^{R_m}\sqrt{k(E_\beta - V)}dr \tag{5.7}$$

We choose the lowest energy of the single particle E_β as the upper limit of the potential. Accordingly, QDs grown at a temperature above the critical temperature T_c will not always remain stable because of the bound state disappearance. However, the Hamiltonian will have at least one bound state if the temperature is below T_c, and the QD will be stable. Thus, the critical temperature is the dividing line for QD stability. The maximum QD base radius clearly determines the limits of the potential and plays important roles in the critical temperature.

Comparing the WL thickness of Ge QD on Si substrates with Si QD on Ge substrates, we check the validity of the above proposed model. Using Eq. (5.3), we compare the potential of the two systems. Fig. 50 shows the behavior of the potential with the QD base radius. The potentials of both systems decrease linearly with the radius, and the small barrier with a radius near zero can be ignored when compared with the large potential. Thus, the base radii R^* with minimum energy are equal to the maximum base radii R_m. However, the difference in the two potentials is exhibited by the WL thickness shown in Fig. 51. The Ge QD potential decreases with increasing thickness, whereas the Si QD potential increases with increasing thickness. The two lines in Figs. 51(a) and (b) represent the QD potential with 10 nm and 20 nm base radii, respectively. Although the radii values differ, the trends of the two lines are identical in both figures. The difference in the two potentials in Figs. 51(a) and (b) is caused by differences in the QD surface energy density.

With the dependence of the potential on the base radius, as shown above, we can obtain the critical temperature behavior by integration using Eq. (5.7) and the quantization rules. Fig. 52 shows the dependence of the critical temperature as a function of the maximum base radius R_m. The solid line

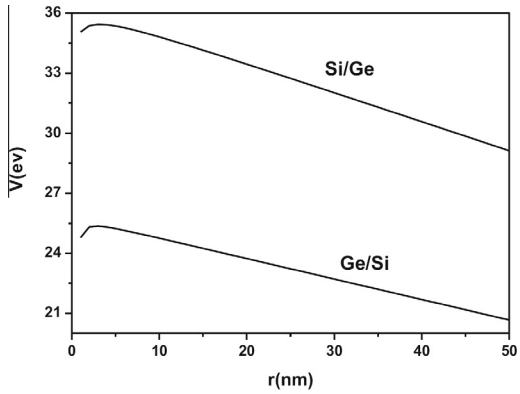

Fig. 50. The potential energy of QD as a function of the base radii of QD which is used in the integral. The above line is the potential energy of Si QD on Ge substrates while the other line is the potential energy of Ge QD on Si substrates [37].

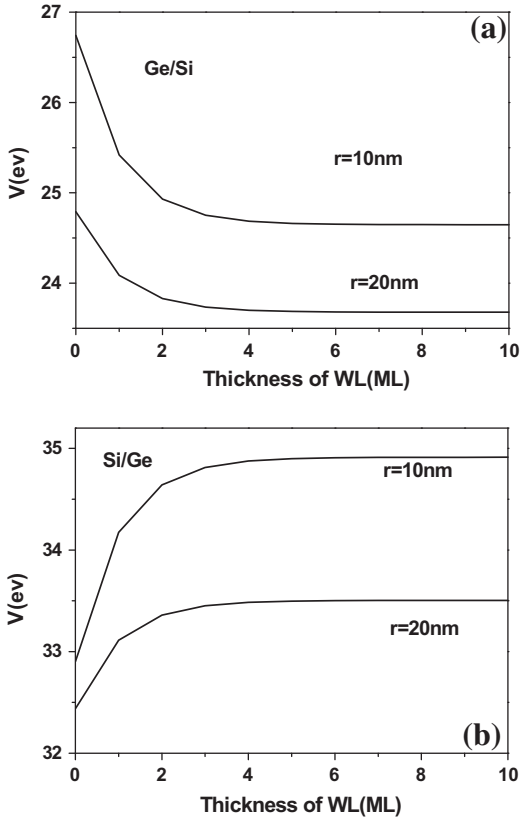

Fig. 51. (a) The potential energy of Ge QD with the thickness of WL. The two lines represent the Ge QD with base radii $r = 10$ nm and $r = 20$ nm respectively. (b) The potential energy of Si QD with $r = 10$ nm and $r = 20$ nm vs the thickness of WL [37].

and the line with the symbol represent the Ge QD and Si QD, respectively. Despite having different radius values, the critical temperature lines both increase with the maximum base radii. Therefore, larger QDs have higher critical temperatures, and smaller maximum base radii cause the critical

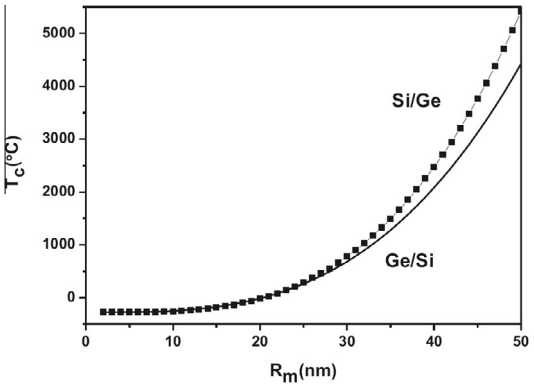

Fig. 52. The critical temperature corresponding to the stability of QD vs the maximum base radii of QD. The solid line represents the critical temperature of Ge QD on Si substrates. The dot line is the critical temperature of Si QD on Ge substrates [37].

temperature to be lower. The QD is stable if grown at a temperature below the critical temperature. If the temperature increases above the critical temperature, then the QD becomes unstable. Therefore, we deduce that stable QDs grown at higher temperatures can be obtained by increasing the QD size.

Furthermore, the WL thickness of WL is assumed another important factor for the critical temperature. With a maximum base radius of 30 nm [374], we obtain the relation between WL thickness and critical temperature, as shown in Fig. 53. The Ge QD critical temperature decreases with increasing WL thickness, as shown in Fig. 53(a). Ge QDs can only stably form at a temperature below the critical temperature line. Additionally, QDs with thick WLs have lower critical temperatures. From the critical temperature line, we deduce that the WL thickness does not exceed a critical value at a given temperature. The QD can form only with a thickness smaller than the critical value. The critical value of WL thickness from the critical temperature becomes thicker if the growth temperature decreases. If the temperature is high enough, then the WL thickness decreases until complete disappearance. Interestingly, all experimental data [63,71,108,368–370] are in the region below the critical temperature line, and the WL thicknesses are all smaller than the critical value. Moreover, in experiments, the maximum WL thicknesses with different growth temperatures increase with a decrease in temperature, which is consistent with our conclusion.

We also compare the critical temperature behavior of Si QDs grown on Ge substrates with the WL thickness to the experiments shown in Fig. 53(b). Unlike the Ge QD, the Si QD critical temperature increases with increasing WL thickness. QDs can also stably form below the critical temperature. However, the QD critical temperature with a thicker WL is larger. Contrary to the behavior of Ge WLs, the critical value of Si WLs thickens with increasing temperature. Pachinger et al. [375] reported concerning the WL thickness of Si QDs on Ge substrates with different growth temperatures. These authors found that the thickness increases with increasing temperature. All experimental data are in the region below the critical line, and the trend is in good agreement with our conclusion.

5.2. Temperature-dependent growth of NW orientation

We perform the case concerning temperature-dependent growth of NW orientation. Thus far, vapor-phase synthesis is most likely the most extensively explored approach to prepare all types of semiconductor NWs, and the VLS process seems to be the most successful for growing NWs [7,376–379]. However, the commonly grown out-of-plane NW geometry imposed by the VLS process appears to be an obstacle to the current planar processing technology of microelectronic and optoelectronic devices [380,381]. To control the growth direction of NWs from the substrate, for example, vertically or horizontally aligned, we require a deep understanding of the VLS process. Generally, a typical VLS process starts with the dissolution of gaseous reactants into nano-scaled liquid droplets in the presence of a catalyst metal. Once the liquid droplet is supersaturated with the metal, NW nucleation

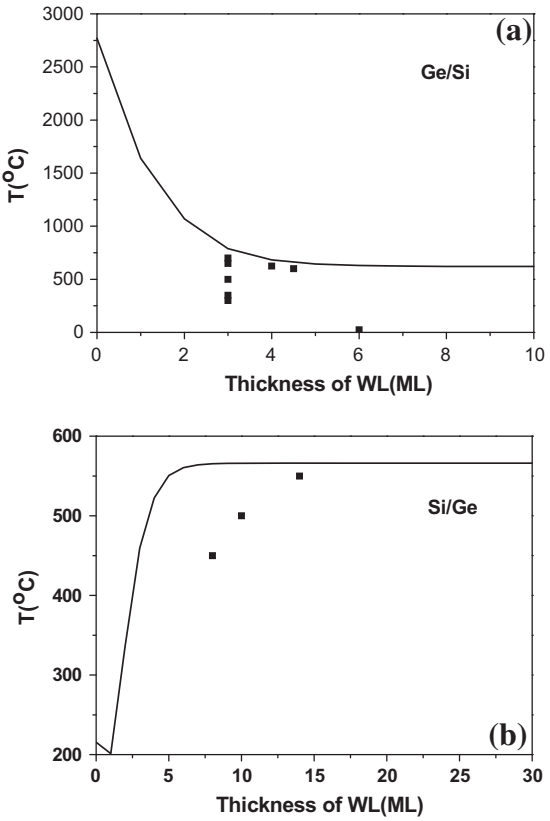

Fig. 53. (a) The critical temperature of Ge QD on Si substrates as a function of thickness of WL. The experimental data are from Refs. [63,71,108,369,370]. (b) The critical temperature of Si QD on Ge substrates with the thickness of WL (The experimental data of QD with different thickness of WL at various temperatures are from Ref. [375]) [37].

and growth will occur at the solid–liquid interface. Thus, this growth is induced and dictated by the liquid droplets [7]. Meanwhile, growth directions of NWs are determined by the surface free energy from the perspective of the energy theory based on thermodynamics [382,383]. From this viewpoint, each liquid droplet serves as a soft template to limit the lateral growth of NWs. Therefore, previous theoretical treatments of the VLS NW nucleation and growth have been based on the energy theory of thermodynamics [310,321,384,385]. As an important characteristic, the NW direction can be affected by growth conditions, such as substrate orientation and materials [384,386]. Recently, reports have shown that this growth direction depends on temperature [381,386–391], which implies that thermal effects underlie the growth mechanism. For this issue, we have established a theoretical model to quantitatively address temperature-dependent growth via the VLS process by introducing the effect of thermal fluctuations.

5.2.1. Thermal fluctuations during the VLS process

Previous studies have shown that the growth direction of NWs depends on the orientation of the NW nucleus during the VLS process [31,297,382,383]. In this study, we focus on the stability of the nucleus. Considering the thermal effect, the nucleus surface would oscillate and become unstable. For this study, we first calculated the energy of formation per unit area for NW nucleation as a function of direction. The Gibbs free energy of formation, including contributions from surface (G_s) and volume (G_g), can be expressed as follows [35]:

$$G = \sigma_{nv} R^2 s(\alpha) + \left(\frac{1}{2}\Delta g_v^0 - \frac{\sigma_{nv}}{R}\right) R^3 t(\alpha) \tag{5.8}$$

Accordingly, we obtain the formation energy for unit area of nucleus as follows:

$$V = \frac{G}{S} = \frac{\sigma_{nv} s(\alpha) R^2 + \frac{1}{2}\Delta g_v^0 t(\alpha) R^3}{\frac{1}{2}[s_1(\alpha) + s_2(\alpha)] R^2} \tag{5.9}$$

Based on the condition for critical nucleus formation, $\frac{\partial G}{\partial R} = 0$, if the atomic cluster transforms into a critical nucleus, then we can calculate the radius of the critical nucleus as follows: $R^* = -\frac{4}{3}\frac{\sigma_{nv}}{\Delta g_v^0}\frac{s(\alpha) - t(\alpha)}{t(\alpha)}$.

Given different directions, the morphology of the nucleus would change. Fig. 54 illustrates the variety of nuclei with different shapes and orientations. To compare the different orientations, we simply use Fig. 54(a) as the origin. Figs. 54(b–e) show the nucleus with different angles α to the original substrate direction. The complement $\frac{\pi}{2} - \alpha$ is the angle between the NW and the substrate. Given the area and volume factors in Eqs. (5.8) and (5.9), we obtain the angle dependence of the energy per unit area for the nucleus.

To explore the thermal stability of the nucleus, we consider thermal fluctuations of its cross-sectional boundaries; the radii of these cross-sections r fluctuate with polar coordinate, $0 \leqslant \theta \leqslant 2\pi$. The boundaries are allowed to oscillate with elastic energy $(k/2)r^2$ and to interact via a local potential V. Based on the energy associated with these surface fluctuations, the partition function can be expressed as follows:

$$Z(\beta) = \int \prod_r [dr] e^{-\beta \int_0^{2\pi} d\theta [(k/2)r^2 + R^{*2} V/2]} \tag{5.10}$$

where $\beta = 1/k_B T$. The integral in the exponent of the Eq. (5.10) is the energy of the cross-sectional surface of the nucleus. We assume a system of only one radius r as a single particle because the fluctuations only depend on r. Thus, the integrand in the exponent is the single-particle energy under our

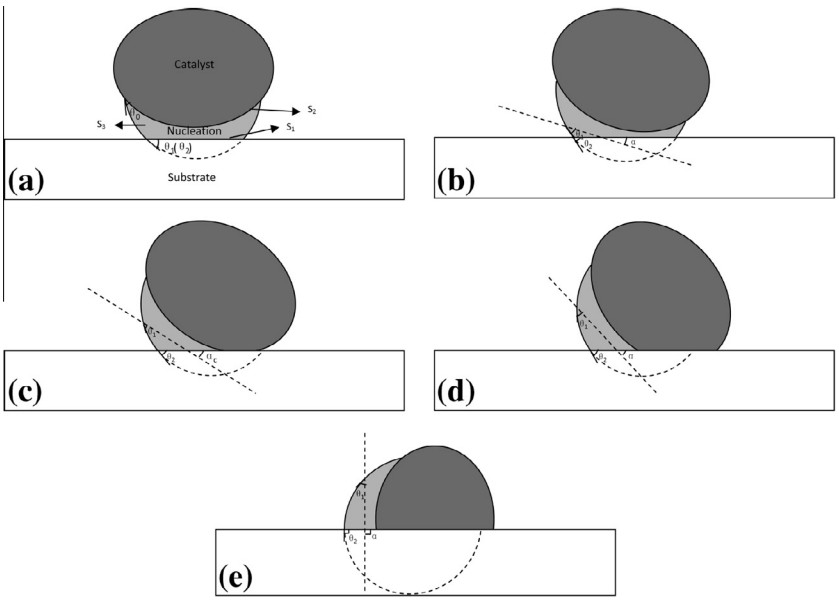

Fig. 54. Schematic illustration of NW nucleus with various directions. Taking (a) as the initial state of the orientation of nucleus. The dashed line in (b–e) is the substrate position with the initial direction of nucleus, and the angle α between the substrate and the dashed line shows the various direction of nucleus. The angle α in (c) is the critical angle α_c which is the demarcation point of two different morphology of nucleus [35].

assumptions. By introducing the density matrix and the standard transformation [141,392], Eq. (5.10) can be written as follows:

$$Z(\beta) = \left(\frac{2\pi}{\beta k\lambda}\right)^{2\pi\lambda} Tr\left[\exp\left(-\frac{4\pi}{R^{*2}}\widehat{H}_\beta\right)\right] \tag{5.11}$$

in which the temperature-dependent Hamiltonian can be expressed as follows:

$$\widehat{H}_\beta = -\frac{R^{*2}}{4\beta k}\frac{d^2}{dr^2} + \frac{\beta}{4}R^{*4}V \tag{5.12}$$

The energy for free oscillators is contained in the coefficient in front of the trace, in which λ is the linear density of oscillators and can be expressed as $\lambda = K/k$, where K is the microscopic spring constant. Because $r = R\sin\theta_2$, the Hamiltonian can be re-expressed as follows:

$$\widehat{H}_\beta = -\frac{R^{*2}}{4\beta k\sin^2\theta_2}\frac{d^2}{dR^2} + \frac{\beta}{4}R^{*4}V \tag{5.13}$$

We can obtain its lowest bound eigenstate from the following relation: $\widehat{H}_\beta\psi_\beta(r) = E_\beta\psi_\beta(r)$. Thus, the probability for the cross-sectional radius of the nucleus is expressed as follows: $p(r) = |\psi_\beta(r)|^2$. If the Hamiltonian $\widehat{H}_\beta$ has no bound state, then the probability $p(r)$ would be constant. The equipotent probability for various radii leads to an unstable nucleus; as long as the probability $p(r)$ is not constant, the nucleus has a stable regime. However, with the existence of a bound state in $\widehat{H}_\beta$, we can deduce whether $p(r)$ is constant [33]. Therefore, nucleus stability can be judge by the existence of a bound state in a suitable one-particle Hamiltonian operator.

5.2.2. Critical temperature for growth direction of NWs

The potential in Eq. (5.13) linearly depends on the radius of the nucleus. For general linear potentials, the energy spectrum would change from being discrete to continuous without restriction from the rigid wall at the lowest potential. Hence, the bound state does not always exist with a linear potential. Considering that the radius of a nucleus is always a positive value, the potential has only a maximum finite potential; meanwhile, the lower bound of the potential is infinite. The linear potential cannot ensure that a bound state is present, *i.e.*, the nucleus is not always stable. In this study, we solve the problem using the quantization rules in the WKB approximation [373]. The classically allowed range, which is used in the quantization rules, is from zero to infinity, in theory. However, nucleus sizes are finite in practice and are necessarily restricted by catalyst size [297,321]. By adding a size limitation to the classically allowed range, the limits of integration in the quantization rules become $0 \sim R_m$, with R_m the maximum radius of the nucleus. Accordingly, we can obtain a critical temperature corresponding to the disappearance of the lower bound eigenstate as follows:

$$T_c = \frac{4}{3\pi}R_m^{\frac{3}{2}}R^*\sin\theta_2\sqrt{\frac{-\Delta g_\nu^0 kt(\alpha)}{s_1(\alpha)+s_2(\alpha)}} \tag{5.14}$$

The critical temperature determines the stability of nucleus: if $T > T_c$, then there are no bound states, thus, no stable nucleus, whereas if $T < T_c$, then the nucleus is stable because the Hamiltonian has at least one bound state, and from the nucleus, a NW can form and grow.

Interestingly, we have obtained the critical temperature from the potential energy. Leaving aside the effect of the nucleus size, the potential depends on surface and volume factors through introducing the identity $\cos\theta_2 = \cos\theta_1\cos\alpha$. In our above analysis, these factors are determined by angle α such that the critical radius of the nucleus is also a function of α. Considering the dependence of Δg_ν^0 on temperature, we define $\Delta g_\nu^0 = T\Delta g_T^0$, where Δg_T^0 is assumed constant. Accordingly, we can relate the critical temperature to the growth direction α as follows:

$$T_c(\alpha) = \left(\frac{16\sigma_{n\nu}}{9\pi}\right)^{\frac{2}{3}}R_m\left\{-\frac{k}{\Delta g_T^0}(1-\cos^2\theta_1\cos^2\alpha)\frac{[s(\alpha)-t(\alpha)]^2}{t(\alpha)[s_1(\alpha)+s_2(\alpha)]}\right\}^{\frac{1}{3}} \tag{5.15}$$

The nucleus will have various angle-dependent critical temperatures $T_c(\alpha)$ and will be stable if the growth temperature is below that critical temperature; NWs will preferentially grow along that direction at the exclusion of other directions. Hence, we have deduced a temperature-dependent growth direction for NWs.

Using the growth of GaAs NWs on the Si substrate as an example, we check the validity of the above model. Fig. 55(a) shows the potential of the nucleus as a function of angle α. Because different α values lead to different nucleus morphologies, the potential energy is different. The radial dependence of the potential, which is used in the integral to obtain the critical temperature, is shown in Fig. 55(b). The two different lines illustrate the nucleus with $\alpha > \alpha_c$ and with $\alpha < \alpha_c$, respectively. Despite a varying α values, trends in the potential stay the same. As the radius increases, the potential decreases and determines a maximum radius, which we choose as 25 nm [390,391]. Based on this trend in potential, we can obtain the critical temperature by integration. Assume the parameters in Eq. (5.14) are all constants except the maximum of radii R_m.

Furthermore, the nucleus angle α dictates growth direction: if $\alpha = 0°$, then the NWs are grown vertically to the substrate, whereas for $\alpha = 90°$, planar NWs are formed. The angle dependence of critical temperature is plotted as the solid line in Fig. 56 based on Eq. (5.15). At temperatures below the critical line, the NWs grow at a preferential direction. An undulation curiously appears if α is smaller than approximately 50°. In the temperature range below the value of the dashed line in Fig. 56, all NWs with α smaller than 50° have a certain probability of occurring; hence, at lower temperatures, NWs grow in haphazard directions. However, if the temperature is above those values represented by this

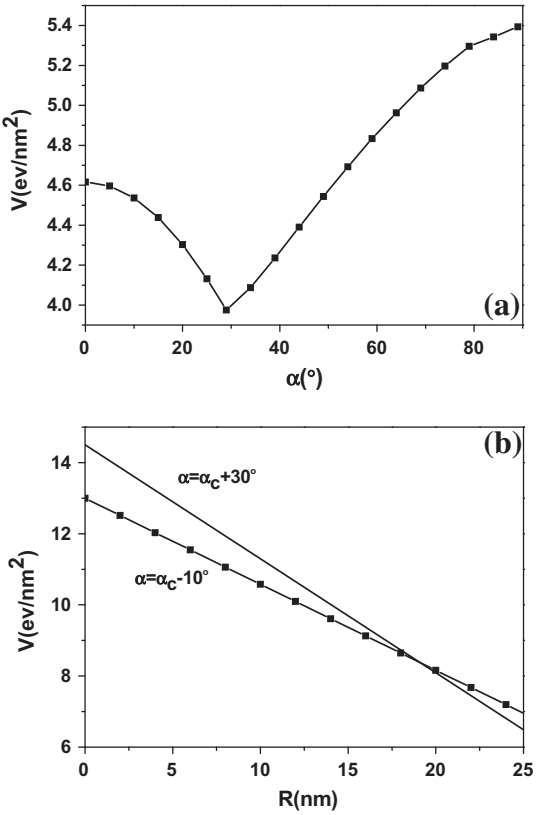

Fig. 55. (a) The potential energy of GaAs nucleus with various angle α. The lowest point is the critical angle. (b) The potential energy of nucleus vs the radii. The real line and dashed line represented the nucleus with $\alpha = \alpha_c - 10°$ and $\alpha = \alpha_c + 30°$, respectively [35].

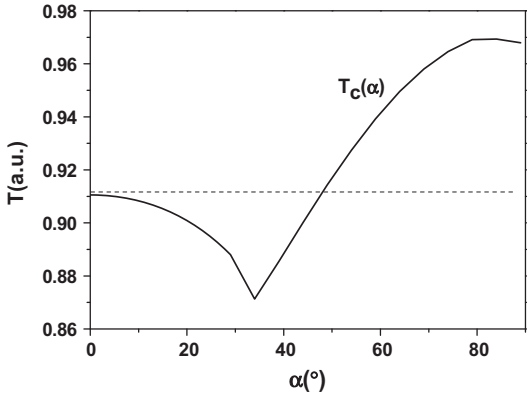

Fig. 56. The critical temperature as functions of the angle α, which denotes the growth direction of NWs [35].

dashed line, then stable NWs form at an increasing greater angle α as temperature increases, becoming more planar-aligned in the process. Because the material parameters enter as a morphological factor, the deductions we have obtained above are universal.

In experiments [381], temperature was modulated to change the GaAs NW growth direction on GaAs(100) substrate. NWs grown at low temperature are cluttered; some NWs grew vertically to the substrate, and some inclined at approximately 35.3°. At higher temperatures, planar NWs grew. Cai et al. [387] reported temperature-dependent growth directions of ZnSe NWs. The NWs were inclined at 55° from the GaAs(001) substrate at 530 °C. When the growth temperature was lowered to 390 °C, then NWs were predominantly vertical to the substrate but haphazardly inclined at approximately this angle. Another experimental report [391] described Si NWs grown on a Si(111) substrate at temperatures between 450 °C and 600 °C. In addition, yields of vertical NWs decreased with increasing temperature. Zhang et al. [388] reported GaAs NW growth from a GaAs [311]B substrate. The vertical or inclined NWs were grown at temperatures lower than 460 °C. When the growth temperature was increased to 500 °C, then the authors found that all NWs grew laterally on the substrate. All of these experiments are in agreement with our conclusions; the direction of NWs can be modulated by temperature, with growth tending to be planar at higher temperatures and stable with smaller α values at lower temperatures.

6. Summary

In summary, we have reviewed the progress of the thermodynamic theoretical treatments of the growth of nanostructures, including the growth of QDs by epitaxy, QRs by droplet epitaxy, and NWs by the VLS process in the recent years. Based on these investigations, the assemblies and growth at the nanometer scale have revealed many unusual thermodynamic and kinetic behaviors of the microphase growth. The thermodynamic theory could be applicable to the physical understanding of the growth of nanostructures.

We have shown that the growth of QDs by epitaxy can be understood by thermodynamics-based energy theories. In particular, the relaxation of QDs drives the formation of QDs, whereas the thickness-dependent surface energy of WL restricts the growth of QDs. The physical origin of the shape transition of QDs has been shown to be related to the balance between the surface energy and relaxation energy of QDs. We have also shown that the growth of QDs on patterned substrates and in multilayered systems can be understood through the surface chemical potential and thermodynamics aspects for the formation of QDs.

We have shown that the growth of QRs by droplet epitaxy is directly related to the nucleation on the droplet's skirt and to the diffusion of atoms. The selective nucleation on the droplet's skirt leads to the QR formation at the initial deposition stage, and then the QR growth is controlled by the diffusion of atoms. Using the GaAs system as an example, by calculating the amounts of produced GaAs in each

point, we showed that the shape evolution of GaAs nanostructure during the crystallization process could be simulated based on a quantitative kinetic model.

Concerning the growth of NWs by the VLS process, we have systemically introduced a series of theoretical tools, i.e., thermodynamic and kinetic approaches, to address the nucleation, growth and phase transition of NWs, which elucidate the physical and chemical mechanisms involved in the growth of 1D nanostructures. In particular, the nucleation and size-dependent growth behaviors of NWs have been described by thermodynamic and kinetic models. Additionally, experiments regarding core–shell NW heterostructure growth were performed.

We have also presented a new theoretical treatment that includes thermal effects to understand the temperature-dependent growth of nanostructures. In particular, based on the fundamental energy theory, we introduced a thermodynamic treatment that included thermal effects within the context of a statistical, mechanical, and quantum mechanical model. The temperature-dependent growth of nanostructures can be understood by the new thermodynamic treatment.

However, thus far, there remain some issues in the theoretical treatments of the growth of nanostructures. First, the surface energy of nanostructures is anisotropic. Moreover, the surface can reconstruct or adsorb other species to reduce the surface energy. Considering the effect of surface anisotropy and reconstruction will allow us to investigate more experiments. Second, self-assembled nanostructures have an inhomogeneous composition. The distribution of composition plays a key role in thermodynamic properties. For example, intermixing and alloying can allow for a partial strain relaxation in the growth of nanostructures. The strain relaxation can cause a decrease in free energy and drive the nanostructures to a more effective state for strain relaxation, such as the segregation of the Ge at the top of the GeSi alloying QD. Therefore, the calculation for the stain energy of QD is usually higher than the reality when we assume that the composition is uniform. In addition, the inhomogeneous distribution of the composition also influences the surface of nanostructures. It is well known that the surface plays an important role in the properties of nanostructures. Therefore, the change in the surface caused by the inhomogeneous composition would affect the growth of nanostructures. For example, surface segregation results in a decrease in surface energy, which drives the atoms of elements with low surface energy to segregate at the surface. Therefore, the theoretical framework for covered alloying effects on growth should primarily consider the contributions of composition to the strain energy and to the surface energy. In this case, the extension of the existing theory to consider the distribution of composition will allow us to more accurately describe the origin of experimental observations. Third, there are some concomitant chemical reactions during the growth of binary compound nanostructures, particularly III–V and II–VI semiconductors. These chemical reactions also affect the growth of nanostructures. The extension of these effects would help us to understand and to design specific nanostructures in multi-element systems.

The last issue concerns the relation between thermodynamics and kinetics. Generally, Gibbs free energy is an adaptable measure of the stability of a state in phase transition. Thermodynamically, phase transformation is promoted by the difference in free energy. However, the thermodynamic criterion only provides the probability for the growth of nanostructures. Kinetics will play a key role in the achievement of the selection growth when the thermodynamic criterion operates. Therefore, kinetics provides an optional route to actualize the probability from thermodynamics. Therefore, a better understanding of the relation between thermodynamics and kinetics will allow us to more accurately design the growth of nanostructures.

Acknowledgments

The National Basic Research Program of China (2014CB931700), the National Natural Science Foundation of China, China (91233203 and 11104084) and the State Key Laboratory of Optoelectronic Materials and Technologies of Sun Yat-sen University supported this work.

References

[1] Moriarty P. Nanostructured materials. Rep Prog Phys 2001;64:297–381.
[2] Teichert C. Self-organization of nanostructures in semiconductor heteroepitaxy. Phys Rep 2002;365:335–432.

[3] Stangl J, Holy V, Bauer G. Structural properties of self-organized semiconductor nanostructures. Rev Mod Phys 2004;76:725–83.
[4] Kiravittaya S, Rastelli A, Schmidt OG. Advanced quantum dot configurations. Rep Prog Phys 2009;72:046502.
[5] Berbezier I, Ronda A. SiGe nanostructures. Surf Sci Rep 2009;64:47–98.
[6] Ratto F, Rosei F. Order and disorder in the heteroepitaxy of semiconductor nanostructures. Mater Sci Eng R: Rep. 2010;70:243–64.
[7] Frances MR. Controlling nanowire structures through real time growth studies. Rep Prog Phys 2010;73:114501.
[8] Wu J, Hu X, Lee J, Kim ES, Wang ZMM. Epitaxially self-assemblied quantum dot pairs. Adv Opt Mater 2013;1: 201–14.
[9] Shchukin VA, Bimberg D. Spontaneous ordering of nanostructures on crystal surfaces. Rev Mod Phys 1999;71:1125–71.
[10] Lee ST, Wang N, Lee CS. Semiconductor nanowires: synthesis, structure and properties. Mater Sci Eng A 2000;286:16–23.
[11] Wang N, Cai Y, Zhang RQ. Growth of nanowires. Mater Sci Eng R 2008;60:1–51.
[12] Skolnick MS, Mowbray DJ. Self-assembled semiconductor quantum dots: fundamental physics and device a tipplications. Ann Rev Mater Res 2004;34:181–218.
[13] Mano T, Kuroda T, Sanguinetti S, Ochiai T, Tateno T, Kim J, et al. Self-assembly of concentric quantum double rings. Nano Lett 2005;5:425–8.
[14] Aqua JN, Berbezier I, Favre L, Frisch T, Ronda A. Growth and self-organization of SiGe nanostructures. Phys Rep 2013;522:59–189.
[15] Wang CX, Yang GW. Thermodynamics of metastable phase nucleation at the nanoscale. Mater Sci Eng R 2005;49:157–202.
[16] Ouyang G, Wang CX, Yang GW. Surface energy of nanostructural materials with negative curvature and related size effects. Chem Rev 2009;109:4221–47.
[17] Wang CX, Yang YH, Xu NS, Yang GW. Thermodynamics of diamond nucleation on the nanoscale. J Am Chem Soc 2004;126:11303–6.
[18] Alivisatos P. Nanothermodynamics: a personal perspective by Terrell Hill. Nano Lett 2001;1:109.
[19] Li XL, Ouyang G, Yang GW. Thermodynamic theory of nucleation and shape transition of strained quantum dots. Phys Rev B 2007;75:245428.
[20] Li XL, Ouyang G, Yang GW. A thermodynamic theory of the self-assembly of quantum dots. New J Phys 2008;10:043007.
[21] Li XL, Yang GW. Theoretical determination of contact angle in quantum dot self-assembly. Appl Phys Lett 2008;92:171902.
[22] Li XL, Yang GW. Growth mechanisms of quantum ring self-assembly upon droplet epitaxy. J Phys Chem C 2008;112:7693–7.
[23] Li XL. Thermodynamic theory of quantum dot self-assembly on strained substrates. J Phys Chem C 2010;114:2018–21.
[24] Li XL, Ouyang G. Thermodynamic theory of controlled formation of strained quantum dots on hole-patterned substrates. J Appl Phys 2011;109:093508.
[25] Li XL. Selective formation mechanisms of quantum dots on patterned substrates. Phys Chem Chem Phys 2013;15:5238–42.
[26] Wang CX, Yang YH, Liu QX, Yang GW. Nucleation thermodynamics of cubic boron nitride upon high-pressure and high-temperature supercritical fluid system in nanoscale. J Phys Chem B 2004;108:728–31.
[27] Wang CX, Chen J, Yang GW, Xu NS. Thermodynamic stability and ultrasmall-sSize effect of nanodiamonds. Angew Chem Int Ed 2005;44:7414–8.
[28] Wang B, Yang YH, Xu NS, Yang GW. Mechanisms of size-dependent shape evolution of one-dimensional nanostructure growth. Phys Rev B 2006;74:235305.
[29] Liu QX, Wang CX, Yang YH, Yang GW. One-dimensional nanostructures grown inside carbon nanotubes upon vapor deposition: a growth kinetic approach. Appl Phys Lett 2004;84:4568–70.
[30] Liu QX, Wang CX, Yang GW. Nucleation thermodynamics of cubic boron nitride in pulsed-laser ablation in liquid. Phys Rev B 2005;71:155422.
[31] Liu QX, Wang CX, Xu NS, Yang GW. Nanowire formation during catalyst assisted chemical vapor deposition. Phys Rev B 2005;72:085417.
[32] Cao YY, Ouyang G, Wang CX, Yang GW. Physical mechanism of surface roughening of the radial Ge-core/Si-shell nanowire heterostructure and thermodynamic prediction of surface stability of the InAs-core/GaAs-shell nanowire structure. Nano Lett 2013;13:436–43.
[33] Nisoli C, Abraham D, Lookman T, Saxena A. Thermal stability of strained nanowires. Phys Rev Lett 2009;102:245504.
[34] Nisoli C, Abraham D, Lookman T, Saxena A. Thermally induced local failures in quasi-one-dimensional systems: collapse in carbon nanotubes, necking in nanowires, and opening of bubbles in DNA. Phys Rev Lett 2010;104:025503.
[35] Cao YY, Yang GW. Vertical or horizontal: understanding nanowire orientation and growth from substrates. J Phys Chem C 2012;116:6233–8.
[36] Cao YY, Yang GW. Temperature-dependent preferential formation of quantum structures upon the droplet epitaxy. Appl Phys Lett 2012;100:151909.
[37] Cao YY, Yang GW. Thermal stability of wetting layer in quantum dot self-assembly. J Appl Phys 2012;111:093526.
[38] Reithmaier JP, Sek G, Loffler A, Hofmann C, Kuhn S, Reitzenstein S, et al. Strong coupling in a single quantum dot-semiconductor microcavity system. Nature 2004;432:197–200.
[39] Badolato A, Hennessy K, Atature M, Dreiser J, Hu E, Petroff PM, et al. Deterministic coupling of single quantum dots to single nanocavity modes. Science 2005;308:1158–61.
[40] Xu X, Sun B, Berman PR, Steel DG, Bracker AS, Gammon D, et al. Coherent optical spectroscopy of a strongly driven quantum dot. Science 2007;317:929–32.
[41] Mowbray DJ, Skolnick MS. New physics and devices based on self-assembled semiconductor quantum dots. J Phys D: Appl Phys 2005;38:2059.
[42] Stranski IN, Krastanow L. Zur Theorie der orientierten Ausscheidung von Ionenkristallen aufeinander. Monatshefte für Chemie und verwandte Teile anderer Wissenschaften 1937;71:351–64.

[43] Lee S, Daruka I, Kim CS, Barabási AL, Merz JL, Furdyna JK. Dynamics of ripening of self-assembled II–VI semiconductor quantum dots. Phys Rev Lett 1998;81:3479–82.
[44] Strassburg M, Deniozou T, Hoffmann A, Heitz R, Pohl UW, Bimberg D, et al. Coexistence of planar and three-dimensional quantum dots in CdSe/ZnSe structures. Appl Phys Lett 2000;76:685–7.
[45] Kratzert PR, Puls J, Rabe M, Henneberger F. Growth and magneto-optical properties of sub 10 nm (Cd, Mn)Se quantum dots. Appl Phys Lett 2001;79:2814–6.
[46] Bajracharya P, Nguyen TA, Mackowski S, Smith LM, Wagner HP, Pohl UW, et al. Relaxation dynamics of bimodally distributed CdSe quantum dots. Phys Rev B 2007;75:035321.
[47] Guha S, Madhukar A, Rajkumar KC. Onset of incoherency and defect introduction in the initial stages of molecular beam epitaxical growth of highly strained InxGa1-xAs on GaAs(100). Appl Phys Lett 1990;57:2110–2.
[48] Ebiko Y, Muto S, Suzuki D, Itoh S, Shiramine K, Haga T, et al. Island size scaling in InAs/GaAs self-assembled quantum dots. Phys Rev Lett 1998;80:2650–3.
[49] Ebiko Y, Muto S, Suzuki D, Itoh S, Yamakoshi H, Shiramine K, et al. Scaling properties of InAs/GaAs self-assembled quantum dots. Phys Rev B 1999;60:8234–7.
[50] Nakata Y, Mukai K, Sugawara M, Ohtsubo K, Ishikawa H, Yokoyama N. Molecular beam epitaxial growth of InAs self-assembled quantum dots with light-emission at 1.3 μm. J Cryst Growth 2000;208:93–9.
[51] Márquez J, Geelhaar L, Jacobi K. Atomically resolved structure of InAs quantum dots. Appl Phys Lett 2001;78:2309–11.
[52] Krzyzewski TJ, Joyce PB, Bell GR, Jones TS. Wetting layer evolution in InAs/GaAs(001) heteroepitaxy: effects of surface reconstruction and strain. Surf Sci 2002;517:8–16.
[53] Migliorato MA, Cullis AG, Fearn M, Jefferson JH. Atomistic simulation of strain relaxation in InxGa1–xAs/GaAs quantum dots with nonuniform composition. Phys Rev B 2002;65:115316.
[54] Wasserman D, Lyon SA, Hadjipanayi M, Maciel A, Ryan JF. Formation of self-assembled InAs quantum dots on (110) GaAs substrates. Appl Phys Lett 2003;83:5050–2.
[55] Bauer J, Schuh D, Uccelli E, Schulz R, Kress A, Hofbauer F, et al. Long-range ordered self-assembled InAs quantum dots epitaxially grown on (110) GaAs. Appl Phys Lett 2004;85:4750–2.
[56] Akiyama Y, Sakaki H. Formation of self-assembled InGaAs quantum dot arrays aligned along quasiperiodic multiatomic steps on vicinal (111)B GaAs. Appl Phys Lett 2006:89.
[57] Snyder CW, Orr BG, Kessler D, Sander LM. Effect of strain on surface morphology in highly strained InGaAs films. Phys Rev Lett 1991;66:3032–5.
[58] Schmidbauer M, Hatami F, Hanke M, Schafer P, Braune K, Masselink WT, et al. Shape-mediated anisotropic strain in self-assembled InP/In0.48Ga0.52P quantum dots. Phys Rev B 2002;65:125320.
[59] Ugur A, Hatami F, Schmidbauer M, Hanke M, Masselink WT. Self-assembled chains of single layer InP/(In,Ga)P quantum dots on GaAs(001). J Appl Phys 2009;105:124308.
[60] Ugur A, Hatami F, Masselink WT. Controlled growth of InP/In0.48Ga0.52P quantum dots on GaAs substrate. J Cryst Growth 2011;323:228–32.
[61] Pistol ME. InP quantum dots in GaInP. J Phys: Condens Matter 2004;16:S3737–48.
[62] Eaglesham DJ, Cerullo M. Dislocation-free Stranski–Krastanow growth of Ge on Si(100). Phys Rev Lett 1990;64:1943–6.
[63] Mo YW, Savage DE, Swartzentruber BS, Lagally MG. Kinetic pathway in Stranski–Krastanov growth of Ge on Si(001). Phys Rev Lett 1990;65:1020–3.
[64] Abstreiter G, Schittenhelm P, Engel C, Silveira E, Zrenner A, Meertens D, et al. Growth and characterization of self-assembled Ge-rich islands on Si. Semicond Sci Technol 1996;11:1521–8.
[65] Shiryaev SY, Jensen F, Hansen JL, Petersen JW, Larsen AN. Nanoscale structuring by misfit dislocations in Si1–xGex/Si: epitaxial systems. Phys Rev Lett 1997;78:503–6.
[66] Medeiros-Ribeiro G, Bratkovski AM, Kamins TI, Ohlberg DAA, Williams RS. Shape transition of germanium nanocrystals on a silicon (001) surface from pyramids to domes. Science 1998;279:353–5.
[67] Ross FM, Tersoff J, Tromp RM. Coarsening of self-assembled Ge quantum dots on Si(001). Phys Rev Lett 1998;80:984–7.
[68] Floro JA, Lucadamo GA, Chason E, Freund LB, Sinclair M, Twesten RD, et al. SiGe island shape transitions induced by elastic repulsion. Phys Rev Lett 1998;80:4717–20.
[69] Kamins TI, Medeiros-Ribeiro G, Ohlberg DAA, Williams RS. Evolution of Ge islands on Si(001) during annealing. J Appl Phys 1999;85:1159–71.
[70] Floro JA, Chason E, Freund LB, Twesten RD, Hwang RQ, Lucadamo GA. Evolution of coherent islands in Si1–xGex/Si(001). Phys Rev B 1999;59:1990–8.
[71] Vailionis A, Cho B, Glass G, Desjardins P, Cahill DG, Greene JE. Pathway for the strain-driven two-dimensional to three-dimensional transition during growth of Ge on Si(001). Phys Rev Lett 2000;85:3672–5.
[72] Liu CP, Gibson JM, Cahill DG, Kamins TI, Basile DP, Williams RS. Strain evolution in coherent Ge/Si islands. Phys Rev Lett 2000;84:1958–61.
[73] Chaparro SA, Zhang Y, Drucker J, Chandrasekhar D, Smith DJ. Evolution of Ge/Si(100) islands: Island size and temperature dependence. J Appl Phys 2000;87:2245–54.
[74] Tersoff J, Spencer BJ, Rastelli A, von Kanel H. Barrierless formation and faceting of SiGe islands on Si(001). Phys Rev Lett 2002:89.
[75] Yang B, Liu F, Lagally MG. Local strain-mediated chemical potential control of quantum dot self-organization in heteroepitaxy. Phys Rev Lett 2004:92.
[76] Fafard S, Hinzer K, Raymond S, Dion M, McCaffrey J, Feng Y, et al. Red-emitting semiconductor quantum dot lasers. Science 1996;274:1350–3.
[77] Tatebayashi J, Nishioka M, Arakawa Y. Over 1.5 mu m light emission from InAs quantum dots embedded in InGaAs strain-reducing layer grown by metalorganic chemical vapor deposition. Appl Phys Lett 2001;78:3469–71.
[78] Orlov AO, Amlani I, Bernstein GH, Lent CS, Snider GL. Realization of a functional cell for quantum-dot cellular automata. Science 1997;277:928–30.
[79] Imre A, Csaba G, Ji L, Orlov A, Bernstein GH, Porod W. Majority logic gate for magnetic quantum-dot cellular automata. Science 2006;311:205–8.

[80] Yuan MY, Pan F, Yang Z, Gilheart TJ, Chen F, Savage DE, et al. Si/SiGe quantum dot with superconducting single-electron transistor charge sensor. Appl Phys Lett 2011;98:142104.
[81] Wolf CR, Thonke K, Sauer R. Single-electron transistors based on self-assembled silicon-on-insulator quantum dots. Appl Phys Lett 2010;96:142108.
[82] Loss D, DiVincenzo DP. Quantum computation with quantum dots. Phys Rev A 1998;57:120–6.
[83] Hu XD, Das Sarma S. Hilbert-space structure of a solid-state quantum computer: two-electron states of a double-quantum-dot artificial molecule. Phys Rev A 2000;61:062301.
[84] Nitzsche B, Ruhnow F, Diez S. Quantum-dot-assisted characterization of microtubule rotations during cargo transport. Nat Nano 2008;3:552–6.
[85] Bandyopadhyay S, Karahaliloglu K, Balkir S, Pramanik S. Computational paradigm for nanoelectronics: self-assembled quantum dot cellular neural networks. IEE P-circ Dev Syst 2005;152:85–92.
[86] Recher P, Sukhorukov EV, Loss D. Quantum dot as spin filter and spin memory. Phys Rev Lett 2000;85:1962–5.
[87] Kroutvar M, Ducommun Y, Heiss D, Bichler M, Schuh D, Abstreiter G, et al. Optically programmable electron spin memory using semiconductor quantum dots. Nature 2004;432:81–4.
[88] Stroscio JA, Pierce DT, Dragoset RA. Homoepitaxial growth of iron and a real space view of reflection-high-energy-electron diffraction. Phys Rev Lett 1993;70:3615–8.
[89] Zhang ZY, Lagally MG. Atomistic processes in the early stages of thin-film growth. Science 1997;276:377–83.
[90] Brune H. Microscopic view of epitaxial metal growth: nucleation and aggregation. Surf Sci Rep 1998;31:121–229.
[91] Bauer E. Phänomenologische theorie der kristallabscheidung an oberflächen. I Z Kristallogr 1958;110:372.
[92] Frank FC, Merwe JHvd. One-dimensional dislocations. I. Static theory. Proc Roy Soc Lond Ser A: Math Phys Sci 1949;198:205–16.
[93] Volmer M, Weber A. Nucleus formation in supersaturated systems. Z Phys Chem (Munich) 1926;119:277.
[94] Young T. An essay on the cohesion of fluids. Philos Trans Roy Soc Lond 1805;95:65–87.
[95] Sutter P, Lagally MG. Nucleationless three-dimensional island formation in low-misfit heteroepitaxy. Phys Rev Lett 2000;84:4637–40.
[96] Tromp RM, Ross FM, Reuter MC. Instability-driven SiGe island growth. Phys Rev Lett 2000;84:4641–4.
[97] Tersoff J, Tromp RM. Shape transition in growth of strained islands: Spontaneous formation of quantum wires. Phys Rev Lett 1993;70:2782–5.
[98] Priester C, Lannoo M. Origin of self-assembled quantum dots in highly mismatched heteroepitaxy. Phys Rev Lett 1995;75:93–6.
[99] Wang LG, Kratzer P, Scheffler M, Moll N. Formation and stability of self-assembled coherent islands in highly mismatched heteroepitaxy. Phys Rev Lett 1999;82:4042–5.
[100] Lu G-H, Liu F. Towards quantitative understanding of formation and stability of Ge hut islands on Si(001). Phys Rev Lett 2005;94:176103.
[101] Combe N, Jensen P, Barrat J-L. Stable unidimensional arrays of coherent strained islands. Surf Sci 2001;490:351–60.
[102] Walther T, Cullis AG, Norris DJ, Hopkinson M. Nature of the Stranski–Krastanow transition during epitaxy of InGaAs on GaAs. Phys Rev Lett 2001;86:2381–4.
[103] Cullis AG, Norris DJ, Walther T, Migliorato MA, Hopkinson M. Stranski–Krastanow transition and epitaxial island growth. Phys Rev B 2002;66:081305.
[104] Tersoff J, LeGoues FK. Competing relaxation mechanisms in strained layers. Phys Rev Lett 1994;72:3570–3.
[105] Karl B. Si/Ge nanostructures. Rep Prog Phys 2002;65:27.
[106] Spencer BJ, Voorhees PW, Davis SH. Morphological instability in epitaxially strained dislocation-free solid films. Phys Rev Lett 1991;67:3696–9.
[107] Spencer BJ, Voorhees PW, Davis SH. Morphological instability in epitaxially strained dislocation-free solid films: linear stability theory. J Appl Phys 1993;73:4955–70.
[108] Jesson DE, Kästner M, Voigtländer B. Direct observation of subcritical fluctuations during the formation of strained semiconductor islands. Phys Rev Lett 2000;84:330–3.
[109] Steinfort AJ, Scholte PMLO, Ettema A, Tuinstra F, Nielsen M, Landemark E, et al. Strain in nanoscale germanium hut clusters on Si(001) studied by X-Ray diffraction. Phys Rev Lett 1996;77:2009–12.
[110] Kästner M, Voigtländer B. Kinetically self-limiting growth of Ge islands on Si(001). Phys Rev Lett 1999;82:2745–8.
[111] Li XL, Cao YY, Yang GW. Thermodynamic theory of two-dimensional to three-dimensional growth transition in quantum dots self-assembly. Phys Chem Chem Phys 2010;12:4768–72.
[112] Müller P, Thomas O. Asymptotic behaviour of stress establishment in thin films. Surf Sci 2000;465:L764–70.
[113] Nenow D, Trayanov A. Thermodynamics of crystal surfaces with quasi-liquid layer. J Cryst Growth 1986;79:801–5.
[114] Li XL. The influence of the atomic interactions in out-of-plane on surface energy and its applications in nanostructures. J Appl Phys 2012;112:013524.
[115] Dash JG. Surface melting. Contemp Phys 1989;30:89.
[116] Lu G-H, Cuma M, Liu F. First-principles study of strain stabilization of Ge(105) facet on Si(001). Phys Rev B 2005;72:125415.
[117] Shchukin VA, Bimberg D, Munt TP, Jesson DE. Elastic interaction and self-relaxation energies of coherently strained conical islands. Phys Rev B 2004;70:085416.
[118] Li XL, Yang GW. Strain self-releasing mechanism in heteroepitaxy on nanowires. J Phys Chem C 2009;113:12402–6.
[119] Kamins TI, Carr EC, Williams RS, Rosner SJ. Deposition of three-dimensional Ge islands on Si(001) by chemical vapor deposition at atmospheric and reduced pressures. J Appl Phys 1997;81:211–9.
[120] Costantini G, Rastelli A, Manzano C, Acosta-Diaz P, Katsaros G, Songmuang R, et al. Pyramids and domes in the InAs/GaAs(001) and Ge/Si(001) systems. J Cryst Growth 2005;278:38–45.
[121] Polimeni A, Patanè A, Capizzi M, Martelli F, Nasi L, Salviati G. Self-aggregation of quantum dots for very thin InAs layers grown on GaAs. Phys Rev B 1996;53:R4213–6.
[122] Berti M, Drigo AV, Rossetto G, Torzo G. Experimental evidence of two-dimensional-three-dimensional transition in the Stranski–Krastanow coherent growth. J Vac Sci Technol B 1997;15:1794–9.

[123] Heitz R, Ramachandran TR, Kalburge A, Xie Q, Mukhametzhanov I, Chen P, et al. Observation of reentrant 2D to 3D morphology transition in highly strained epitaxy: InAs on GaAs. Phys Rev Lett 1997;78:4071–4.
[124] Ramachandran TR, Heitz R, Chen P, Madhukar A. Mass transfer in Stranski–Krastanow growth of InAs on GaAs. Appl Phys Lett 1997;70:640–2.
[125] Bottomley DJ. The physical origin of InAs quantum dots on GaAs(001). Appl Phys Lett 1998;72:783–5.
[126] Li XL. Thermodynamic analysis on the stability and evolution mechanism of self-assembled quantum dots. Appl Surf Sci 2010;256:4023–6.
[127] Lobanov DN, Novikov AV, Vostokov NV, Drozdov YN, Yablonskiy AN, Krasilnik ZF, et al. Growth and photoluminescence of self-assembled islands obtained during the deposition of Ge on a strained SiGe layer. Opt Mater 2005;27:818–21.
[128] Yurasov DV, Drozdov YN, Shaleev MV, Novikov AV. Features of two-dimensional to three-dimensional growth mode transition of Ge in SiGe/Si(001) heterostructures with strained layers. Appl Phys Lett 2009;95:151902.
[129] Medeiros-Ribeiro G, Kamins TI, Ohlberg DAA, Williams RS. Annealing of Ge nanocrystals on Si(001) at 550 C: metastability of huts and the stability of pyramids and domes. Phys Rev B 1998;58:3533–6.
[130] Tonkikh AA, Dubrovskii VG, Cirlin GE, Egorov VA, Ustinov VM, Werner P. Temperature dependence of the quantum dot lateral size in the Ge/Si(100) system. Phys Status Solidi (b) 2003;236:R1–3.
[131] Ross FM, Tromp RM, Reuter MC. Transition states between pyramids and domes during Ge/Si island growth. Science 1999;286:1931–4.
[132] Rastelli A, von Känel H. Surface evolution of faceted islands. Surf Sci 2002;515:L493–8.
[133] Montalenti F, Raiteri P, Migas DB, von Känel H, Rastelli A, Manzano C, et al. Atomic-scale pathway of the pyramid-to-dome transition during Ge growth on Si(001). Phys Rev Lett 2004;93:216102.
[134] Rastelli A, Kummer M, von Känel H. Reversible shape evolution of Ge islands on Si(001). Phys Rev Lett 2001;87:256101.
[135] Capellini G, De Seta M, Evangelisti F, Zinovyev VA, Vastola G, Montalenti F, et al. Self-ordering of a Ge island single layer induced by Si overgrowth. Phys Rev Lett 2006;96:106102.
[136] Lang C, Kodambaka S, Ross FM, Cockayne DJH. Real time observation of GeSi/Si(001) island shrinkage due to surface alloying during Si capping. Phys Rev Lett 2006;97:226104.
[137] Daruka I, Barabási A-L. Dislocation-free island formation in heteroepitaxial growth: a study at equilibrium. Phys Rev Lett 1997;79:3708–11.
[138] Daruka I, Tersoff J, Barabási AL. Shape transition in growth of strained islands. Phys Rev Lett 1999;82:2753–6.
[139] Rudd RE, Briggs GAD, Sutton AP, Medeiros-Ribeiro G, Williams RS. Equilibrium model of bimodal distributions of epitaxial island growth. Phys Rev Lett 2003;90:146101.
[140] Chen KM, Jesson DE, Pennycook SJ, Thundat T, Warmack RJ. Critical nuclei shapes in the stress-driven 2D-to-3D transition. Phys Rev B 1997;56:R1700–3.
[141] Poon TW, Yip S, Ho PS, Abraham FF. Equilibrium structures of Si(100) stepped surfaces. Phys Rev Lett 1990;65:2161–4.
[142] Perdew JP, Wang Y, Engel E. Liquid-drop model for crystalline metals: vacancy-formation, cohesive, and face-dependent surface energies. Phys Rev Lett 1991;66:508–11.
[143] Schmidt OG, Eberl K. Self-assembled Ge/Si dots for faster field-effect transistors. Electron Dev IEEE Trans 2001;48:1175–9.
[144] Sutter P, Lagally MG. Embedding of nanoscale 3D SiGe islands in a Si matrix. Phys Rev Lett 1998;81:3471–4.
[145] Zhong Z, Stangl J, Schäffler F, Bauer G. Evolution of shape, height, and in-plane lattice constant of Ge-rich islands during capping with Si. Appl Phys Lett 2003;83:3695–7.
[146] Wu YQ, Li FH, Cui J, Lin JH, Wu R, Qin J, et al. Shape change of SiGe islands with initial Si capping. Appl Phys Lett 2005;87:223116.
[147] Blossey R, Lorke A. Wetting droplet instability and quantum ring formation. Phys Rev E 2002;65:021603.
[148] Granados D, García JM. In(Ga)As self-assembled quantum ring formation by molecular beam epitaxy. Appl Phys Lett 2003;82:2401–3.
[149] Costantini G, Rastelli A, Manzano C, Acosta-Diaz P, Songmuang R, Katsaros G, et al. Interplay between thermodynamics and kinetics in the capping of InAs/GaAs(001) quantum dots. Phys Rev Lett 2006;96:226106.
[150] Li XL, Yang GW. Thermodynamic theory of shape evolution induced by Si capping in Ge quantum dot self-assembly. J Appl Phys 2009;105:013510.
[151] Lang C, Cockayne DJH, Nguyen-Manh D. Alloyed Ge(Si)/Si(001) islands: the composition profile and the shape transformation. Phys Rev B 2005;72:155328.
[152] Rastelli A, von Känel H, Albini G, Raiteri P, Migas DB, Miglio L. Morphological and compositional evolution of the Ge/Si(001) surface during exposure to a Si flux. Phys Rev Lett 2003;90:216104.
[153] Nakagawa K, Miyao M. Reverse temperature dependence of Ge surface segregation during Si-molecular beam epitaxy. J Appl Phys 1991;69:3058–62.
[154] Zhong Z, Halilovic A, Mühlberger M, Schäffler F, Bauer G. Ge island formation on stripe-patterned Si(001) substrates. Appl Phys Lett 2003;82:445–7.
[155] Karmous A, Cuenat A, Ronda A, Berbezier I, Atha S, Hull R. Ge dot organization on Si substrates patterned by focused ion beam. Appl Phys Lett 2004;85:6401–3.
[156] Bavard A, Eymery J, Pascale A, Fournel F. Controlled Ge quantum dots positioning with nano-patterned Si(001) substrates. Phys Status Solidi (b) 2006;243:3963–7.
[157] Zhong Z, Halilovic A, Mühlberger M, Schäffler F, Bauer G. Positioning of self-assembled Ge islands on stripe-patterned Si(001) substrates. J Appl Phys 2003;93:6258–64.
[158] Yang B, Liu F, Lagally MG. Local strain-mediated chemical potential control of quantum dot self-organization in heteroepitaxy. Phys Rev Lett 2004;92:025502.
[159] Kamins TI, Williams RS. Lithographic positioning of self-assembled Ge islands on Si(001). Appl Phys Lett 1997;71:1201–3.
[160] Jin G, Liu JL, Wang KL. Regimented placement of self-assembled Ge dots on selectively grown Si mesas. Appl Phys Lett 2000;76:3591–3.

[161] Kim ES, Usami N, Shiraki Y. Control of Ge dots in dimension and position by selective epitaxial growth and their optical properties. Appl Phys Lett 1998;72:1617–9.
[162] Schmidt OG, Jin-Phillipp NY, Lange C, Denker U, Eberl K, Schreiner R, et al. Long-range ordered lines of self-assembled Ge islands on a flat Si(001) surface. Appl Phys Lett 2000;77:4139–41.
[163] Vescan L, Stoica T. Luminescence of laterally ordered Ge islands along ⟨100⟩ directions. J Appl Phys 2002;91:10119–26.
[164] Zhong Z, Halilovic A, Fromherz T, Schäffler F, Bauer G. Two-dimensional periodic positioning of self-assembled Ge islands on prepatterned Si(001) substrates. Appl Phys Lett 2003;82:4779–81.
[165] Borgström M, Zela V, Seifert W. Arrays of Ge islands on Si(001) grown by means of electron-beam pre-patterning. Nanotechnology 2003;14:264.
[166] Zhong Z, Bauer G. Site-controlled and size-homogeneous Ge islands on prepatterned Si(001) substrates. Appl Phys Lett 2004;84:1922–4.
[167] Lee H, Johnson JA, He MY, Speck JS, Petroff PM. Strain-engineered self-assembled semiconductor quantum dot lattices. Appl Phys Lett 2001;78:105–7.
[168] Cui CX, Chen YH, Ren YY, Xu B, Jin P, Zhao C, et al. Selective growth of InAs islands on patterned GaAs(100) substrate. Superlatt Microstruct 2006;39:446–53.
[169] Schramboeck M, Schrenk W, Roch T, Andrews AM, Austerer M, Strasser G. Self organized InAs quantum dots grown on patterned GaAs substrates. Microelectron Eng 2006;83:1573–6.
[170] Kiravittaya S, Heidemeyer H, Schmidt OG. Lateral quantum-dot replication in three-dimensional quantum-dot crystals. Appl Phys Lett 2005;86:263113.
[171] Ma WQ, Sun YW, Yang XJ, Jiang DS, Chen LH. Self-organized hexagonal ordering of quantum dot arrays. Nanotechnology 2006;17:5765.
[172] Richard N. Self-organized growth of quantum-dot structures. Semicond Sci Technol 1996;11:1365.
[173] Konkar A, Madhukar A, Chen P. Stress-engineered spatially selective self-assembly of strained InAs quantum dots on nonplanar patterned GaAs(001) substrates. Appl Phys Lett 1998;72:220–2.
[174] Lee H, Johnson JA, Speck JS, Petroff PM. Controlled ordering and positioning of InAs self-assembled quantum dots. J Vac Sci Technol B 2000;18:2193–6.
[175] Heidemeyer H, Denker U, Müller C, Schmidt OG. Morphology response to strain field interferences in stacks of highly ordered quantum dot arrays. Phys Rev Lett 2003;91:196103.
[176] Schmidt OG, Kiravittaya S, Nakamura Y, Heidemeyer H, Songmuang R, Müller C, et al. Self-assembled semiconductor nanostructures: climbing up the ladder of order. Surf Sci 2002;514:10–8.
[177] Zhong Z, Schwinger W, Schäffler F, Bauer G, Vastola G, Montalenti F, et al. Delayed plastic relaxation on patterned Si substrates: coherent SiGe pyramids with dominant 111 facets. Phys Rev Lett 2007;98:176102.
[178] Bollani M, Chrastina D, Fedorov A, Sordan R, Picco A, Bonera E. Ge-rich islands grown on patterned Si substrates by low-energy plasma-enhanced chemical vapour deposition. Nanotechnology 2010;21:475302.
[179] Hu H, Gao H, Liu F. Quantitative model of heterogeneous nucleation and growth of SiGe quantum dot molecules. Phys Rev Lett 2012;109:106103.
[180] Hu H, Gao HJ, Liu F. Theory of directed nucleation of strained islands on patterned substrates. Phys Rev Lett 2008;101:216102.
[181] Bavencoffe M, Houdart E, Priester C. Strained heteroepitaxy on nanomesas: a way toward perfect lateral organization of quantum dots. J Cryst Growth 2005;275:305–16.
[182] Pascale A, Berbezier I, Ronda A, Kelires PC. Self-assembly and ordering mechanisms of Ge islands on prepatterned Si(001). Phys Rev B 2008;77:075311.
[183] Nurminen L, Kuronen A, Kaski K. Kinetic Monte Carlo simulation of nucleation on patterned substrates. Phys Rev B 2000;63:035407.
[184] Bergamaschini R, Montalenti F, Miglio L. Optimal growth conditions for selective Ge islands positioning on Pit-patterned Si(001). Nanoscale Res Lett 2010;5:1873–7.
[185] Mullins WW. Theory of thermal grooving. J Appl Phys 1957;28:333–9.
[186] Yang GW, Liu BX. Nucleation thermodynamics of quantum-dot formation in V-groove structures. Phys Rev B 2000;61:4500–2.
[187] Gherasimova M, Hull R, Reuter MC, Ross FM. Pattern level assembly of Ge quantum dots on Si with focused ion beam templating. Appl Phys Lett 2008;93:023106.
[188] Portavoce A, Kammler M, Hull R, Reuter MC, Ross FM. Mechanism of the nanoscale localization of Ge quantum dot nucleation on focused ion beam templated Si(001) surfaces. Nanotechnology 2006;17:4451.
[189] Atkinson P, Bremner SP, Anderson D, Jones GAC, Ritchie DA. Size evolution of site-controlled InAs quantum dots grown by molecular beam epitaxy on prepatterned GaAs substrates. J Vac Sci Technol B 2006;24:1523–6.
[190] Martín-Sánchez J, González Y, González L, Tello M, García R, Granados D, et al. Ordered InAs quantum dots on pre-patterned GaAs(001) by local oxidation nanolithography. J Cryst Growth 2005;284:313–8.
[191] Kiravittaya S, Heidemeyer H, Schmidt OG. Growth of three-dimensional quantum dot crystals on patterned GaAs(001) substrates. Physica E 2004;23:253–9.
[192] Songmuang R, Kiravittaya S, Schmidt OG. Formation of lateral quantum dot molecules around self-assembled nanoholes. Appl Phys Lett 2003;82:2892–4.
[193] Krause B, Metzger TH, Rastelli A, Songmuang R, Kiravittaya S, Schmidt OG. Shape, strain, and ordering of lateral InAs quantum dot molecules. Phys Rev B 2005;72:085339.
[194] Wang L, Rastelli A, Kiravittaya S, Atkinson P, Ding F, Bufon CCB, et al. Towards deterministically controlled InGaAs/GaAs lateral quantum dot molecules. New J Phys 2008;10:045010.
[195] Tersoff J, Spencer BJ, Rastelli A, von Känel H. Barrierless formation and faceting of SiGe islands on Si(001). Phys Rev Lett 2002;89:196104.
[196] Xie Q, Madhukar A, Chen P, Kobayashi NP. Vertically self-organized InAs quantum box islands on GaAs(100). Phys Rev Lett 1995;75:2542–5.

[197] Mateeva E, Sutter P, Bean JC, Lagally MG. Mechanism of organization of three-dimensional islands in SiGe/Si multilayers. Appl Phys Lett 1997;71:3233–5.
[198] Schmidt OG, Kienzle O, Hao Y, Eberl K, Ernst F. Modified Stranski–Krastanov growth in stacked layers of self-assembled islands. Appl Phys Lett 1999;74:1272–4.
[199] Le Thanh V, Yam V, Boucaud P, Fortuna F, Ulysse C, Bouchier D, et al. Vertically self-organized Ge/Si(001) quantum dots in multilayer structures. Phys Rev B 1999;60:5851–7.
[200] Usami N, Araki Y, Ito Y, Miura M, Shiraki Y. Modification of the growth mode of Ge on Si by buried Ge islands. Appl Phys Lett 2000;76:3723–5.
[201] Schmidt OG, Eberl K. Multiple layers of self-asssembled Ge/Si islands: photoluminescence, strain fields, material interdiffusion, and island formation. Phys Rev B 2000;61:13721–9.
[202] Pal D, Towe E, Chen S. Structural characterization of InAs/GaAs quantum-dot nanostructures. Appl Phys Lett 2001;78:4133–5.
[203] Capellini G, De Seta M, Spinella C, Evangelisti F. Ordering self-assembled islands without substrate patterning. Appl Phys Lett 2003;82:1772–4.
[204] De Seta M, Capellini G, Evangelisti F. Ordered growth of Ge island clusters on strain-engineered Si surfaces. Phys Rev B 2005;71:115308.
[205] Dunbar A, Halsall M, Dawson P, Bangert U, Miura M, Shiraki Y. The effect of strain field seeding on the epitaxial growth of Ge islands on Si(001). Appl Phys Lett 2001;78:1658–60.
[206] Tersoff J, Teichert C, Lagally MG. Self-organization in growth of quantum dot superlattices. Phys Rev Lett 1996;76:1675–8.
[207] Zhang J, Zhang K, Zhong J. Local self-organization of islands in embedded nanodot systems. Appl Phys Lett 2004;84:1853–5.
[208] Zhang J, Zhang K, Zhong J. Replication and alignment of quantum dots in multilayer heteroepitaxial growth. Surf Sci 2004;551:L40–6.
[209] Makeev MA, Madhukar A. Simulations of atomic level stresses in systems of buried Ge/Si islands. Phys Rev Lett 2001;86:5542–5.
[210] Priester C. Modified two-dimensional to three-dimensional growth transition process in multistacked self-organized quantum dots. Phys Rev B 2001;63:153303.
[211] Marchetti R, Montalenti F, Miglio L, Capellini G, De Seta M, Evangelisti F. Strain-induced ordering of small Ge islands in clusters at the surface of multilayered Si–Ge nanostructures. Appl Phys Lett 2005;87:261919.
[212] Liu F, Davenport SE, Evans HM, Lagally MG. Self-organized replication of 3D coherent island size and shape in multilayer heteroepitaxial films. Phys Rev Lett 1999;82:2528–31.
[213] Lam P-M, Tan S. Kinetic monte carlo model of self-organized quantum dot superlattices. Phys Rev B 2001;64:035321.
[214] Zhang YW, Xu SJ, Chiu C-h. Vertical self-alignment of quantum dots in superlattice. Appl Phys Lett 1999;74:1809–11.
[215] Daruka I, Barabási AL, Zhou SJ, Germann TC, Lomdahl PS, Bishop AR. Molecular-dynamics investigation of the surface stress distribution in a Ge/Si quantum dot superlattice. Phys Rev B 1999;60:R2150–3.
[216] Makeev MA, Madhukar A. Calculation of vertical correlation probability in Ge/Si(001) shallow island quantum dot multilayer systems. Nano Lett 2006;6:1279–83.
[217] Li XL. Surface chemical potential in multilayered Stranski–Krastanow systems: an analytic study and anticipated applications. J Appl Phys 2009;106:113520.
[218] Li XL, Ouyang G, Tan X. Thermodynamic stability of quantum dots on strained substrates. Physica E 2011;43:1755–8.
[219] Hu SM. Stress from a parallelepipedic thermal inclusion in a semispace. J Appl Phys 1989;66:2741–3.
[220] Tan X, Li XL, Yang GW. Theoretical strategy for self-assembly of quantum rings. Phys Rev B 2008;77:245322.
[221] Cao YY, Li XL, Yang GW. Wetting layer evolution upon quantum dots self-assembly. Appl Phys Lett 2009;95:231902.
[222] Rosenauer A, Fischer U, Gerthsen D, Förster A. Composition evaluation of InxGa1–xAs Stranski–Krastanow-island structures by strain state analysis. Appl Phys Lett 1997;71:3868–70.
[223] Liao XZ, Zou J, Cockayne DJH, Leon R, Lobo C. Indium segregation and enrichment in coherent InxGa1–xAs/GaAs quantum dots. Phys Rev Lett 1999;82:5148–51.
[224] Nakajima K, Konishi A, Kimura K. Direct observation of intermixing at Ge/Si(001) interfaces by high-resolution rutherford backscattering spectroscopy. Phys Rev Lett 1999;83:1802–5.
[225] Joyce PB, Krzyzewski TJ, Bell GR, Jones TS, Malik S, Childs D, et al. Effect of growth rate on the size, composition, and optical properties of InAs/GaAs quantum dots grown by molecular-beam epitaxy. Phys Rev B 2000;62:10891–5.
[226] Chaparro SA, Drucker J, Zhang Y, Chandrasekhar D, McCartney MR, Smith DJ. Strain-driven alloying in Ge/Si(100) coherent islands. Phys Rev Lett 1999;83:1199–202.
[227] Liao XZ, Zou J, Cockayne DJH, Wan J, Jiang ZM, Jin G, et al. Alloying, elemental enrichment, and interdiffusion during the growth of Ge(Si)/Si(001) quantum dots. Phys Rev B 2002;65:153306.
[228] Magalhães-Paniago R, Medeiros-Ribeiro G, Malachias A, Kycia S, Kamins TI, Williams RS. Direct evaluation of composition profile, strain relaxation, and elastic energy of Ge:Si(001) self-assembled islands by anomalous x-ray scattering. Phys Rev B 2002;66:245312.
[229] Kegel I, Metzger TH, Lorke A, Peisl J, Stangl J, Bauer G, et al. Nanometer-scale resolution of strain and interdiffusion in self-assembled InAs/GaAs quantum dots. Phys Rev Lett 2000;85:1694–7.
[230] Malachias A, Kycia S, Medeiros-Ribeiro G, Magalhães-Paniago R, Kamins TI, Williams RS. 3D composition of epitaxial nanocrystals by anomalous X-ray diffraction: observation of a Si-rich core in Ge domes on Si(100). Phys Rev Lett 2003;91:176101.
[231] Zanotto S, Degl'Innocenti R, Sorba L, Tredicucci A, Biasiol G. Analysis of line shapes and strong coupling with intersubband transitions in one-dimensional metallodielectric photonic crystal slabs. Phys Rev B 2012;85:035307.
[232] Malachias A, Schülli TU, Medeiros-Ribeiro G, Cançado LG, Stoffel M, Schmidt OG, et al. X-ray study of atomic ordering in self-assembled Ge islands grown on Si(001). Phys Rev B 2005;72:165315.
[233] Leite MS, Malachias A, Kycia SW, Kamins TI, Williams RS, Medeiros-Ribeiro G. Evolution of thermodynamic potentials in closed and open nanocrystalline systems: Ge–Si:Si(001) islands. Phys Rev Lett 2008;100:226101.

[234] Biasiol G, Heun S, Golinelli GB, Locatelli A, Mentes TO, Guo FZ, et al. Surface compositional gradients of InAs/GaAs quantum dots. Appl Phys Lett 2005;87:223106.
[235] Müller M, Cerezo A, Smith GDW, Chang L, Gerstl SSA. Atomic scale characterization of buried InxGa1–xAs quantum dots using pulsed laser atom probe tomography. Appl Phys Lett 2008;92:10.
[236] Rastelli A, Stoffel M, Malachias A, Merdzhanova T, Katsaros G, Kern K, et al. Three-dimensional composition profiles of single quantum dots determined by scanning-probe-microscopy-based nanotomography. Nano Lett 2008;8:1404–9.
[237] Medhekar NV, Hegadekatte V, Shenoy VB. Composition maps in self-assembled alloy quantum dots. Phys Rev Lett 2008;100:106104.
[238] Digiuni D, Gatti R, Montalenti F. Aspect-ratio-dependent driving force for nonuniform alloying in Stranski–Krastanow islands. Phys Rev B 2009;80:155436.
[239] Vastola G, Shenoy VB, Guo J, Zhang YW. Coupled evolution of composition and morphology in a faceted three-dimensional quantum dot. Phys Rev B 2011;84:035432.
[240] Liang XD, Ni Y, He LH. Shape-dependent composition profile in epitaxial alloy quantum dots: a phase-field simulation. Comp Mater Sci 2010;48:871–4.
[241] Spencer BJ, Voorhees PW, Tersoff J. Morphological instability theory for strained alloy film growth: the effect of compositional stresses and species-dependent surface mobilities on ripple formation during epitaxial film deposition. Phys Rev B 2001;64:235318.
[242] Hadjisavvas G, Kelires PC. Critical aspects of alloying and stress relaxation in Ge/Si(100) islands. Phys Rev B 2005;72:075334.
[243] Vantarakis G, Remediakis IN, Kelires PC. Ordering mechanisms in epitaxial SiGe nanoislands. Phys Rev Lett 2012;108:176102.
[244] Shenoy VB. Evolution of morphology and composition in three-dimensional fully faceted strained alloy crystals. J Mech Phys Solids 2011;59:1121–30.
[245] Gatti R, Uhlík F, Montalenti F. Intermixing in heteroepitaxial islands: fast, self-consistent calculation of the concentration profile minimizing the elastic energy. New J Phys 2008;10:083039.
[246] Ye H, Lu PF, Yu ZY, Wang DL, Chen ZH, Liu YM, et al. Dislocation-induced composition profile in alloy semiconductors. Solid State Commun 2010;150:1275–8.
[247] Medeiros-Ribeiro G, Williams RS. Thermodynamics of coherently-strained GexSi1-x nanocrystals on Si(001): alloy composition and island formation. Nano Lett 2007;7:223–6.
[248] Schülli TU, Vastola G, Richard MI, Malachias A, Renaud G, Uhlík F, et al. Enhanced relaxation and intermixing in Ge islands grown on pit-patterned Si(001) substrates. Phys Rev Lett 2009;102:025502.
[249] Floro JA, Sinclair MB, Chason E, Freund LB, Twesten RD, Hwang RQ, et al. Novel SiGe island coarsening kinetics: Ostwald ripening and elastic interactions. Phys Rev Lett 2000;84:701–4.
[250] Tu Y, Tersoff J. Origin of apparent critical thickness for island formation in heteroepitaxy. Phys Rev Lett 2004;93:216101.
[251] Tu Y, Tersoff J. Coarsening, mixing, and motion: the complex evolution of epitaxial islands. Phys Rev Lett 2007;98:096103.
[252] Johansson J, Seifert W. Kinetics of self-assembled island formation: Part II–Island size. J Cryst Growth 2002;234:139–44.
[253] Malachias A, Stoffel M, Schmidbauer M, Schulli TÜ, Medeiros-Ribeiro G, Schmidt OG, et al. Atomic ordering dependence on growth method in Ge:Si(001) islands: influence of surface kinetic and thermodynamic interdiffusion mechanisms. Phys Rev B 2010;82:035307.
[254] Katsaros G, Costantini G, Stoffel M, Esteban R, Bittner AM, Rastelli A, et al. Kinetic origin of island intermixing during the growth of Ge on Si(001). Phys Rev B 2005;72:195320.
[255] Xu X, Aqua JN, Frisch T. Growth kinetics in a strained crystal film on a wavy patterned substrate. J Phys: Conden Matter 2012;24:045002.
[256] McKay MR, Venables JA, Drucker J. Kinetically suppressed Ostwald ripening of Ge/Si(100) hut clusters. Phys Rev Lett 2008;101:216104.
[257] Meixner M, Schöll E, Shchukin VA, Bimberg D. Self-assembled quantum dots: crossover from kinetically controlled to thermodynamically limited growth. Phys Rev Lett 2001;87:236101.
[258] Desai RC, Kim H, Chatterji A, Ngai D, Chen S, Yang N. Epitaxial growth in dislocation-free strained asymmetric alloy films. Phys Rev B 2010;81:235301.
[259] Huang Z-F, Desai RC. Epitaxial growth in dislocation-free strained alloy films: morphological and compositional instabilities. Phys Rev B 2002;65:205419.
[260] Spencer BJ, Blanariu M. Shape and composition map of a prepyramid quantum dot. Phys Rev Lett 2005;95:206101.
[261] Denker U, Rastelli A, Stoffel M, Tersoff J, Katsaros G, Costantini G, et al. Lateral motion of SiGe islands driven by surface-mediated alloying. Phys Rev Lett 2005;94:216103.
[262] Katsaros G, Rastelli A, Stoffel M, Isella G, Känel Hv, Bittner AM, et al. Investigating the lateral motion of SiGe islands by selective chemical etching. Surf Sci 2006;600:2608–13.
[263] Niu XB, Stringfellow GB, Liu F. Nonequilibrium composition profiles of alloy quantum dots and their correlation with the growth mode. Phys Rev Lett 2011;107:076101.
[264] Biasiol G, Heun S. Compositional mapping of semiconductor quantum dots and rings. Phys Rep 2011;500:117–73.
[265] Yang N, Dai Z, Zhu J-L. Spin and angular momentum transitions in few-electron quantum dots and rings. Phys Rev B 2008;77:245321.
[266] Bayer M, Korkusinski M, Hawrylak P, Gutbrod T, Michel M, Forchel A. Optical detection of the Aharonov-Bohm effect on a charged particle in a nanoscale quantum ring. Phys Rev Lett 2003;90:186801.
[267] Aharonov Y, Bohm D. Significance of electromagnetic potentials in the quantum theory. Phys Rev 1959;115:485–91.
[268] Keyser UF, Fühner C, Borck S, Haug RJ, Bichler M, Abstreiter G, et al. Kondo effect in a few-electron quantum ring. Phys Rev Lett 2003;90:196601.
[269] McLellan JM, Geissler M, Xia Y. Edge spreading lithography and its application to the fabrication of mesoscopic gold and silver rings. J Am Chem Soc 2004;126:10830–1.
[270] Kosiorek A, Kandulski W, Glaczynska H, Giersig M. Fabrication of nanoscale rings, dots, and rods by combining shadow nanosphere lithography and annealed polystyrene nanosphere masks. Small 2005;1:439–44.

[271] Bochenkov VE, Sutherland DS. From rings to crescents: a novel fabrication technique uncovers the transition details. Nano Lett 2013;13:1216–20.
[272] Hanke M, Mazur YI, Marega E, AbuWaar ZY, Salamo GJ, Schäfer P, et al. Shape transformation during overgrowth of InGaAs/GaAs(001) quantum rings. Appl Phys Lett 2007;91:043103.
[273] Mano T, Koguchi N. Nanometer-scale GaAs ring structure grown by droplet epitaxy. J Cryst Growth 2005;278:108–12.
[274] Gong Z, Niu ZC, Huang SS, Fang ZD, Sun BQ, Xia JB. Formation of GaAs/AlGaAs and InGaAs/GaAs nanorings by droplet molecular-beam epitaxy. Appl Phys Lett 2005;87:093116.
[275] Wang ZMM, Holmes K, Shultz JL, Salamo GJ. Self-assembly of GaAs holed nanostructures by droplet epitaxy. Phys Status Solidi A 2005;202:R85–7.
[276] Lee JH, Zh MW, Abuwaar ZY, Strom NW, Salamo GJ. Evolution between self-assembled single and double ring-like nanostructures. Nanotechnology 2006;17:3973.
[277] Huang S, Niu Z, Fang Z, Ni H, Gong Z, Xia J. Complex quantum ring structures formed by droplet epitaxy. Appl Phys Lett 2006;89:031921.
[278] Mano T, Noda T, Yamagiwa M, Koguchi N. Coupled quantum nanostructures formed by droplet epitaxy. Thin Solid Films 2006;515:531–4.
[279] Tong CZ, Yoon SF. Investigation of the fabrication mechanism of self-assembled GaAs quantum rings grown by droplet epitaxy. Nanotechnology 2008;19:365604.
[280] Li AZ, Wang ZM, Wu J, Xie Y, Sablon KA, Salamo GJ. Evolution of holed nanostructures on GaAs (001). Cryst Growth Des 2009;9:2941–3.
[281] Somaschini C, Bietti S, Koguchi N, Sanguinetti S. Fabrication of multiple concentric nanoring structures. Nano Lett 2009;9:3419–24.
[282] Lee JH, Wang ZM, Ware ME, Wijesundara KC, Garrido M, Stinaff EA, et al. Super Llow density InGaAs semiconductor ring-shaped nanostructures. Cryst Growth Des 2008;8:1945–51.
[283] Mano T, Watanabe K, Tsukamoto S, Fujioka H, Oshima M, Koguchi N. Fabrication of InGaAs quantum dots on GaAs(001) by droplet epitaxy. J Cryst Growth 2000;209:504–8.
[284] Li X, Wu J, Wang ZM, Liang B, Lee J, Kim E-S, et al. Origin of nanohole formation by etching based on droplet epitaxy. Nanoscale 2014;6:2675–81.
[285] Wu J, Shao D, Dorogan VG, Li AZ, Li S, DeCuir EA, et al. Intersublevel infrared photodetector with strain-free GaAs quantum dot pairs grown by high-temperature droplet epitaxy. Nano Lett 2010;10:1512–6.
[286] Wu J, Shao D, Li Z, Manasreh MO, Kunets VP, Wang ZM, et al. Intermediate-band material based on GaAs quantum rings for solar cells. Appl Phys Lett 2009;95:071908.
[287] Wu J, Li ZH, Shao DL, Manasreh MO, Kunets VP, Wang ZMM, et al. Multicolor photodetector based on GaAs quantum rings grown by droplet epitaxy. Appl Phys Lett 2009;94:171102.
[288] Wu J, Wang ZMM, Dorogan VG, Li SB, Lee J, Mazur YI, et al. Effects of rapid thermal annealing on the optical properties of strain-free quantum ring solar cells. Nanoscale Res Lett 2013;8:1–5.
[289] Wu J, Wang Z, Dorogan V, Mazur Y, Li S, Salamo G. Insight into optical properties of strain-free quantum dot pairs. J Nanopart Res 2011;13:947–52.
[290] Heyn C, Stemmann A, Eiselt R, Hansen W. Influence of Ga coverage and As pressure on local droplet etching of nanoholes and quantum rings. J Appl Phys 2009;105:054316.
[291] Heyn C. Kinetic model of local droplet etching. Phys Rev B 2011;83:165302.
[292] Heyn C, Stemmann A, Hansen W. Dynamics of self-assembled droplet etching. Appl Phys Lett 2009;95:173110.
[293] Li XL, Yang GW. On the physical understanding of quantum rings self-assembly upon droplet epitaxy. J Appl Phys 2009;105:103507.
[294] Li XL. Formation mechanisms of multiple concentric nanoring structures upon droplet epitaxy. J Phys Chem C 2010;114:15343–6.
[295] Li XL. Theory of controllable shape of quantum structures upon droplet epitaxy. J Cryst Growth 2013;377:59–63.
[296] Zhou ZY, Zheng CX, Tang WX, Tersoff J, Jesson DE. Origin of quantum ring formation during droplet epitaxy. Phys Rev Lett 2013;111:036102.
[297] Wang CX, Wang B, Yang YH, Yang GW. Thermodynamic and kinetic size limit of nanowire growth. J Phys Chem B 2005;109:9966–9.
[298] Tersoff J, Johnson MD, Orr BG. Adatom densities on GaAs: evidence for near-equilibrium growth. Phys Rev Lett 1997;78:282–5.
[299] Somaschini C, Bietti S, Koguchi N, Sanguinetti S. Coupled quantum dot–ring structures by droplet epitaxy. Nanotechnology 2011;22:185602.
[300] Xia Y, Yang P, Sun Y, Wu Y, Mayers B, Gates B, et al. One-dimensional nanostructures: synthesis, characterization, and applications. Adv Mater 2003;15:353–89.
[301] Zhong Lin W. Zinc oxide nanostructures: growth, properties and applications. J Phys: Condens Matter 2004;16:R829.
[302] Zhang CY, Wang CX, Yang YH, Yang GW. A nanoscaled thermodynamic approach in nucleation of CVD diamond on nondiamond surfaces. J Phys Chem B 2004;108:2589–93.
[303] Wang ZL, Kong XY, Zuo JM. Induced growth of asymmetric nanocantilever arrays on polar surfaces. Phys Rev Lett 2003;91:185502.
[304] Abe S, Rajagopal AK. Validity of the second law in nonextensive quantum thermodynamics. Phys Rev Lett 2003;91:120601.
[305] Chamberlin RV. Critical behavior from Landau theory in nanothermodynamic equilibrium. Phys Lett A 2003;315:313–8.
[306] Chamberlin RV. Mean-field cluster model for the critical behaviour of ferromagnets. Nature 2000;408:337–9.
[307] Pohl K, Bartelt MC, de la Figuera J, Bartelt NC, Hrbek J, Hwang RQ. Identifying the forces responsible for self-organization of nanostructures at crystal surfaces. Nature 1999;397:238–41.
[308] Plass R, Last JA, Bartelt NC, Kellogg GL. Nanostructures: self-assembled domain patterns. Nature 2001;412:875.
[309] Wagner RS, Ellis WC, Jackson KA, Arnold SM. Study of the filamentary growth of silicon crystals from the vapor. J Appl Phys 1964;35:2993–3000.

[310] Wagner RS, Ellis WC. Vapor–liquid–solid mechanism of single crystal growth. Appl Phys Lett 1964;4:89–90.
[311] Morales AM, Lieber CM. A laser ablation method for the synthesis of crystalline semiconductor nanowires. Science 1998;279:208–11.
[312] Duan X, Lieber CM. General synthesis of compound semiconductor nanowires. Adv Mater 2000;12:298–302.
[313] Chen CC, Yeh CC. Large-scale catalytic synthesis of crystalline gallium nitride nanowires. Adv Mater 2000;12:738–41.
[314] Wu Y, Yang P. Germanium nanowire growth via simple vapor transport. Chem Mater 2000;12:605–7.
[315] Wu XC, Song WH, Wang KY, Hu T, Zhao B, Sun YP, et al. Preparation and photoluminescence properties of amorphous silica nanowires. Chem Phys Lett 2001;336:53–6.
[316] Tolbert SH, Alivisatos AP. High-pressure structural transformations in semiconductor nanocrystals. Annu Rev Phys Chem 1995;46:595–626.
[317] Kelton KF. Crystal nucleation in liquids and glasses. In: Henry E, David T, editors. Solid state physics. Academic Press; 1991. p. 75–177.
[318] Lew KK, Pan L, Dickey EC, Redwing JM. Vapor–liquid–solid growth of silicon–germanium nanowires. Adv Mater 2003;15:2073–6.
[319] Cui Y, Lauhon LJ, Gudiksen MS, Wang J, Lieber CM. Diameter-controlled synthesis of single-crystal silicon nanowires. Appl Phys Lett 2001;78:2214–6.
[320] Louchev OA, Sato Y, Kanda H. Growth mechanism of carbon nanotube forests by chemical vapor deposition. Appl Phys Lett 2002;80:2752–4.
[321] Tan TY, Li N, Gösele U. Is there a thermodynamic size limit of nanowires grown by the vapor–liquid–solid process? Appl Phys Lett 2003;83:1199–201.
[322] Wang N, Tang YH, Zhang YF, Yu DP, Lee CS, Bello I, et al. Transmission electron microscopy evidence of the defect structure in Si nanowires synthesized by laser ablation. Chem Phys Lett 1998;283:368–72.
[323] Wang N, Tang YH, Zhang YF, Lee CS, Bello I, Lee ST. Si nanowires grown from silicon oxide. Chem Phys Lett 1999;299:237–42.
[324] Sunkara MK, Sharma S, Miranda R, Lian G, Dickey EC. Bulk synthesis of silicon nanowires using a low-temperature vapor–liquid–solid method. Appl Phys Lett 2001;79:1546–8.
[325] Kamins TI, Stanley Williams R, Basile DP, Hesjedal T, Harris JS. Ti-catalyzed Si nanowires by chemical vapor deposition: microscopy and growth mechanisms. J Appl Phys 2001;89:1008–16.
[326] Westwater J, Gosain DP, Tomiya S, Usui S, Ruda H. Growth of silicon nanowires via gold/silane vapor–liquid–solid reaction. J Vac Sci Technol B 1997;15:554–7.
[327] Hiruma K, Yazawa M, Katsuyama T, Ogawa K, Haraguchi K, Koguchi M, et al. Growth and optical properties of nanometer-scale GaAs and InAs whiskers. J Appl Phys 1995;77:447–62.
[328] Duan X, Lieber CM. Laser-assisted catalytic growth of single crystal GaN nanowires. J Am Chem Soc 1999;122:188–9.
[329] Ohlsson BJ, Björk MT, Magnusson MH, Deppert K, Samuelson L, Wallenberg LR. Size-, shape-, and position-controlled GaAs nano-whiskers. Appl Phys Lett 2001;79:3335–7.
[330] Gudiksen MS, Lieber CM. Diameter-selective synthesis of semiconductor nanowires. J Am Chem Soc 2000;122:8801–2.
[331] Givargizov EI. Highly anisotropic crystals. D Reidel Pub Co; 1987.
[332] Davis SH. On the principle of exchange of stabilities. Proc Roy Soc Lond A Math Phys Sci 1969;310:341–58.
[333] Galdi G, Straughan B. Exchange of stabilities, symmetry, and nonlinear stability. Arch Ration Mech An 1985;89:211–28.
[334] Feng SQ, Yu DP, Zhang HZ, Bai ZG, Ding Y. The growth mechanism of silicon nanowires and their quantum confinement effect. J Cryst Growth 2000;209:513–7.
[335] Liu ZQ, Zhou WY, Sun LF, Tang DS, Zou XP, Li YB, et al. Growth of amorphous silicon nanowires. Chem Phys Lett 2001;341:523–8.
[336] Wu Y, Cui Y, Huynh L, Barrelet CJ, Bell DC, Lieber CM. Controlled growth and structures of molecular-scale silicon nanowires. Nano Lett 2004;4:433–6.
[337] Yu H, Buhro WE. Solution–liquid–solid growth of soluble GaAs nanowires. Adv Mater 2003;15:416–9.
[338] Thürmer K, Carter CB, Bartelt NC, Hwang RQ. Self-assembly via adsorbate-driven dislocation reactions. Phys Rev Lett 2004;92:106101.
[339] Ross FM, Tersoff J, Reuter MC. Sawtooth faceting in silicon nanowires. Phys Rev Lett 2005;95:146104.
[340] Witt F, Vook RW. Thermally induced strains in cubic metal films. J Appl Phys 1968;39:2773–6.
[341] Kwon SJ, Park J-G. Theoretical analysis of growth of ZnO nanorods on the amorphous surfaces. J Chem Phys 2005;122:214714.
[342] Pelleg J, Zevin LZ, Lungo S, Croitoru N. Reactive-sputter-deposited TiN films on glass substrates. Thin Solid Films 1991;197:117–28.
[343] Kwon SJ. Theoretical analysis of non-catalytic growth of nanorods on a substrate. J Phys Chem B 2006;110:3876–82.
[344] Liang LH, Liu F, Shi DX, Liu WM, Xie XC, Gao HJ. Nucleation and reshaping thermodynamics of Ni as catalyst of carbon nanotubes. Phys Rev B 2005;72:035453.
[345] Lieber CM. The incredible shrinking circuit – researchers have built nanotransistors and nanowires. Now they just need to find a way to put them all together. Sci Am 2001;285:58–64.
[346] Wang JF, Gudiksen MS, Duan XF, Cui Y, Lieber CM. Highly polarized photoluminescence and photodetection from single indium phosphide nanowires. Science 2001;293:1455–7.
[347] Lee ML, Fitzgerald EA, Bulsara MT, Currie MT, Lochtefeld A. Strained Si, SiGe, and Ge channels for high-mobility metal-oxide-semiconductor field-effect transistors. J Appl Phys 2005;97:011101.
[348] He R, Yang P. Giant piezoresistance effect in silicon nanowires. Nat Nano 2006;1:42–6.
[349] Xiang J, Lu W, Hu YJ, Wu Y, Yan H, Lieber CM. Ge/Si nanowire heterostructures as high-performance field-effect transistors. Nature 2006;441:489–93.
[350] Tian B, Zheng X, Kempa TJ, Fang Y, Yu N, Yu G, et al. Coaxial silicon nanowires as solar cells and nanoelectronic power sources. Nature 2007;449:885–9.
[351] Pekoz R, Malcioglu OB, Raty JY. First-principles design of efficient solar cells using two-dimensional arrays of core-shell and layered SiGe nanowires. Phys Rev B 2011;83:035317.

[352] Qian F, Li Y, Gradecak S, Park H-G, Dong Y, Ding Y, et al. Multi-quantum-well nanowire heterostructures for wavelength-controlled lasers. Nat Mater 2008;7:701–6.
[353] Hu Y, Churchill HOH, Reilly DJ, Xiang J, Lieber CM, Marcus CM. A Ge/Si heterostructure nanowire-based double quantum dot with integrated charge sensor. Nat Nano 2007;2:622–5.
[354] Roddaro S, Fuhrer A, Brusheim P, Fasth C, Xu HQ, Samuelson L, et al. Spin states of holes in Ge/Si nanowire quantum dots. Phys Rev Lett 2008;101:186802.
[355] Liang G, Xiang J, Kharche N, Klimeck G, Lieber CM, Lundstrom M. Performance analysis of a Ge/Si core/shell nanowire field-effect transistor. Nano Lett 2007;7:642–6.
[356] Hao X-J, Tu T, Cao G, Zhou C, Li H-O, Guo G-C, et al. Strong and tunable spin-orbit coupling of one-dimensional holes in Ge/Si core/shell nanowires. Nano Lett 2010;10:2956–60.
[357] Pan L, Lew KK, Redwing JM, Dickey EC. Stranski–Krastanow growth of germanium on silicon nanowires. Nano Lett 2005;5:1081–5.
[358] Goldthorpe IA, Marshall AF, McIntyre PC. Synthesis and strain relaxation of Ge-core/Si-shell nanowire arrays. Nano Lett 2008;8:4081–6.
[359] Goldthorpe IA, Marshall AF, McIntyre PC. Inhibiting strain-induced surface roughening: dislocation-free Ge/Si and Ge/SiGe core-shell nanowires. Nano Lett 2009;9:3715–9.
[360] Li A, Ercolani D, Lugani L, Nasi L, Rossi F, Salviati G, et al. Synthesis of AlAs and AlAs–GaAs core-shell nanowires. Cryst Growth Des 2011;11:4053–8.
[361] Schmidt V, McIntyre PC, Goesele U. Morphological instability of misfit-strained core-shell nanowires. Phys Rev B 2008;77:235302.
[362] Wang H, Upmanyu M, Ciobanu CV. Morphology of epitaxial core-shell nanowires. Nano Lett 2008;8:4305–11.
[363] Tersoff J. Stress-induced layer-by-layer growth of Ge on Si(100). Phys Rev B 1991;43:9377–80.
[364] Ashu P, Matthai CC. A molecular dynamics study of the critical thickness of Ge layers on Si substrates. Appl Surf Sci 1991;48–49:39–43.
[365] Deelman PW, Thundat T, Schowalter LJ. AFM and RHEED study of Ge islanding on Si(111) and Si(100). Appl Surf Sci 1996;104–105:510–5.
[366] Wang X, Jiang Z-m, Zhu H-j, Lu F, Huang D, Liu X, et al. Germanium dots with highly uniform size distribution grown on Si(100) substrate by molecular beam epitaxy. Appl Phys Lett 1997;71:3543–5.
[367] Shchukin VA, Ledentsov NN, Kop'ev PS, Bimberg D. Spontaneous ordering of arrays of coherent strained islands. Phys Rev Lett 1995;75:2968–71.
[368] Bergamaschini R, Brehm M, Grydlik M, Fromherz T, Bauer G, Montalenti F. Temperature-dependent evolution of the wetting layer thickness during Ge deposition on Si(001). Nanotechnology 2011;22:285704.
[369] Cimalla V, Zekentes K. Temperature dependence of the transition from two-dimensional to three-dimensional growth of Ge on (001)Si studied by reflection high-energy electron diffraction. Appl Phys Lett 2000;77:1452–4.
[370] Asai M, Ueba H, Tatsuyama C. Heteroepitaxial growth of Ge films on the Si(100)-2×1 surface. J Appl Phys 1985;58:2577–83.
[371] Gu M, Zhou Y, Pan L, Sun Z, Wang S, Sun CQ. Temperature dependence of the elastic and vibronic behavior of Si, Ge, and diamond crystals. J Appl Phys 2007;102:083524.
[372] Huang Z-F, Desai RC. Instability and decomposition on the surface of strained alloy films. Phys Rev B 2002;65:195421.
[373] Fermi E, Schluter RA. Notes on quantum mechanics. University of Chicago Press; 1995.
[374] Schöllhorn C, Oehme M, Bauer M, Kasper E. Coalescence of germanium islands on silicon. Thin Solid Films 1998;336:109–11.
[375] Pachinger D, Lichtenberger H, Chen G, Stangl J, Hesser G, Schäffler F. MBE growth conditions for Si island formation on Ge(001) substrates. Thin Solid Films 2008;517:62–4.
[376] Leung YP, Liu Z, Hark SK. Changes in morphology and growth rate of quasi-one-dimensional ZnSe nanowires on GaAs(100) substrates by metalorganic chemical vapor deposition. J Cryst Growth 2005;279:248–57.
[377] Sundaresan SG, Davydov AV, Vaudin MD, Levin I, Maslar JE, Tian Y-L, et al. Growth of silicon carbide nanowires by a microwave heating-assisted physical vapor transport process using group VIII Metal catalysts. Chem Mater 2007;19:5531–7.
[378] Kikkawa J, Ohno Y, Takeda S. Growth rate of silicon nanowires. Appl Phys Lett 2005;86:123109.
[379] Mohammad SN. General hypothesis governing the growth of single-crystal nanowires. J Appl Phys 2010;107:114304.
[380] Fan HJ, Werner P, Zacharias M. Semiconductor nanowires: from self-organization to patterned growth. Small 2006;2:700–17.
[381] Fortuna SA, Wen J, Chun IS, Li X. Planar GaAs nanowires on GaAs (100) substrates: self-aligned, nearly twin-defect free, and transfer-printable. Nano Lett 2008;8:4421–7.
[382] Schmidt V, Senz S, Gösele U. Diameter-dependent growth direction of epitaxial silicon nanowires. Nano Lett 2005;5:931–5.
[383] Wang CX, Hirano M, Hosono H. Origin of diameter-dependent growth direction of silicon nanowires. Nano Lett 2006;6:1552–5.
[384] Schwarz KW, Tersoff J. From droplets to nanowires: dynamics of vapor–liquid–solid growth. Phys Rev Lett 2009;102:206101.
[385] Glas F, Harmand J-C, Patriarche G. Why does wurtzite form in nanowires of III–V zinc blende semiconductors? Phys Rev Lett 2007;99:146101.
[386] Seth AF, Xiuling L. Metal-catalyzed semiconductor nanowires: a review on the control of growth directions. Semicond Sci Technol 2010;25:024005.
[387] Cai Y, Chan SK, Sou IK, Chan YF, Su DS, Wang N. Temperature-dependent growth direction of ultrathin ZnSe nanowires. Small 2007;3:111–5.
[388] Guoqiang Z, Kouta T, Hideki G, Hidetoshi N. Parallel-aligned GaAs nanowires with lang110rang orientation laterally grown on [311] B substrates via the gold-catalyzed vapor–liquid–solid mode. Nanotechnology 2010;21:095607.

[389] Ihn SG, Song JI, Kim TW, Leem DS, Lee T, Lee SG, et al. Morphology- and orientation-controlled gallium arsenide nanowires on silicon substrates. Nano Lett 2006;7:39–44.
[390] Shan CX, Liu Z, Hark SK. CdSe nanowires with controllable growth orientations. Appl Phys Lett 2007;90:193123.
[391] Schmid H, Björk MT, Knoch J, Riel H, Riess W, Rice P, et al. Patterned epitaxial vapor-liquid-solid growth of silicon nanowires on Si(1 1 1) using silane. J Appl Phys 2008;103:024304.
[392] Alerhand OL, Berker AN, Joannopoulos JD, Vanderbilt D, Hamers RJ, Demuth JE. Finite-temperature phase diagram of vicinal Si(1 0 0) surfaces. Phys Rev Lett 1990;64:2406–9.